JUN 20 1957

Journal of Research

of the

U.S. National Bureau of Standards

UNIVERSITY OF MICHIGAN
JUN 13 1957
PHYSICS LIBRARY

JUNE 1957

VOLUME 58 NUMBER 6

U. S. DEPARTMENT OF COMMERCE
Sinclair Weeks, Secretary
NATIONAL BUREAU OF STANDARDS
A. V. Astin, Director

JUNE • 1957
VOLUME • 58
NUMBER • 6

JOURNAL OF RESEARCH
of the
NATIONAL BUREAU OF STANDARDS

The National Bureau of Standards

Functions and Activities

The functions of the National Bureau of Standards are set forth in the Act of Congress, March 3, 1901, as amended by Congress in Public Law 619, 1950. These include the development and maintenance of the national standards of measurement and the provision of means and methods for making measurements consistent with these standards; the determination of physical constants and properties of materials; the development of methods and instruments for testing materials, devices, and structures; advisory services to Government Agencies on scientific and technical problems; invention and development of devices to serve special needs of the Government; and the development of standard practices, codes, and specifications. The work includes basic and applied research, development, engineering, instrumentation, testing, evaluation, calibration services, and various consultation and information services. A major portion of the Bureau's work is performed for other Government Agencies, particularly the Department of Defense and the Atomic Energy Commission. The scope of activities is suggested by the listing of divisions and sections on the inside of the back cover.

Publications

The results of the Bureau's work take the form of either actual equipment and devices or published papers. These papers appear either in the Bureau's own series of publications or in the journals of professional and scientific societies. The Bureau itself publishes three monthly periodicals, available from the Government Printing Office: The Journal of Research, which presents complete papers reporting technical investigations; the Technical News Bulletin, which presents summary and preliminary reports on work in progress; and Basic Radio Propagation Predictions, which provides data for determining the best frequencies to use for radio communications throughout the world. There are also five series of nonperiodical publications: The Applied Mathematics Series, Circulars, Handbooks, Building Materials and Structures Reports, and Miscellaneous Publications.

Information on the Bureau's publications can be found in NBS Circular 460, Publications of the National Bureau of Standards ($1.25) and its Supplement ($0.75), available from the Superintendent of Documents, Government Printing Office, Washington 25, D. C.

Journal of Research of the National Bureau of Standards Vol. 58, No. 6, June 1957 Research Paper 2762

Slotted-Cylinder Antenna With a Dielectric Coating

James R. Wait and Walter Mientka

Analysis is presented for the fields produced by an arbitrary slot on a circular cylinder which has a concentric dielectric coating. Expressions for the far-zone fields are developed by evaluating the appropriate integrals using a saddle-point method. Numerical results are presented for the case of a narrow axial slot for a range of values of cylinder diameters and electrical constants of the dielectric coating. There is some evidence that the coating provides a trap or a duct for surface waves, resulting in an increase of over-all amplitude of the field in the backward direction.

1. Introduction

Slotted-cylinder antennas are now becoming extensively utilized in microwave radiating systems. The great interest in this subject is evidenced by the great number of papers on this subject within the last decade [1 to 7].[1] In most of the previous theoretical work, the slot is assumed to be cut on a circular or elliptical cylinder of perfect conductivity and infinite length. The computation of the radiation patterns is then straightforward, although it can be very tedious even if special summation techniques are employed. Usually it is desirable to program the series formula on an electronic calculator if extensive numerical data is required [8, 9].

Several years ago one of the authors (J. R. W.) was asked to consider the effect of covering the slot with a dielectric coating such as a fabric. A solution was carried out for an infinitely long axial slot on a circular cylinder, which itself was covered by a concentric dielectric coating of constant thickness [10]. It was shown that, if the coating thickness approached zero, the pattern approached uniformly the pattern expected for the uncoated cylinder. It was then concluded that, if the slot was covered by a lossless dielectric coating of very small thickness, the pattern would not be modified to any extent. Some related experimental work corroborated this conclusion [11].

It is the purpose of the present paper to pursue this matter further. A solution is given for the fields produced by an arbitrary slot on a circular cylinder which is covered by a concentric dielectric coating. Attention is then focused on the special case of an axial slot where the rather cumbersome formulas become less foreboding in appearance. Some numerical results are presented for the far field in the equatorial plane of the slot or in the broadside direction from the cylinder. It is then possible to give a more quantitative viewpoint of the effect of the coating.

It might be mentioned in passing that the plane wave scattering by a dielectric cylinder with a metallic core has been considered recently by Adey [12]. Some of the numerical results obtained by him could have some application to the reciprocal antenna problem for the case when the slot is circumferential.

2. Formal Solution

The cylinder is taken to have a radius a, and the concentric dielectric coating has a radius b, as indicated in figure 1. Cylindrical coordinates (ρ,ϕ,z) are chosen to be coaxial with the cylinder. The electrical constants of the coating are ϵ and μ and those of the homogeneous (air) space outside are ϵ_0 and μ_0. The tangential electric fields[2] on the cylinder are specified, being finite over the area of the slot and zero elsewhere. Therefore, following the suggestion of Silver and Saunders [7], the tangential field is written as a combined azimuthal Fourier series and axial Fourier integral, such that

$$E_\phi(a,\phi,z)=\int_{-\infty}^{\infty} dh \sum_{m=-\infty}^{+\infty} P_m(h)e^{-im\phi}e^{-ihz} \qquad (1)$$

with

$$P_m(h)=\frac{1}{(2\pi)^2}\int_{z_1}^{z_2} dz' \int_{\phi_2}^{\phi_1} d\phi' E_\phi(a,\phi',z')e^{ihz'}e^{im\phi'}, \qquad (2)$$

where the slot is considered to be bounded by $\phi_1<\phi'<\phi_2$ and $z_1<z'<z_2$ in terms of the primed coordinates. A similar relation holds for the $E_z(a,\phi,z)$ component with $P_m(h)$ being replaced by $Q_m(h)$.

In the subsequent equations, the double Fourier representation is considered as an operator to simplify the notation. For example, eq (1) is rewritten, operationally

$$E_\phi(a,\phi,z)=\Gamma P_m(h), \qquad (3)$$

where the Γ signifies the multiplication of $P_m(h)$ by $\exp[-ihz-im\phi]$ and then integration with respect to h and summation with respect to m.

In region I, defined by $a\leq\rho\leq b$, the fields can be represented as a superposition of TM (transverse magnetic) and TE (transverse electric) modes [13].

[1] Figures in brackets indicate the literature references at the end of this paper.

[2] The time factor $\exp(i\omega t)$ is employed throughout.

Therefore, the electric and magnetic field components are given by

$$E_z=\Gamma[u^2a_mH_m+u^2A_mJ_m], \tag{4}$$

$$E_\phi=\Gamma\left[i\mu\omega b_m\frac{\partial H_m}{\partial\rho}-\frac{mh}{\rho}a_mH_m+i\mu\omega B_m\frac{\partial J_m}{\partial\rho}-\frac{mh}{\rho}A_mJ_m\right], \tag{5}$$

$$E_\rho=\Gamma\left[-\frac{m\omega\mu}{\rho}b_mH_m-ihA_m\frac{\partial H_m}{\partial\rho}-\frac{m\omega\mu}{\rho}B_mJ_m-ihA\frac{\partial J_m}{\partial\rho}\right], \tag{6}$$

$$H_z=\Gamma[u^2b_mH_m+u^2B_mJ_m], \tag{7}$$

$$H_\phi=\Gamma\left[-\frac{mh}{\rho}b_mH_m-\frac{ik^2}{\mu\omega}a_m\frac{\partial H_m}{\partial\rho}-\frac{mh}{\rho}B_mJ_m-\frac{ik^2}{\mu\omega}A_m\frac{\partial J_m}{\partial\rho}\right], \tag{8}$$

$$H_\rho=\Gamma\left[-ihb_m\frac{\partial H_m}{\partial\rho}+\frac{mk^2}{\mu\omega\rho}a_mH_m-ihB_m\frac{\partial J_m}{\partial\rho}+\frac{mk^2}{\mu\omega\rho}A_mJ_m\right], \tag{9}$$

where $J_m=J_m(u\rho)$, the Bessel function of the first type of order m; where $H_m=H_m^{(2)}(u\rho)$, the Hankel function of the second kind of order m; and where $u=(k^2-h^2)^{1/2}$ and $k=(\epsilon\mu)^{1/2}\omega$. The coefficients a_m, b_m, A_m, and B_m are independent of ρ, ϕ, and z, but are as yet unknown.

In region II, defined by $\rho\geq b$, the representation is also a superposition of TM and TE modes, but now only the Hankel function is needed because it has the proper asymptotic behavior for large values of ρ. Therefore,

$$E_z=\Gamma u_0^2c_mH_m \tag{10}$$

$$E_\phi=\Gamma\left[i\mu_0\omega d_m\frac{\partial H_m}{\partial\rho}-\frac{mh}{\rho}c_mH_m\right] \tag{11}$$

$$E_\rho=\Gamma\left[-\frac{m\mu_0\omega}{\rho}d_mH_m-ihc_m\frac{\partial H_m}{\partial\rho}\right] \tag{12}$$

$$H_z=\Gamma u_0^2d_mH_m \tag{13}$$

$$H_\phi=\Gamma\left[-\frac{mh}{\rho}d_mH_m-\frac{ik_0^2}{\mu_0\omega}c_m\frac{\partial H_m}{\partial\rho}\right] \tag{14}$$

$$H_\rho=\Gamma\left[-ihd_m\frac{\partial H_m}{\partial\rho}+\frac{mk_0^2}{\mu_0\omega\rho}c_mH_m\right], \tag{15}$$

where $H_m=H_m^{(2)}(u_0\rho)$, $u_0=(k_0^2-h^2)^{1/2}$, and $k_0=(\epsilon_0\mu_0)^{1/2}\omega$. The coefficients c_m and d_m are independent of ρ, ϕ, and z.

The E_ϕ and E_z components in region I must reduce to the prescribed behavior at $\rho=a$, as noted by eq (1). Furthermore, the E_ϕ, E_z, H_ϕ and H_z components are continuous at $\rho=b$. Together these conditions lead to six linear equations to determine the six unknown coefficients. Symbolically, this set is

$$a_{mp}a_m+b_{mp}b_m+A_{mp}A_m+B_{mp}B_m+c_{mp}c_m+d_{mp}d_m=x_{mp}, \tag{16}$$

where the coefficients with the double suffix are given conveniently in table 1 for p from 1 to 6. It is now a simple matter to solve for the coefficients in determinant form. For example:

$$d_m=\frac{\begin{vmatrix} \cdot & \cdot & \cdot & \cdot & 0 & P_m \\ \cdot & 0 & \cdot & 0 & 0 & Q_m \\ \cdot & \cdot & \cdot & \cdot & \cdot & 0 \\ \cdot & 0 & \cdot & 0 & \cdot & 0 \\ \cdot & \cdot & \cdot & \cdot & \cdot & 0 \\ 0 & \cdot & 0 & \cdot & 0 & 0 \end{vmatrix}}{D}$$

and

$$c_m=\frac{\begin{vmatrix} \cdot & \cdot & \cdot & \cdot & P_m & 0 \\ \cdot & 0 & \cdot & 0 & Q_m & 0 \\ \cdot & \cdot & \cdot & \cdot & 0 & \cdot \\ \cdot & 0 & \cdot & 0 & 0 & 0 \\ \cdot & \cdot & \cdot & \cdot & 0 & \cdot \\ 0 & \cdot & 0 & \cdot & 0 & \cdot \end{vmatrix}}{D} \tag{17}$$

where the dots indicate generally finite factors obtained from the table. D is the six by six determinant of the first six columns in table 1. Expanding these determinants leads to explicit, although lengthy, expressions for the fields.

3. Far-Zone Fields

The resulting integrals in region II are of the form

$$I=-\frac{i}{2}\int_{-\infty}^{+\infty}F_m(h)H_m^{(2)}(u_0\rho)e^{-ihz}dh, \tag{18}$$

where the dependence of the geometrical factors of the coated cylinder and the excitation parameters are lumped into $F_m(h)$. For large distances from the cylinder such that $k\rho\gg1$, the Hankel and

exponential functions are rapidly varying so the integral can be evaluated by the method of steepest descents. The procedure is straightforward [6] if it is remembered that the original contour in the h plane must be indented above the branch point at $h=k$ and below the branch point at $h=-k$. The result is

$$I \cong e^{im\pi/2} \frac{e^{-ikR}}{R} F_m(k_0 \sin\theta), \tag{19}$$

where $R=(\rho^2+z^2)^{1/2}$ and $\theta=\tan^{-1}(\rho/z)$.

The far-zone form of the fields in region II are then simply obtained by replacing the Fourier operator Γ by its steepest descent form, such that

$$\Gamma F_m(h) \cong 2i \frac{e^{-ikR}}{R} \sum_{m=0}^{\infty} F_m(k_0 \sin\theta) e^{im\pi/2} e^{-im\phi}, \tag{20}$$

where terms which vary as $1/R^2$, $1/R^3$, etc., are neglected.

4. Equatorial-Plane Fields

Even after making the far-zone approximation, the expressions for the fields are very cumbersome. The situation is simplified somewhat, however, if the observer is in the equatorial plane ($z=0$ or $\theta=\pi/2$). This case is considered here and, furthermore, the slot is considered to be in the form of a narrow rectangle with its long side parallel to the cylinder axis. The integration, over the slot coordinates, indicated by eq (2) then simplifies to

$$P_m(h) \cong P_m(0) \cong \frac{1}{4\pi^2 a} \int_{z_1}^{z_2} V(z')dz', \tag{21}$$

where the center line of the slot is at $\phi=0$ and $V(z')$ is the transverse voltage along the slot.

The far-field in the equatorial plane is then conveniently written

$$E_\phi = \left[\frac{k_0}{2\pi^2} \int_{z_1}^{z_2} V(z')dz'\right] \frac{e^{-ik_0\rho}}{\rho} P(\phi), \tag{22}$$

where the pattern factor is given by

$$P(\phi) = \frac{2i}{\pi(kb)(k_0 a)} \sum_{m=0}^{\infty} \frac{\epsilon_m \cos m\phi e^{im\pi/2}}{\left(\frac{k_0\mu}{k\mu_0}\right) H_m^{(2)}(k_0 b) T_m - H_m^{(2)\prime}(k_0 b) L_m} \tag{23}$$

with $\epsilon_0=1$, $\epsilon_m=2 (m\neq 0)$ and

$$T_m = J_m'(kb) H_m^{(2)\prime}(ka) - J_m'(ka) H_m^{(2)\prime}(kb), \tag{24}$$

$$L_m = J_m(kb) H_m^{(2)\prime}(ka) - J_m'(ka) H_m^{(2)}(kb). \tag{25}$$

The prime over Bessel or Hankel function indicates a derivative with respect to its argument. As a partial check on this result it can be seen, if $b=a$ or if $\epsilon=\epsilon_0$ and $k=k_0$, that

$$P(\phi) = \frac{1}{k_0 a} \sum_{m=0}^{\infty} \frac{\epsilon_m \cos m\phi e^{im\pi/2}}{H_m^{(2)\prime}(k_0 a)}, \tag{26}$$

which is quite well known [1].

The equatorial-plane field is thus proportional to the integrated voltage moment along the slot, a simple radial factor that represents an outgoing spherical wave and a rather complicated azimuth factor. The structure of the solution is closely related to a two-dimensional (scalar) problem carried out previously [10] for an infinite axial slot with a uniform transverse voltage, V, throughout its length. The radiation field for this problem can be written

$$E_\phi = -i60\epsilon_0 \omega V \left(\frac{2}{\pi k_0 \rho}\right)^{\frac{1}{2}} e^{-i(k_0\rho - \pi/4)} P(\phi), \tag{27}$$

which has the form of an outgoing cylindrical wave with the same azimuthal dependence, $P(\phi)$, as for the finite slot. This two-dimensional counterpart is of further interest because it has a well defined acoustic analogy. In this instance, E_ϕ is proportional to the pressure field, in a medium whose wave number is k_0, emanating from a cylindrical radiator. The source is a rigid cylinder except for the narrow axial slot where the normal velocity is specified. Surrounding this cylinder is a film whose acoustic wave number is k and a density, relative to the outer medium, equal to ϵ/ϵ_0.

Although the prime purpose, stated in the introduction, is to evaluate the effect of the dielectric coating, it does seem worthwhile for the sake of completeness to consider the effect when μ/μ_0 is different from unity. Composite materials can be produced whose macroscopic permeability differs from unity so the results may be quite significant in their own right.

Keeping in mind the above points, numerical computations of $P(\phi)$ were carried for two sizes of cylinders ($k_0 a=2$ and 3) and for a range of values of $k_0 b$, ϵ/ϵ_0, and μ/μ_0. Of course, a detailed study of the interrelation between these parameters would entail a great deal of numerical work. As a compromise, only a limited number of sets of calculations were carried out for the amplitude and phase of $P(\phi)$ for intervals of ϕ of 10 degrees, using available tables of Bessel functions [14]. Case I refers to the set of calculations where $\mu/\mu_0=1$, $(\epsilon/\epsilon_0)^{\frac{1}{2}}=N$ and case II to the set where $\epsilon/\epsilon_0=1$, $(\mu/\mu_0)^{\frac{1}{2}}=M$. Setting $A=k_0 a$ and $B=k_0 b$, results were obtained for case I, taking

$A=2.0$, $N=2.0$, with $B=2.1$, 2.2, 2.3;
$A=2.0$, $N=1.5$, with $B=2.2$; and
$A=3.0$, $N=2.0$, with $B=3.2$.

Corresponding values were obtained for case II with M replacing N. For sake of comparison, the two relatively trivial situations, $A=B=2.0$ and $A=B=3.0$, were also considered.

The numerical results are summarized in tables 1, 2, and 3 with the appropriate values of A, B, and N or M at the head of each column of entries. If

further values of $P(\phi)$ are required at smaller intervals of ϕ, they can be computed directly from the following formula

$$P(\phi)=\frac{2}{\pi(k_0a)(kb)}\sum_{m=0}^{\infty}D_m\cos m\phi, \tag{28}$$

where D_m is a Fourier coefficient listed in tables 4 and 6 for values of m up to 10. For the uncoated cylinder, where $A=B$, it is convenient to redefine the Fourier representation of $P(\phi)$ by

$$P(\phi)=\frac{1}{(k_0a)}\sum_{m=0}^{\infty}d_m\cos m\phi, \tag{29}$$

where d_m is tabulated in table 7.

The amplitude and phase [3] of $P(\phi)$ are shown plotted in figures 2 to 7. The set in figures 2, a, and 2, b, indicate, in a graphic way, the effect of varying the thickness of the dielectric coating for a fixed value of a. Figures 3, a, and 3, b, show the influence of the dielectric constant of the coating material and figures 4, a, and 4, b, pertain to a larger cylinder. It appears from these curves that the only significant change in the pattern, resulting from the addition of a dielectric coating, is to enhance the ripples in the curves. Physically, it may be supposed that the radiation from the slot travels around the periphery of the cylinder in both directions. The coating apparently "traps" these peripheral surface waves to some extent and consequently enhances the standing wave pattern. The fact that the period of this standing wave pattern does not depend essentially on the dielectric constant would indicate that surface wave is guided, with considerable leakage, along or just above the dielectric-air interface. The only essential effect of increasing the size of the cylinder is to increase the number of ripples and reduce their magnitude somewhat.

The set of curves in figures 5 to 7 correspond to a coating whose permeability relative to free space is M^2. The pronounced effect of wave trapping by a permeable layer is striking. The ripples in the pattern are much larger than the corresponding ones for the purely dielectric coating. Furthermore, it is apparent that the period of the ripples is modified by the permeability ratio M^2, indicating that the trapped peripheral surface waves are largely confined to within the film. Therefore, their phase velocity is mainly determined by the wave number k rather than k_0.

5. Concluding Remarks

The analytical expressions developed herein are available for any future calculations of patterns of slotted cylinder antennas with dielectric coverings. The formulas could probably be programed for machine calculators if further numerical data are required. The complexity of the numerical procedures becomes excessive when the directions are not in the equatorial plane. It would seem to be desirable to search for an approximation technique to supplement this work. At the moment, the outlook is optimistic, using techniques based on simplified boundary conditions. In any event the rigorous calculations presented here should provide a comparative basis for checking any new approximate formulations.

On the basis of the limited calculations presented here it can be concluded that a thin dielectric film would have only a small effect on the radiation pattern for an axially slotted cylinder. On the other hand, a thin permeable film encasing the cylinder would substantially modify the pattern, indicating the presence of trapped peripheral surface waves.

We thank R. A. Hurd of the National Research Council of Canada for his comments and the verification of the final formulas in reference 10.

6. References

[1] J. R. Wait, Radiation characteristics of axial slots on a conducting cylinder, Wireless Engr. **32,** 316 (Dec. 1955).

[2] A. A. Pistolkors, Radiation from a transverse slit on the surface of a circular cylinder, J. Tech. Phys., U. S. S. R., **17,** 377 (1947) (in Russian).

[3] George Sinclair, The pattern of slotted-cylinder antennas, Proc. Inst. Radio Engrs. **36,** 1487 (1948).

[4] C. H. Papas and Ronold King, Currents on the surface of an infinite cylinder excited by an axial slot, Quart. Appl. Math. **16,** 175 (1949).

[5] C. H. Papas, Radiation from a transverse slot on an infinite cylinder, J. Math. Phys. **28,** 227 (1950).

[6] J. R. Wait, Radiation from a slot on a cylindrically tipped wedge, Can. J. Phys. **32,** 714 (1954).

[7] S. Silver and W. K. Saunders, Field produced by a transverse slot on a circular cylinder, J. Appl. Phys. **21,** 745 (1950).

[8] L. L. Bailin, Field produced by a slot on a large circular cylinder, Trans. Inst. Radio Engrs. (PGAP) **AP-3,** 128 (July 1955).

[9] J. R. Wait, and J. Kates, Radiation patterns of circumferential slots on moderately large conducting cylinders, Inst. Elect. Engrs. (London), Monograph No. 167R, February 1956 (to be republished in Pt. C of the Proceedings).

[10] J. R. Wait Slotted-cylinder antenna with a dielectric coating, Addendum to Radio Physics Laboratory, Project Report 19-0-13 (Ottawa, Nov. 1954).

[11] D. G. Frood and J. R. Wait, An investigation of slot radiators in metal plates, Proc. Inst. Elec. Engrs. **103,** 103 (Jan. 1956).

[12] A. W. Adey, Scattering of electromagnetic waves by co-axial cylinders, Can. J. Phys. **34,** 510 (May 1956); also A. W. Adey (Ph. D. Thesis, Imperial College, Univ. of London, 1954).

[13] J. A. Stratton, Electromagnetic theory, p. 354 (McGraw-Hill Book Co., Inc., New York, N. Y., 1941).

[14] Scattering and radiation from circular cylinders and spheres, Math. Tables Proj. and M. I. T. Underwater Sound Laboratory, A. M. P. Report, 62-1-R (1945).

[15] R. S. Elliott, Spherical surface antennas, Trans. Inst. Radio Engrs. (PGAP) **AP-4,** 422 (July 1956).

[3] Actually the quantity plotted is the phase lag, which is simply the negative of the phase.

TABLE 1. *List of coefficients*

p	a_{mp}	b_{mp}	A_{mp}	B_{mp}	c_{mp}	d_{mp}	ε_{mp}
1	$-\frac{m^2}{a}H_m(ua)$	$i\mu\omega a H_m'(ua)$	$-\frac{m^2}{a}J_m(ua)$	$i\mu\omega a J_m'(ua)$	0	0	P_m
2	$u^2H_m(ua)$	0	$u^2J_m(ua)$	0	0	0	Q_m
3	$-\frac{m^2}{b}H_m(ub)$	$i\mu\omega a H_m'(ub)$	$-\frac{m^2}{b}J_m(ub)$	$i\mu\omega a J_m'(ub)$	$\frac{m^2}{b}H_m(ua^2/b)$	$-i\mu\omega a a H_m'(ua^2/b)$	0
4	$u^2H_m(ub)$	0	$u^2J_m(ub)$	0	$-u_0^2H_m(ua^2/b)$	0	0
5	$-\frac{ik^2}{\mu\omega}aH_m(ub)$	$-\frac{m^2}{b}H_m(ub)$	$-\frac{ik^2}{\mu\omega}aJ_m'(ub)$	$-\frac{m^2}{b}J_m(ub)$	$+\frac{ik_0^2a}{\mu\omega}H_m'(ua^2/b)$	$+\frac{m^2}{b}H_m(ua^2/b)$	0
6	0	$u^2H_m(ub)$	0	$u^2J_m(ub)$	0	$-u_0^2H_m(ua^2/b)$	0

TABLE 2. *The pattern function, $P(\phi)$*

Case I

A	2.0	2.0	2.0	2.0	3.0
B	2.1	2.2	2.3	2.2	3.2
N	2.0	2.0	2.0	1.5	2.0
ϕ					
	Amplitude $\lvert P(\phi)\rvert$				
deg					
0	3.01542	3.19057	3.39700	3.03693	3.25498
10	3.01288	3.19604	3.40803	3.04000	3.26369
20	3.00124	3.20722	3.43740	3.04148	3.27721
30	2.98859	3.20737	3.46905	3.02249	3.25953
40	2.89763	3.16737	3.46672	2.96182	3.16938
50	2.77345	3.05397	3.37882	2.84294	3.00552
60	2.59731	2.85054	3.16491	2.66134	2.84440
70	2.39951	2.58432	2.83926	2.43991	2.77577
80	2.23553	2.33949	2.50987	2.24187	2.74122
90	2.14398	2.21216	2.34650	2.13614	2.55112
100	2.09373	2.19945	2.39723	2.10868	2.13839
110	1.99247	2.16949	2.47021	2.04517	1.75636
120	1.75627	1.97774	2.35044	1.83122	1.74087
130	1.36811	1.57187	1.91386	1.43816	1.82952
140	0.919801	1.04402	1.24227	0.960739	1.57059
150	.699471	0.759246	0.758170	.706317	0.918C74
160	.919829	1.05545	1.12441	.936848	.575483
170	1.21183	1.43974	1.64774	1.25289	1.13915
180	1.32861	1.59211	1.85397	1.37960	1.41882
	Phase of $P(\phi)$				
deg	*deg*	*deg*	*deg*	*deg*	*deg*
0	213.533	213.044	211.124	212.873	268.001
10	211.872	211.274	209.172	211.238	265.428
20	206.967	206.111	203.543	206.379	257.900
30	199.001	197.917	194.805	198.410	245.748
40	188.139	187.046	183.566	187.474	228.942
50	174.373	173.583	170.085	173.662	206.883
60	157.447	157.142	153.956	156.842	179.269
70	137.032	136.872	133.942	136.562	148.124
80	113.415	112.152	108.449	112.588	117.146
90	88.386	84.477	78.257	86.450	87.094
100	64.621	57.919	49.050	61.575	53.961
110	43.553	35.268	25.421	40.094	11.569
120	24.517	15.904	6.644	21.221	−33.607
130	4.689	−3.355	−10.083	1.840	−66.340
140	−23.597	−30.693	−34.167	−25.805	−89.882
150	−73.823	−83.857	−89.225	−76.936	−118.365
160	−116.591	−129.818	−145.407	−122.107	−201.661
170	−133.636	−146.697	−162.914	−139.824	−246.587
180	−138.047	−150.933	−166.999	−144.379	−253.828

TABLE 3. *The pattern function, $P(\phi)$*

Case II

A	2.0	2.0	2.0	2.0	3.0
B	2.1	2.2	2.3	2.2	3.2
M	2.0	2.0	2.0	1.5	2.0
ϕ					
	Amplitude $\lvert P(\phi)\rvert$				
deg					
0	3.24416	2.31378	2.03562	2.95396	2.21707
10	3.22684	2.39152	1.98875	2.96226	2.33487
20	3.17033	2.60844	2.01230	2.97840	2.68975
30	3.06456	2.90218	2.38631	2.97777	3.14516
40	2.90306	3.15747	3.03508	2.92675	3.38660
50	2.69616	3.23706	3.60060	2.79816	3.15344
60	2.48507	3.04068	3.75866	2.59546	2.55238
70	2.33989	2.58334	3.33416	2.37581	2.34847
80	2.31662	2.10452	2.39243	2.24065	2.93850
90	2.38889	2.07404	1.53994	2.24916	3.32516
100	2.44442	2.54071	2.05310	2.32363	2.81914
110	2.35724	2.97488	3.09308	2.30334	1.75203
120	2.07477	2.98713	3.59479	2.06652	1.93906
130	1.54389	2.41705	3.22720	1.59490	2.90073
140	0.984364	1.41820	2.03580	1.01666	2.90070
150	.838475	0.753540	0.563512	0.836482	1.67907
160	1.25306	1.63859	1.66202	1.16270	0.682360
170	1.66607	2.51597	2.96109	1.58455	2.24128
180	1.82366	2.84481	3.44712	1.74717	2.92864
	Phase $P(\phi)$				
deg	*deg*	*deg*	*deg*	*deg*	*deg*
0	195.746	181.927	203.376	198.928	244.215
10	194.478	179.637	196.348	197.452	238.733
20	190.593	173.720	176.260	193.110	226.331
30	183.829	165.967	152.122	186.060	213.095
40	173.816	157.381	134.364	176.340	200.028
50	159.886	147.730	122.656	163.649	183.651
60	141.448	135.613	113.362	147.238	155.984
70	118.679	117.878	102.969	126.198	110.576
80	93.6919	88.8039	85.1765	100.893	71.5498
90	69.8430	49.4196	40.0331	74.6644	47.2343
100	49.0554	18.1857	−17.5717	51.5239	24.8248
110	31.0754	−0.997004	−40.9840	32.4240	−16.9857
120	14.1408	−14.2664	−52.0521	15.7465	−88.3266
130	−4.71149	−26.4508	−59.9543	−1.96822	−119.898
140	−36.3708	−46.0996	−69.9043	−30.1175	−134.839
150	−94.4545	−120.536	−125.229	−68.1046	−150.876
160	−132.229	−174.999	−221.830	−130.191	−262.113
170	−145.796	−186.333	−231.038	−144.773	−304.272
180	−149.319	−188.884	−232.834	−148.435	−308.423

TABLE 4. *The pattern function, $P(\phi)$*

A	2.0	3.0	A	2.0	3.0
B	2.0	3.0	B	2.0	3.0
ϕ			ϕ		
	Amplitude $\lvert P(\phi) \rvert$			Phase of $P(\phi)$	
deg			*deg*	*deg*	*deg*
0	2.91946	3.01228	0	213.310	268.778
10	2.91276	3.00388	10	211.744	266.384
20	2.88927	2.97364	20	207.088	259.219
30	2.83980	2.91104	30	199.443	247.294
40	2.75287	2.81299	40	188.880	230.567
50	2.62188	2.69702	50	175.358	209.146
60	2.45475	2.59185	60	158.719	183.822
70	2.27965	2.49434	70	138.910	156.249
80	2.13482	2.34577	80	116.525	127.691
90	2.03659	2.08708	90	93.2106	97.6070
100	1.95124	1.76251	100	70.9499	63.3880
110	1.81096	1.53456	110	50.6797	23.9124
120	1.56192	1.47497	120	31.6970	−14.0465
130	1.20474	1.39522	130	11.2645	−43.9331
140	0.827194	1.10650	140	−17.8471	−68.8592
150	.659809	0.648455	150	−65.1264	−102.208
160	.830784	.488877	160	−104.451	−176.508
170	1.05811	.815190	170	−121.274	−216.288
180	1.14974	.978586	180	−125.766	−224.045

TABLE 5. *Real and imaginary parts of D_m*

Case I

A	2.0		2.0		2.0		2.0		3.0	
B	2.1		2.2		2.3		2.2		3.2	
N	2.0		2.0		2.0		1.5		2.0	
m	Real	Imaginary	Real	Imaginary	Real	Imaginary	Real	Imaginary	Real	Imaginary
0	−11.2226	+2.09515	−12.7066	+1.96495	−13.8062	+2.95754	−8.90168	+1.68116	−16.5595	−15.6040
1	−23.5768	−2.24456	−25.8912	−1.84874	−29.1592	−1.06811	−18.7073	−1.59443	−28.0280	−37.0156
2	−11.9489	−22.4385	−15.5227	−23.7477	−20.4830	−24.2632	−10.2028	−17.3962	−5.77076	−49.4498
3	+ 4.2228	−2.88595	+7.9116	−4.83094	+22.2909	−8.60814	+11.8857	−2.78592	+44.6068	−33.2523
4	+0.069988	+3.61684	+0.126520	+4.56540	+0.224247	+5.78874	+0.069761	+3.01377	+14.6735	+39.6346
5	−.728316	+0.000862	−.909943	+0.001481	−1.11811	+0.002667	−.601487	+0.000810	−13.0184	+0.665336
6	$+2.11\times10^{-5}$	−.125133	-9.3×10^{-7}	−.155779	-5.06×10^{-5}	−.187316	-2.2×10^{-6}	−.010257	−0.014469	−3.21999
7	+0.018472	-6.57×10^{-7}	+0.022940	-2.48×10^{-7}	+0.027259	-7.99×10^{-7}	+0.015030	-6.4×10^{-7}	+.708769	−0.000213
8	-4.38×10^{-5}	+0.002381	-2.49×10^{-5}	+0.002948	-5.02×10^{-5}	+0.003456	0	+0.001922	$+8.4\times10^{-5}$	+.137679
9	−0.000272	0	−0.000335	-1.15×10^{-5}	−0.000388	-7.4×10^{-9}	−0.000217	0	−0.0222783	-4.09×10^{-4}
10	0	-2.79×10^{-5}	0	-3.42×10^{-5}	0	-4.15×10^{-5}	0	-2.2×10^{-5}	$+2.7\times10^{-7}$	−0.003674

TABLE 6. *Real and imaginary parts of D_m*

Case II

m	Real	Imaginary	Real	Imaginary	Real	Imaginary	Real	Imaginary	Real	Imaginary
0	−10.1144	+5.17046	−8.52101	+7.38167	−6.04711	+7.78317	−8.06944	+3.64159	−18.5527	−4.24158
1	−23.4645	+4.80230	−20.2125	+10.7968	−15.8423	+13.1521	−18.4190	+2.76455	−36.1706	−14.4406
2	−20.9042	−20.6570	−27.0293	−9.50969	−22.7941	−0.004936	−14.1839	−16.0117	−27.5801	−31.2589
3	+13.8792	−4.47222	+24.4545	−14.3722	+18.3439	−38.8382	+12.1601	−2.99106	+10.0303	−51.4962
4	+0.071869	+3.64883	+0.141618	+4.75266	+0.292332	+6.37791	+0.52345	+2.74666	+39.0508	+43.1818
5	−.682888	+0.000684	−.816135	+0.001061	−.975191	+0.001744	−.520680	+0.000487	−16.4855	+1.23400
6	+.00000177	−.111720	−.0000011	−.128662	−.000065	−.146022	−.0000015	−.085703	−0.015533	−3.30210
7	+.015869	−.00000034	+.017896	-3.12×10^{-7}	+.020054	−.00000064	+.012221	−.00000048	+.655067	−0.000158
8	−.0000000344	+.001981	-3.51×10^{-5}	+0.002263	−.000000037	+.002436	0	+.001530	+.0000096	+.119019
9	−.0002201	0	−0.000242	-9.3×10^{-9}	−.000266	−.00000000053	−0.000170	0	−.019108	−.000045
10	0	−.000022	0	−0.0000241	0	−.000027	0	−0.000017	+.00000026	−.002903

TABLE 7. *Real and imaginary parts of* d_m

m	$A=2.0$ $B=2.0$		$A=3.0$ $B=3.0$	
	Real	Imaginary	Real	Imaginary
0	−1.67622	+0.310971	−1.53852	−1.47332
1	−3.50102	−.400130	−2.54238	−3.53029
2	−1.44185	−3.28618	−0.160813	−4.62823
3	+1.82162	−0.270294	+4.33813	−2.03120
4	+0.006261	+.454036	+0.548382	+2.81856
5	−.090604	+.000063	−.884368	+0.023621
6	0	−.015290	−.000506	−.223038
7	+0.002214	0	+.048952	−.000008
8	0	+0.000280	0	+.009409
9	−0.000031	0	−0.001603	0
10	0	−0.000003	0	−0.000245

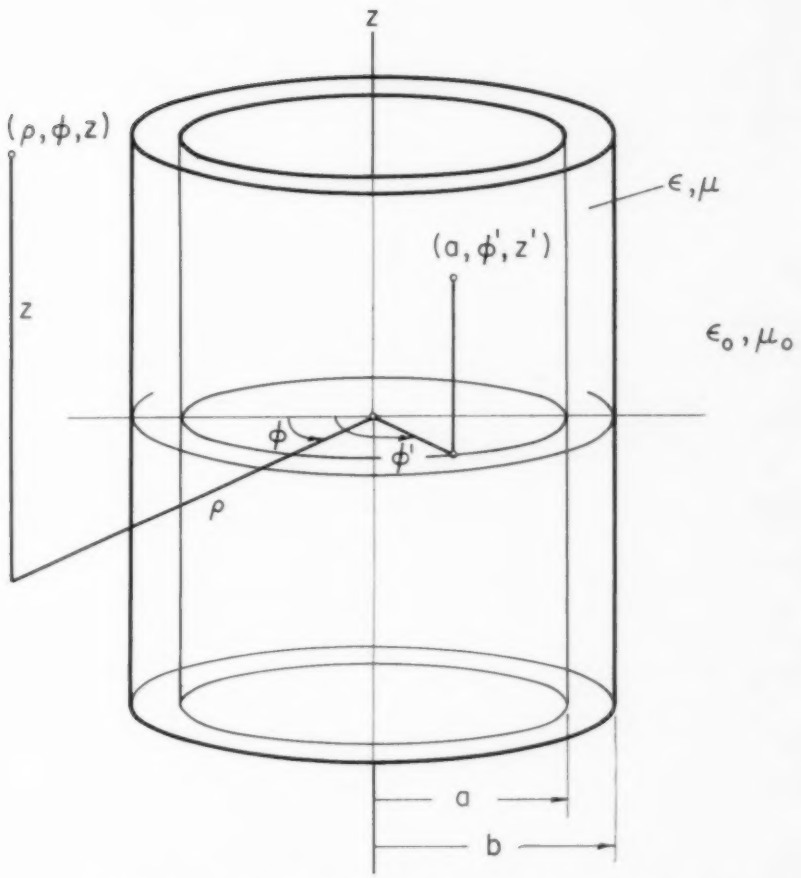

FIGURE 1. *Coordinate systems for the dielectric-coated cylinder of infinite length.*

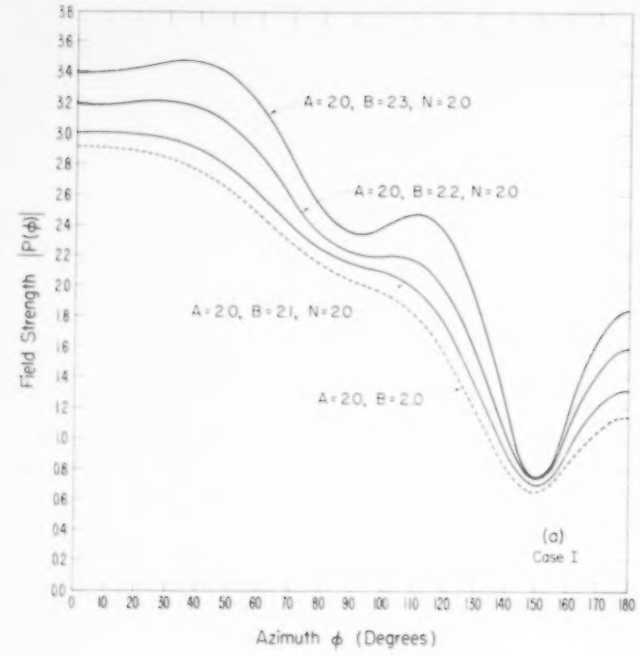

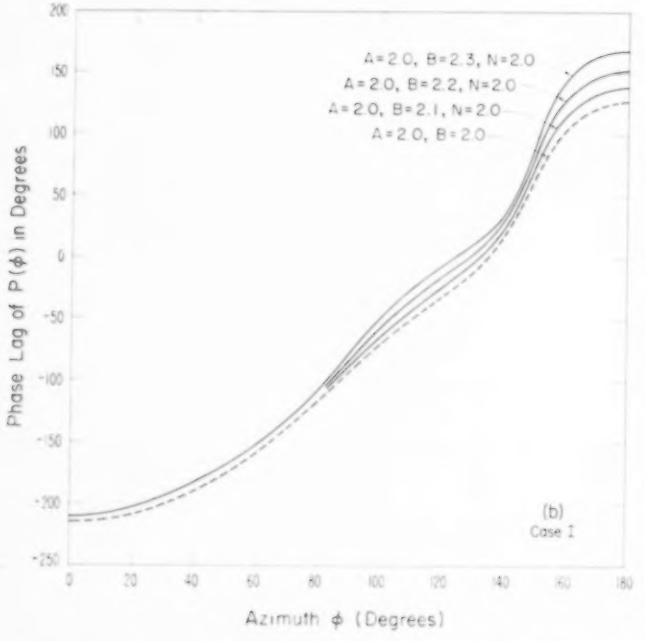

FIGURE 2. *Pattern of slotted-cylinder antenna with a dielectric coating showing effect of thickness.*

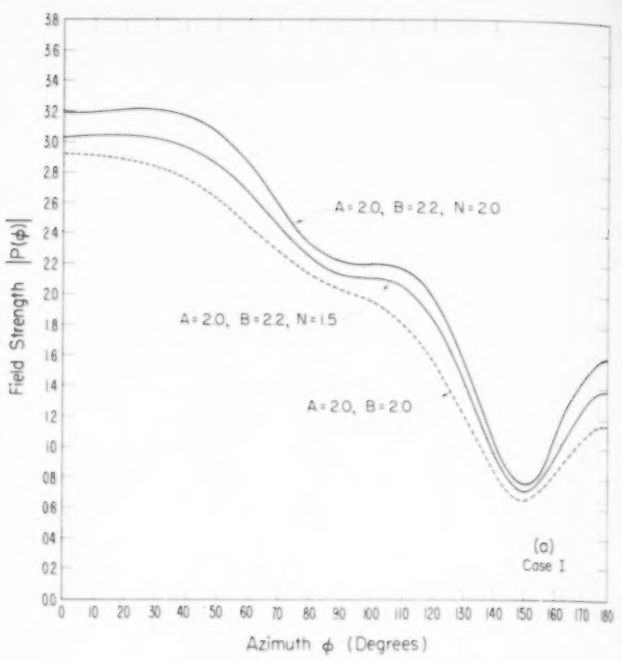

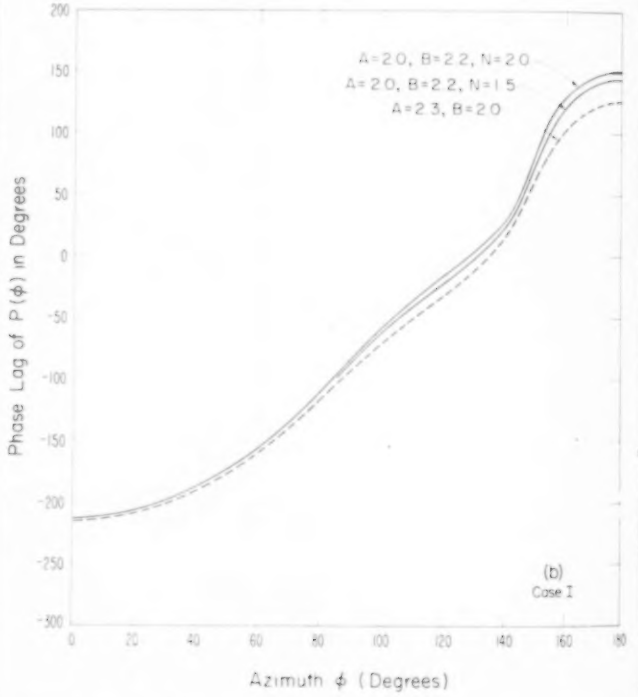

FIGURE 3. *Pattern of slotted-cylinder antenna with a dielectric coating showing effect of refractive index.*

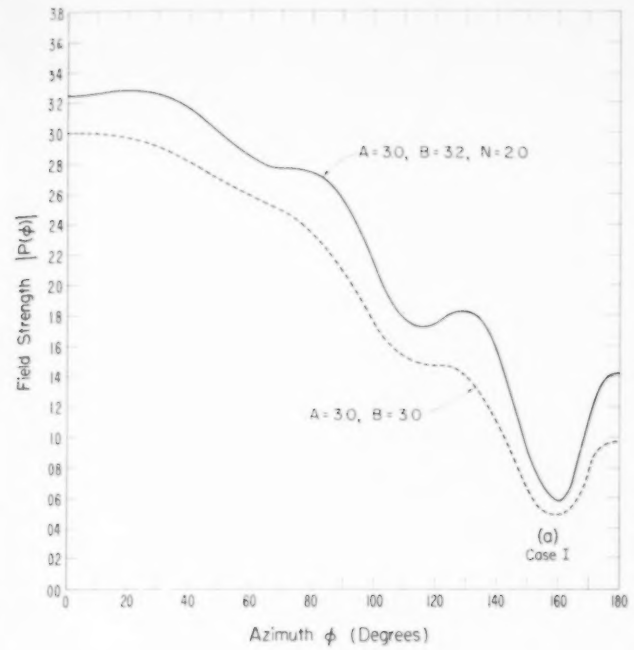

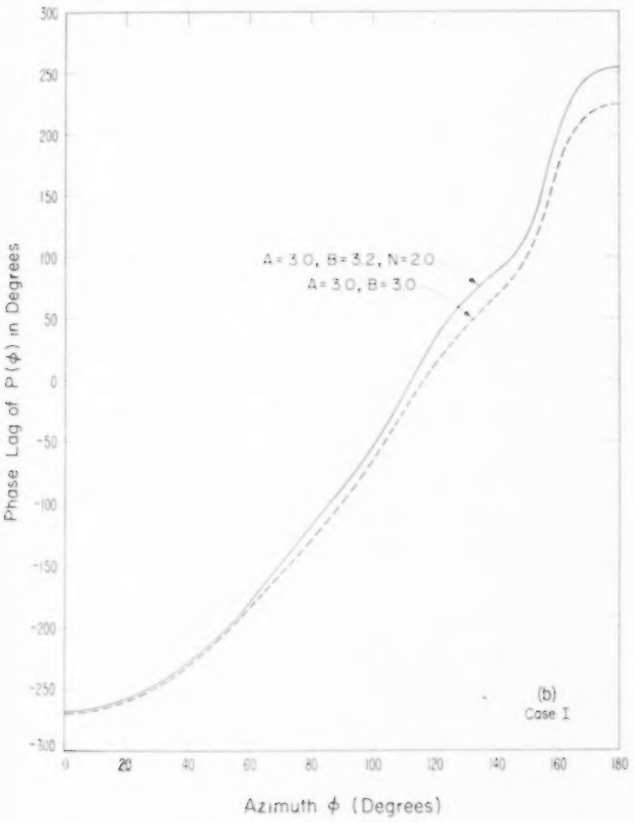

FIGURE 4. *Pattern of slotted-cylinder antenna with a dielectric coating for a larger cylinder.*

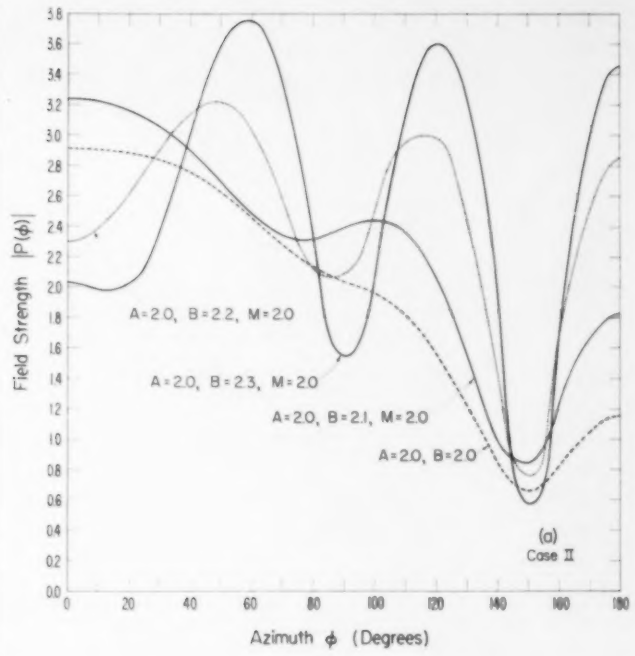

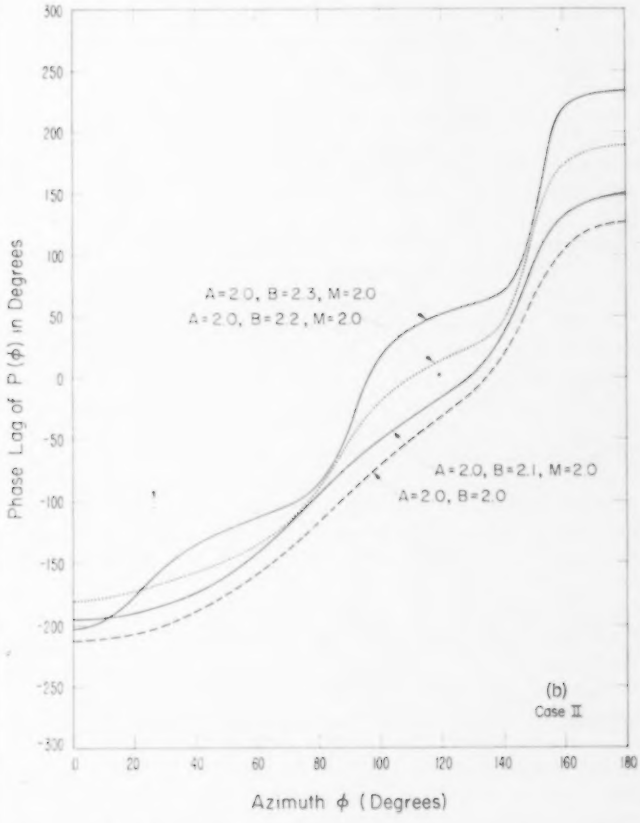

FIGURE 5. *Pattern of slotted-cylinder antenna with a permeable coating showing effect of coating thickness.*

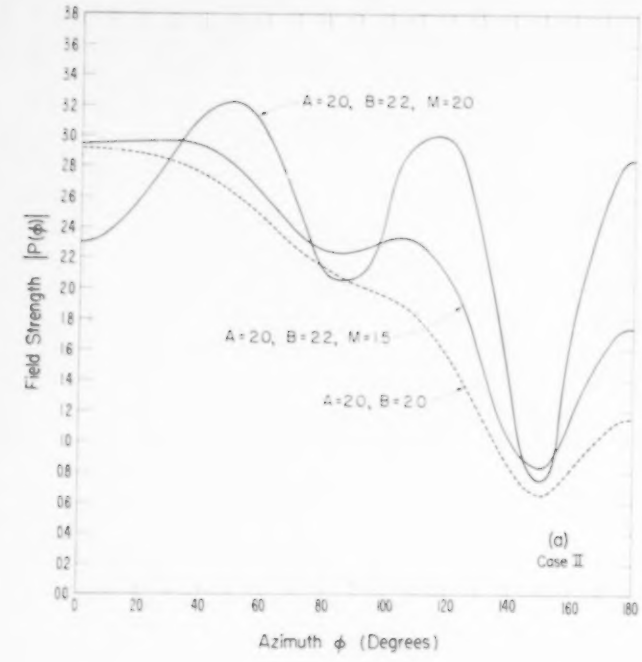

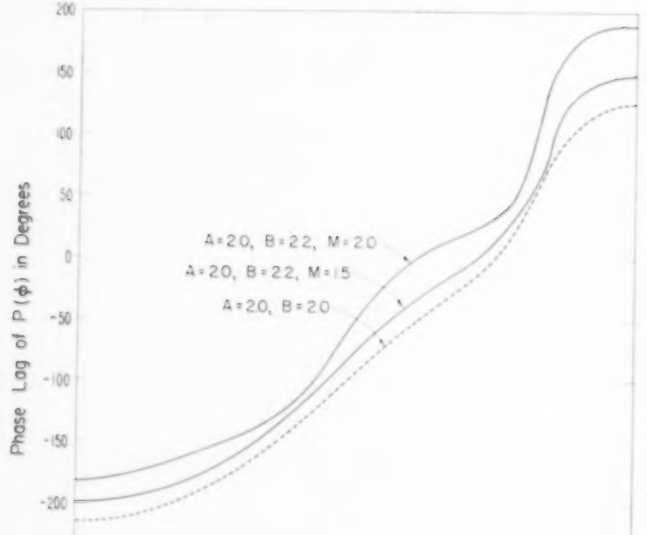

FIGURE 6. *Pattern of slotted-cylinder antenna with a permeable coating showing effect of refractive index.*

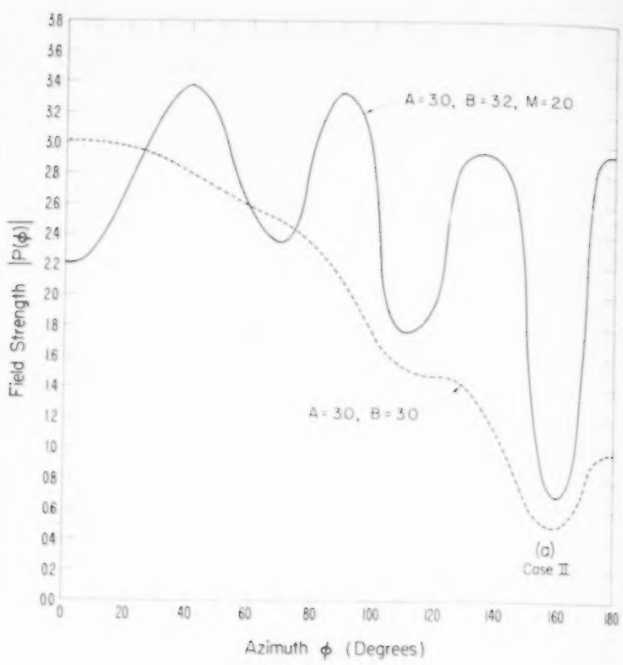

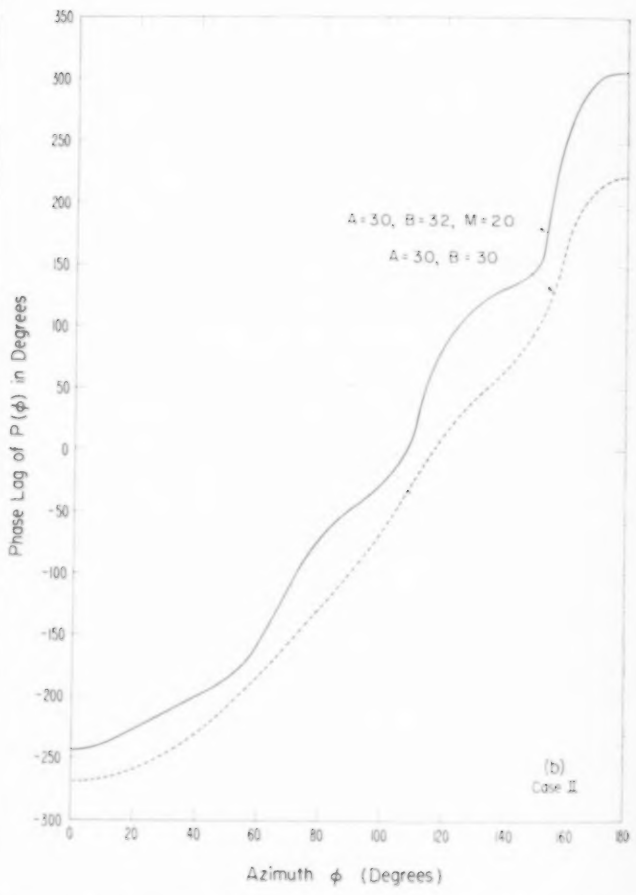

FIGURE 7. *Pattern of slotted-cylinder antenna with a permeable coating for a larger cylinder.*

BOULDER, COLO., October 25, 1956.

Journal of Research of the National Bureau of Standards Vol. 58, No. 6, June 1957 Research Paper 2763

Emission Spectra of Actinium

William F. Meggers, Mark Fred,[1] and Frank S. Tomkins [1]

Small samples of actinium, produced by transmuting radium, have been investigated spectroscopically by photographing the spectra of light emitted by the samples when excited in a hollow cathode or in arcs and sparks between copper or silver electrodes. The wavelengths were measured, and intensities estimated, for some 500 lines characteristic of actinium in the spectral range 2062.00 to 7886.82 A. A comparison of line characteristics in different sources permitted sorting into five categories; about 140 lines belong to Ac I, more than 300 were ascribed to Ac II, 8 were definitely assigned to Ac III, 5 may belong to Ac IV, and about 80 represent band heads characteristic of AcO, the actinium-monoxide molecule.

Analyses of the first three spectra of actinium have revealed their most important features, including atomic-energy levels, spectral terms, and electron configurations. The ground state of Ac III is found to be $(7s)^2S_{0\frac{1}{2}}$, that of Ac II is $(7s^2)^1S_0$, and that of Ac I is $(6d7s^2)^2D_{1\frac{1}{2}}$. Comparisons of the analogous spectra of the chemical homologs (scandium, yttrium, lanthanum, and actinium) show that actinium closely resembles yttrium, except that additional terms of odd parity, first found in lanthanum spectra and attributed to the $4f$ electron, are also found in actinium spectra, where they provide evidence of the presence of the $5f$ electron. The binding force on the $4f$ electron in La II is much stronger than on $5f$ in Ac II. The principal ionization potential of Ac^+ ions is about 12.0 electron volts.

1. Introduction

In 1899 Andre Debierne [1] [2] discovered a new chemical element in pitchblende. After chemically removing uranium, polonium, and radium he found a residue 100,000 times more radioactive than uranium in ionizing gases, affecting photographic emulsions, and producing fluorescence in barium platino-cyanide; he called the new element actinium [2].

After many years of research in radioactivity it has been established that actinium occurs in nature only as the daughter of protactinium, which in turn results from the spontaneous decay (emission of alpha and beta particles) of the relatively rare isotope of uranium, with atomic number 92 and mass 235. The atomic number of actinium is 89, and its mass is 227. The half life of actinium is only 22 years. Through a series of alpha and beta emissions, actinium forms a succession of highly unstable atoms of diminishing mass until it decays to a stable end-product, actinium-lead, with mass 207 and atomic number 82.

Because of its low abundance, high radioactivity, and lack of commercial uses, actinium has never been concentrated in pure form, and consequently relatively little was known about its physical properties. In particular, nothing was known about its optical spectra until 1937, when W. A. Lub [3] examined the spark spectra of lanthanum solutions containing 0.05 mg of actinium and published the wavelengths of possibly 9 lines of actinium appearing among 700 (lanthanum) lines. The wavelengths in angstroms (and intensities) of actinium lines reported by Lub were as follows: 4061.58 (4), 4088.37 (5), 4168.40 (5), 4179.93 (4), 4359.09 (3), 4386.37 (5), 4413.17 (5), 4507.20 (5) and 4812.25 (4). In the light of our present knowledge these are indeed the strongest actinium lines in this range of wavelengths, but we now know that only 1 of these lines belongs to neutral actinium atoms, 7 belong to singly ionized atoms, and 1 to doubly charged ions. No further information about the spectra of actinium was available until 1948, when the first spectrograms were made at the Argonne National Laboratory (ANL) with artificial samples of actinium created by transmuting radium in a chain-reacting uranium pile.

In the periodic chart of the atoms, scandium, yttrium, lanthanum, and actinium are homologous trivalent elements occupying the third place in the fourth, fifth, sixth, and seventh periods, respectively. After the spectra of scandium [4], yttrium [5], and lanthanum [6], had been described and interpreted, it seemed desirable to investigate the spectra of the only remaining homolog, actinium. In particular, the analysis [6] of the spectrum of singly ionized lanthanum (La II) had revealed the presence of electrons of type $4f$ in advance of their firm binding in heavier elements, and it appeared important to determine whether type $5f$ electrons are present in actinium in advance of their firm binding in succeeding elements, especially as there was much interest and speculation as to the first appearance and actual presence of type $5f$ electrons in the heavy elements [7]. For this purpose it would be necessary to observe the spectra of actinium throughout a considerable range of wavelengths, say from 2000 to 9000 A, and to differentiate between the successive spectra, Ac I of neutral atoms, Ac II of singly ionized atoms, and Ac III of doubly ionized atoms. Despite a limited range of observation and experimental difficulties on account of small samples and many impurities, adequate data have been obtained for the derivation of atomic-energy levels from the analyses of the first three spectra of actinium. The purpose of this paper is to report the experimental results and the analytical interpretations of actinium spectra, and to compare them with the facts concerning the spectra of homologous elements.

[1] Argonne National Laboratory, Lemont, Ill.
Figures in brackets indicate the literature references at the end of this paper.

2. Experimental Procedure

Because the artificial samples of actinium were made at ANL and because facilities for safe handling of "hot" materials were there available, all work with highly radioactive actinium was confined to that laboratory. The separation of actinium from radium, purification of the former, and loading of light sources were expertly performed by French Hagemann, whereas the excitation and photography of actinium spectra were carried out by Mark Fred and Frank Tomkins. The spectrograms were sent to the National Bureau of Standards, where wavelengths, relative intensities, spectral stages, and classifications of spectral lines were derived from them by W. F. Meggers.

The first milligrams of actinium were made at ANL in 1948 for chemical researches, and the first spectrogram was obtained in January 1948 by the copper-spark method [8], in which a few micrograms of actinium solution were evaporated on the ends of a pair of flat-topped copper electrodes and then excited in a high-voltage condensed spark. There were no standard wavelengths on this spectrogram, but the wavelengths of about 70 Ac lines were measured (3683.69 to 4337.15 A) relative to copper and impurity lines.

The next spectrograms of actinium were made in February 1951 with a Schüler-Gollnow type of hollow-cathode tube [9], modified by an additional ground joint between anode and cathode assemblies to avoid unwaxing. The cathode was aluminum, the anode nickel, the carrier gas argon, and the current was 100 ma. One milligram of actinium sample was put in the bottom of the cathode in the form of a 0.03-ml nitrate solution, the hydroxide was precipitated by blowing ammonia gas over it, and the precipitate was dried under a heat lamp. The actinium sample was separated from radium on February 24, 1951; it was only 2 days old when placed in the light source and relatively little actinon was being evolved.

The spectrograms were made with a Jarrell-Ash Wadsworth spectrograph, holding a 6-in. grating with a radius of curvature of 21 ft and 15,000 rules per inch. This grating is blazed for 6000 A and gives very weak spectra in the first-order ultraviolet. The reciprocal dispersion is about 5 A/mm in the first order, but the stronger spectral lines were also observed simultaneously in the second- or third-order spectra by illuminating separated segments of the spectrograph slit, some of which were covered by filters to aid in recognizing the different orders. Other sections of the slit were exposed to a "blank" source, a similar hollow-cathode lamp without the actinium charge; and finally, two portions of the slit were reserved for iron spectra to supply wavelength standards. The actinium spectrum lasted about 20 hr in the hollow-cathode lamp, and 7 exposures were recorded on Eastman Kokak 103–F and I–N plates, but no actinium lines appeared on the last exposure, probably because cathodic sputtering finally covered the sample. Because these grating spectrograms showed that many of the actinium lines had hyperfine structure, the same hollow-cathode lamp was recharged with 0.89 mg of Ac, and 5 spectrograms were made with a Fabry-Perot interferometer to resolve the hyperfine structures of the stronger Ac lines. Analysis of these interference spectrograms yielded the mechanical moment, or spin ($I=\frac{3}{2}\hbar$), of the 89 Ac^{227} nucleus [10], and preliminary values of the magnetic ($\mu=1.1$ nm) and electric quadrupole moments ($Q=-1.7\times10^{-24}$ cm^2) [11]. Additional grating spectrograms were then made after krypton was substituted for argon as an exciting gas, to permit discovery of actinium lines that had been masked by argon lines. Unfortunately the actinium spectra were very weak in these spectrograms, whereas the background was very strong because it contained most of the strong lines of argon and xenon, as well as krypton. In addition to the complete spectra of the exciting gases and intense spectra of aluminum, aluminum oxide, and aluminum hydride, the spectra from the hollow-cathode charged with actinium showed strong lines of impurities, such as sodium, potassium, boron, magnesium, calcium, and lead.

The above-mentioned grating spectrograms of the hollow-cathode source containing actinium were supplemented by two made on Eastman Kodak 103a–C plates exposed to copper sparks charged with 4 and 25 μg of actinium, respectively. These gave a good description of actinium spectra between 2600 and 6600 A.

Two additional copper-spark spectra with 70 μg of actinium were photographed on Eastman Kodak 103–C (UV) and I–N plates to record lines with shorter and longer wavelengths, respectively. The results were somewhat disappointing; only 2 lines shorter than 2600 A and 8 longer than 6600 A were captured. Typical portions of the spectra emitted by the hollow-cathode source and by the copper-spark source are reproduced in figure 1. When the intensities of actinium lines appearing in both sources, low-excitation hollow cathode and high-excitation copper spark, were compared it was easy to distinguish the successive spectra of neutral atoms Ac I, of singly ionized atoms Ac II, and of doubly ionized atoms Ac III. The intensities of Ac I lines were much greater in the hollow cathode than in the spark, the reverse was true of Ac II lines, and Ac III lines were tremendously enhanced in the spark. After the spectra were sorted with the aid of estimated intensities in the two sources, the mean wavelengths were converted to vacuum wave numbers, and regularities were sought among the latter. A constant difference of 2231.4 K was immediately found between pairs of Ac I lines; it was interpreted as the interval between low-energy ^{2}D levels arising from the valence electrons $6d\,7s^2$ thus identified. Likewise, regularities among the wave numbers of Ac II lines soon revealed low energy levels that could be assigned to electron configurations $6d^2$, $6d\,7s$, and $7s^2$, the last giving a ^{1}S$_0$ term that represents the ground state of Ac^{++} ions. These results for Ac I and Ac II were orally presented [12] in Chicago at the 36th annual meeting of the Optical Society of America on October 23, 1951.

FIGURE 1. *Emission spectra of actinium.*

Upper, aluminum hollow cathode containing 1 mg of Ac and argon gas; strong lines of argon, calcium, and potassium are marked, but aluminum 3944 and 3962 are not. Lower, spark spectra of copper and 25 μg Ac.

These analyses of Ac I and Ac II spectra were handicapped by weak observations in the ultraviolet below 3000 A and by the lack of strong spark spectrograms above 6600 A. Moreover, a strong background of argon and aluminum in hollow-cathode spectra suggested that some actinium lines might be masked, and in the copper-spark spectra some actinium lines might be hiding behind copper lines. In order to eliminate obscuration by this background it was suggested that arc and spark spectra of actinium be made, first by loading silver electrodes with actinium, and second by loading copper electrodes with actinium. In each case, arc and spark spectra of unloaded electrodes should be juxtaposed so that silver and copper lines could be recognized, and then actinium lines masked by silver would be revealed in the copper spectrograms, and vice versa. Such spectrograms with silver and copper electrodes were made in February 1955 after a new sample of actinium became available and a new grating was installed in a Paschen-Runge mounting at ANL. The grating has a diameter of 8 in. and a radius of curvature of 30 ft.; it is ruled with 15,000 lines/in. and is blazed to give high intensity at 4000 A. The reciprocal dispersion in spectra from this instrument is about 1.8 A/mm in the first order. Overlapping spectral orders were differentiated by supporting appropriate gelatine filters in front of the photographic plates to absorb portions of the slit images. Because this instrument is not stigmatic, slit diaphragms could not be used, but a movable mask near the photographic plates occulted the lower half for arc exposures and the upper half for spark exposures. Unfortunately, spectra of unloaded electrodes could not be juxtaposed to those with actinium-loaded electrodes; the former were photographed on separate plates and later compared with the latter to "spot" the actinium lines.

The actinium came partly from the original preparation and partly as a return of a loan to another site; the total weight was 2.7 mg. For loading electrodes, a solution method with porous electrodes, made by briquetting 70 percent of Ag or Cu powder with 30 percent of NH_4Cl, was developed. The NH_4Cl was sublimed off at about 300° C, leaving an electrode that soaked up solution like blotting paper. The electrodes were 1.5 mm in diameter and were porous for 0.5 mm from the end. It was necessary to add solution to the electrode in increments of 0.001 ml, which was done with a jig holding the electrode and a capillary pipet controlled by a small plunger operated by a dial indicator. We are indebted to Ruth Sjoblom of the ANL for assistance in the chemical purification and handling of the sample. Because it was not considered feasible in this case to remove the daughters, which supply the penetrating radiation, the electrodes were loaded by remote control from behind a 2-in. lead shield.

Each of the 4 exposures, 2 a-c arc and 2 spark, consumed approximately ½ mg of actinium, and lasted about 1 min. The range of wavelengths from 2000 to 11000 A was covered with four varieties of Eastman Kodak spectroscopic plates—103a-F (UV) for ultraviolet, 103a-F for near ultraviolet and visible, I–N for red and adjacent infrared, and I–Q for longer waves. Because the grating was blazed for 4000 A, the spectra were satisfactory between 2000 and 7000 A, but only 5 actinium lines (7290,

7567, 7617, 7866, and 7886 A) of greater wavelength were weakly recorded. The infrared spectrum was sacrificed in order to obtain maximum information in the region of most interest. Because the sample size was limited, it was felt that there would be a net gain over the use of an unblazed grating in the number of weak lines revealed.

The actinium spectra were much stronger on silver electrodes than on copper, but most of the lines appeared on both, and it appears probable that actinium spectra are now well known from 2500 to about 7000 A. In particular, the comparison of arc and spark intensities removed all doubt about sorting the lines belonging to Ac I, Ac II, and Ac III, as shown in table 1. A few lines with short wavelengths may belong to Ac IV. Typical portions of the arc and spark spectra emitted by silver electrodes charged with actinium are reproduced in figures 2 and 3; the "spotted lines" belong mostly to actinium.

A major difficulty in arriving at a definitive list of

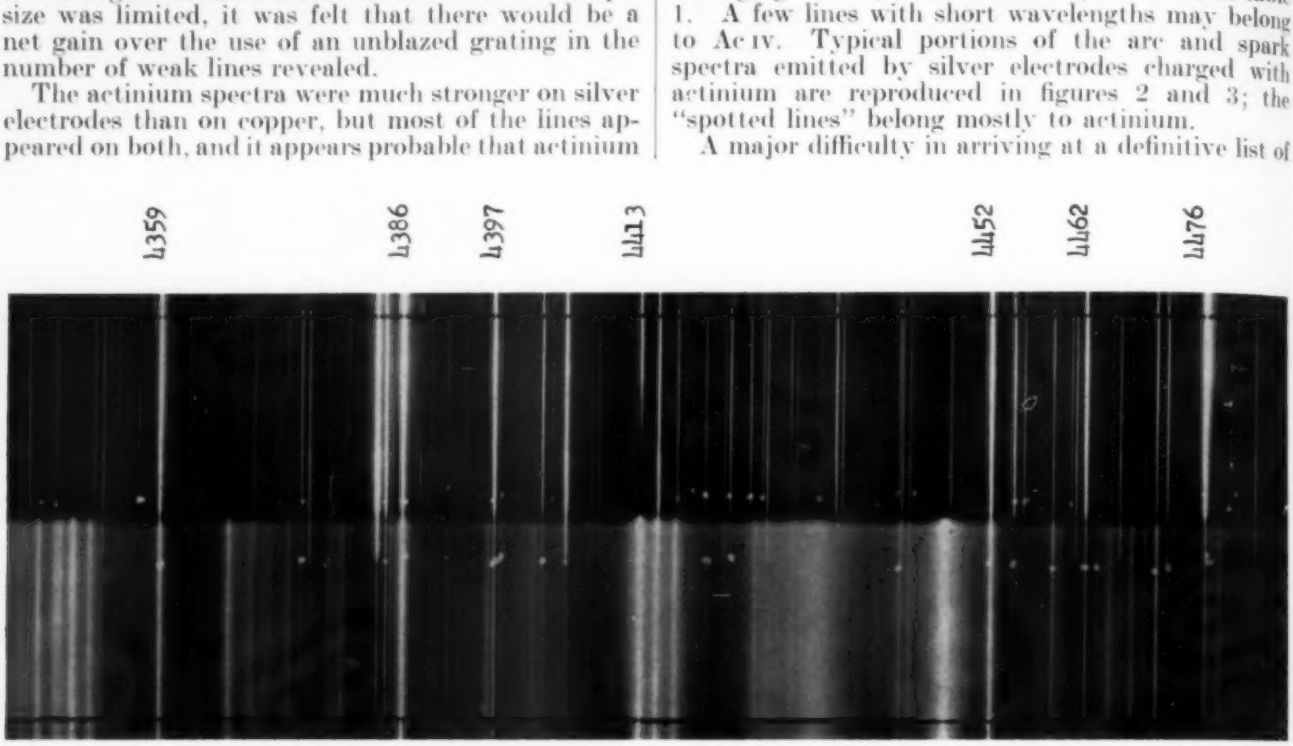

FIGURE 2. *Emission spectra of 0.5 mg of actinium of silver electrodes.*

Upper a-c arc spectrum; lower, high-voltage spark spectrum. 4397, 4462, 4476 A belong to Ac I; 4359, 4386, 4452 A represent Ac II; and 4413 A is characteristic of Ac III.

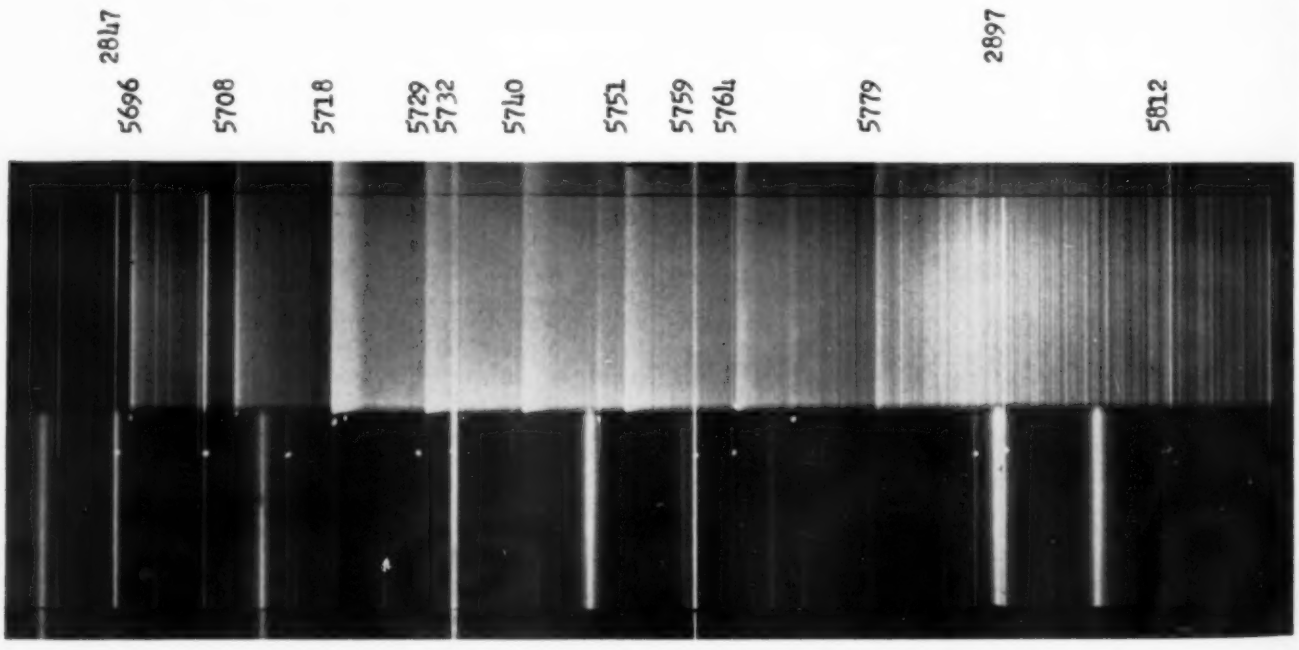

FIGURE 3. *Emission spectra of 0.5 mg of actinium on silver electrodes.*

Upper, a-c arc spectrum; lower, high-voltage spark spectrum. 5812 A belongs to Ac I; 2847, 2897, 5732, and 5759 A represent Ac II; but 5696, 5708, 5718, 5729, 5740, 5751, 5764, and 5779 A are band heads of AcO.

actinium lines is to eliminate the impurities. Despite careful chemical separation and handling, the observed spectra of actinium on silver and copper electrodes showed the stronger lines of sodium, potassium, calcium, strontium, barium, magnesium, zinc, aluminum, silicon, iron, chromium, nickel, manganese, palladium, platinum, lanthanum, radium, and lead. The first six named might have been present in chemical reagents; iron, chromium, and nickel, or palladium and platinum, or aluminum and silicon, suggest erosion of chemical ware, whereas radium and lead are expected as decay products of actinium. The greatest number of impurity lines were identified with iron, and the next greatest with lanthanum, the source of which is unknown.

The final data on emission spectra of actinium are presented in table 1, in which the literal symbols accompanying intensity numbers have the following meanings: *c*, complex; *d*, double; *e*, enhanced at electrode; *h*, hazy; *H*, very hazy; *l*, shaded to longer waves; *s*, shaded to shorter waves; and *B*, molecular band. The wavelengths in column 1 of table 1 are the means of 2 to 13 measurements on different spectrograms, except a few cases where the line was classified, although observed only once; other singly observed lines were omitted because they lacked confirmation. The probable error in any wavelength is usually less than 0.01 A; this is shown by consistent agreement of different measurements and by the close fit of classified lines. Some Ac lines have hyperfine structure extending over 0.3 A, or more, but only mean wavelengths are given for these because the hyperfine structures are ignored in spectral-term analyses. The analyses and interpretations of Ac III, Ac II, and Ac I spectra will now be given in succession, thus proceeding from the relatively simple case of the 1-valence electron, producing doublet terms, to the 2-electron spectrum of singlet and triplet terms, and finally to the 3-electron spectrum of doublet and quartet multiplicities.

TABLE 1. *Emission spectra of actinium*

Wavelength	Intensity in silver		Intensity in copper		Intensity in hollow cathode	Spectrum	Wavelength	Intensity in silver		Intensity in copper		Intensity in hollow cathode	Spectrum
	Arc	Spark	Arc	Spark				Arc	Spark	Arc	Spark		
A							A						
2062.00	.....	40*h*	.....	20*h*	.....	IV?	2952.55	30*c*	4000*h*	...	2000*h*	.....	III
2064.28	.....	5*h*	.....	4*h*	.....	II	2958.49	2	10*hl*	.....	4*hl*	.....	II
2100.00	.....	20*h*	.....	8*h*	.....	II	2966.45	.....	5*h*	.....	.....	.....	II
2102.24	.....	2*h*	.....	1	.....	II	2968.82	5	.....	.....	.....	.....	I
2261.75	3	10	.....	4	.....	II	2972.49	6	10*c*	.....	4	.....	II
2307.50	.....	10*h*	.....	3*h*	.....	II	2994.17	200	400	40	200	60	II
2316.06	.....	2	.....	2	.....	II	2996.68	4	10*hl*	.....	8*hl*	.....	II
2344.87	.....	3	.....	2	.....	II	3001.88	10	40	1	20	1	II
2501.39	.....	2	.....	2	.....	II	3015.40	.....	10*h*	.....	4*h*	.....	II
2502.12	.....	50*h*	.....	30*h*	.....	IV?	3019.87	200*c*	300*c*	30	100	4*c*	II
2534.85	.....	5	.....	2	.....	II	3030.46	2	7*hl*	.....	2*h*	.....	II
2558.08	.....	200*h*	.....	100*h*	.....	IV?	3036.93	10	2	.....	.....	.....	I
2626.44	20*dc*	5000*h*	.....	1000*h*	.....	III	3043.30	200	1000	50	500	10*c*	II
2630.19	40	50	2	20	.....	II	3064.25	10	40*hl*	.....	7*hl*	1	II
2657.81	40*c*	100*c*	4	30*c*	2*c*	II	3069.36	80	400	10	200	5	II
2682.90	3*c*	400*h*	.....	50*h*	.....	III	3076.17	4	10	.....	5	.....	II
2705.61	.....	5*h*	.....	.....	.....	II	3076.44	30	3	10	3	20	I
2712.50	40	40	4	20	2	II	3076.87	20	40	2	10	.....	II
2713.72	20	30	.....	3	1	II	3078.07	40	300	10	100	.....	II
2726.23	20*c*	40	2	10	.....	II	3080.54	.....	10*h*	.....	3*h*	.....	II
2729.74	.....	20*h*	.....	5*h*	.....	II	3082.96	2	.....	.....	.....	.....	I
2753.15	7*c*	10*c*	.....	4*c*	.....	II	3084.85	6	20	1	7	.....	II
2758.37	2	3	.....	.....	.....	II	3086.04	70	300	5	100	7	II
2760.18	4	30*hl*	.....	10*h*	.....	II	3087.37	150	200	30	100	20*c*	II
2781.56	2	20*hl*	.....	10*h*	.....	II	3100.63	5	20	.....	5	.....	II
2788.64	.....	5	.....	.....	.....	II	3109.33	8	.....	3	.....	.....	I
2790.83	.....	20*H*	.....	5*H*	.....	IV?	3111.57	50	5	10	3	30	I
2793.90	.....	200*Hw*	.....	50*Hw*	.....	IV?	3112.83	300	400	40	200	6	II
2797.59	15	40	1	20	3	II	3118.78	10	40	2	20	1	II
2798.05	.....	6*h*	.....	2*h*	.....	II	3120.16	200	300	20	100	6	II
2806.76	20	50	2	20	.....	II	3132.04	3	5	.....	2	.....	II
2826.27	2	6	.....	2	.....	II	3140.72	10	.....	3	.....	.....	I
2831.56	1	6	.....	4	.....	II	3143.71	100	10	20	10	80	I
2833.47	5	20	.....	8	.....	II	3153.09	500*c*	1000*c*	100	500	80*cs*	II
2847.16	50	300*hl*	10	150*h*	.....	II	3154.15	.....	.....	.....	4	.....	II
2856.73	.....	20*h*	.....	5*h*	.....	II	3154.41	600	1000*c*	100	600*c*	60*cs*	II
2864.11	.....	4*h*	.....	2	.....	II	3158.88	4	10*hl*	.....	2*h*	.....	II
2895.20	6	20	1	8	1	II	3163.01	.....	5*h*	.....	.....	.....	II
2896.82	50*c*	100*c*	6	30*c*	.....	II	3164.81	300	500*cs*	30	200*c*	10*cs*	II
2905.81	.....	6*h*	.....	.....	.....	II	3171.17	150	15	20	6	60	I
2923.02	80	100	3	30	.....	II	3174.23	20	2	3	1	5	I
2924.12	10	20	1	5	.....	II	3174.69	10	1	.....	.....	.....	I
2931.46	.....	20*hl*	.....	7*hl*	.....	II	3176.83	9	30	1	7	.....	II
2935.80	2	5	.....	3	.....	II	3179.52	3	.....	.....	.....	.....	I
2944.42	.....	5	.....	3	.....	II	3182.52	10	1	3	.....	2	I

TABLE 1. *Emission spectra of actinium*—Continued

Wavelength Å	Intensity in silver: Arc	Intensity in silver: Spark	Intensity in copper: Arc	Intensity in copper: Spark	Intensity in hollow cathode	Spectrum
3193.68	.....	.....	.....	2	.....	II
3202.12	4	20	1	10	.....	II
3204.87	5c	40cn	1	20cn	.....	II
3211.99	10	20	2	10	.....	II
3216.45	10	1	.....	.....	5	I
3219.08	20	100h	2	50h	2	II
3221.49	5	20	.....	6	.....	II
3224.7	.....	60*H*	.....	20*H*	.....	IV?
3226.14	2	9	.....	3	.....	II
3228.67	2	7	.....	2	.....	II
3230.59	300cn	400cn	40	300	10cn	II
3237.70	200cn	300cn	20	150c	10cn	II
3238.39	.....	5h	.....	1h	.....	II
3239.73	7	20	.....	5	1	II
3239.86	20	100	2	50	2	II
3247.79	4	20	.....	.....	.....	II
3249.48	3	10	.....	5c	.....	II
3253.84	4c	30cl	.....	6cl	.....	II
3257.77	4	.....	.....	.....	.....	I
3259.49	5	30	.....	6	.....	II
3260.91	500	1000	50	500	80	II
3281.65	?	40	?	20	2	II
3288.90	15	3	4	1	10	I
3297.14	.....	5h	.....	2h	.....	II
3301.93	.....	?	.....	4c	.....	II
3302.37	5	.....	.....	1	30	I
3303.28	20	2	?	2	10	I
3311.60	.....	6h	.....	2h	.....	II
3318.01	200	300	30	100c	6cn	II
3320.65	30	1	5	.....	15	I
3322.29	20	40	2	20	2	II
3328.01	10	30	2	20	2	II
3330.26	5	?	.....	.....	2	I
3331.50	4	20	.....	8	1	II
3341.25	1	6*hl*	.....	5h	.....	II
3342.31	2	5h	.....	4h	.....	II
3343.04	2	10h	.....	7h	.....	II
3350.06	5	.....	.....	.....	.....	I
3359.68	2	6	.....	3	.....	II
3361.19	2	5h	.....	5	.....	II
3380.96	10	.....	?	3	.....	I
3383.53	200c	400	20c	200	20cn	II
3388.51	1	6	.....	5	.....	II
3398.85	3c	10c	.....	8cl	.....	II
3391.41	3	.....	.....	.....	4	I
3392.78	20*dc*	3000*dh*	10c	2000*dh*	10*d*	III
3396.92	.....	20*hl*	.....	10*h*	.....	II
3402.11	.....	5h	.....	4h	.....	II
3413.84	300	400	30	200	60	II
3416.29	15	3	.....	.....	10	I
3417.77	500	600	100	500	200	II
3439.25	3	8	.....	6	.....	II
3440.40	4	20	?	15	2	II
3446.25	30	2	20	2	.....	I
3460.77	10	30	2	20	2	II
3481.16	500	1000	100	500c	200cn	II
3481.56	3	10	.....	5	.....	II
3483.25	9	20	.....	8	.....	II
3487.59	40	4000	10	3000	15	III
3489.53	300	400	50	200	100	II
3491.47	.....	3h	.....	2h	.....	II
3499.75	15	20	2	8	.....	II
3506.25	6	1	.....	1	.....	I
3513.73	2	50*hl*	.....	20*hl*	4c	II
3516.97	5	20*hl*	.....	8*hl*	1	II
3527.31	50	200	?	60	20	II
3529.24	50	200	10	100	15	II
3532.14	5	15	.....	4	.....	II
3533.98	5	10h	.....	4h	.....	II
3534.63	50	250	10	100	15	II
3545.44	3	10	.....	5	.....	II
3546.83	4	15	.....	5	.....	II
3547.07	.....	.....	.....	2	.....	II
3549.47	5	1	.....	.....	.....	I
3552.55	2	10*hl*	.....	5*hl*	.....	II
3554.99	300	400	100	200	10cn	II
3562.33	6	30	.....	10	2	II
3565.59	1000	2000	200	1000	150cn	II
3579.53	5	15*hl*	.....	10*hl*	.....	II
3583.55	5	30*hl*	.....	15*hl*	.....	II
3585.09	10	40	3	20	2c	II
3588.31	2	5	.....	3	.....	II
3595.75	5	20	.....	10	.....	II
3600.24	3	4	.....	.....	.....	II
3643.62	4	8*hl*	.....	5*hl*	.....	II
3644.42	4	.....	.....	.....	.....	I
3653.49	2	.....	.....	.....	.....	I
3660.32	.....	4h	.....	3h	.....	II
3662.04	1	5h	.....	3h	.....	II
3662.35	5	.....	.....	.....	.....	I
3664.69	3	10	.....	6	.....	II
3669.88	1	4h	.....	3h	.....	II
3679.69	.....	4h	.....	4h	.....	II
3683.66	20	30	6	20	6c	II
3685.17	.....	2	.....	2	.....	II
3690.67	.....	10*hl*	.....	10*hl*	.....	II
3692.36	5	.....	.....	.....	.....	I
3694.88	50	150	15	100	20	II
3701.30	80	10	20	5	100	I
3704.32	6	9	.....	6	.....	II
3709.03	?	3	.....	2	.....	II
3710.28	2	3	.....	3	.....	II
3711.82	.....	3h	.....	4h	.....	II
3713.00	3	6	.....	6	.....	II
3713.17	.....	6h	.....	5h	.....	II
3725.22	4	1	.....	.....	2	I
3734.47	.....	5h	.....	.....	.....	II
3735.95	5	.....	.....	.....	.....	I
3736.55	.....	4h	.....	3h	.....	II
3740.67	.....	2	.....	2	.....	II
3747.25	2	5	.....	3	.....	II
3754.18	5	15	.....	10	.....	II
3756.67	400c	500c	60c	300cn	80cn	II
3761.24	5	20	.....	8	10	II
3767.80	30	?	.....	.....	.....	I
3769.82	6	20	.....	20	.....	II
3771.21	.....	2h	.....	2h	.....	II
3771.64	2	10h	.....	8	1	II
3772.14	.....	7h	.....	6	.....	II
3774.31	.....	2	.....	2	.....	II
3777.80	.....	3h	.....	2h	.....	II
3784.01	.....	6h	.....	4h	.....	II
3788.66	.....	2h	.....	2h	.....	II
3795.86	10	2	.....	2	20	I
3796.02	.....	2	.....	2	.....	II
3799.82	100	200	?	200	30	II
3805.05	2	40*hl*	.....	20*hl*	.....	II
3809.52	.....	6h	.....	5h	.....	II
3814.36	40	10	6	4	.....	I
3814.78	.....	5*hl*	.....	5h	.....	II
3832.72	.....	2	.....	2	.....	II
3834.80	3	30*hl*	.....	20*hl*	.....	II
3835.32	100	8	20	3	150	I
3843.04	300	20	100	10	600c	I
3850.91	.....	5*hl*	.....	10*hl*	.....	II
3858.80	.....	2	.....	2	.....	II
3863.12	1000cn	2000c	200c	2000c	200cn	II
3877.03	.....	4	.....	4	.....	II
3879.82	.....	2h	.....	1h	.....	II
3885.56	400	40	100	30	400c	I
3893.35	20	50*hl*	?	20*hl*	.....	II
3907.38	.....	.....	.....	4h	.....	II
3914.47	100	200	20	100	100c	II
3920.10	10	50	?	30	5	II
3922.73	.....	6h	.....	6h	.....	II
3928.39	2	10*hl*	.....	10*hl*	.....	II
3929.52	5	.....	.....	.....	.....	I
3938.58	.....	10h	.....	10h	.....	II
3946.59	.....	3h	.....	4h	.....	II
3951.98	4	20*hl*	.....	10*hl*	.....	II
3965.07	.....	5h	.....	4h	.....	II
3972.49	.....	4h	.....	4h	.....	II
3977.36	40	100	6	80	8	II
3999.36	20	50*hl*	3	30*hl*	2	II
4002.23	.....	10*hl*	.....	10*hl*	.....	II
4003.79	3	.....	.....	.....	.....	I
4004.64	20	3	4	2	.....	I
4005.47	5	10	.....	7	.....	II
4015.22	30	3	3	.....	.....	I
4019.64	30	80	3	50	20	II

TABLE 1. *Emission spectra of actinium*—Continued

Wavelength	Intensity in silver		Intensity in copper		Intensity in hollow cathode	Spectrum
	Arc	Spark	Arc	Spark		
Å						
4023.09	3	5	.....	4	.....	II
4031.95	40	5	5	3	7c	I
4034.63	200	30	60	10	80c	I
4037.15	.....	4h	.....	3h	.....	II
4038.93	.....	?	.....	2h	.....	II
4044.45	3	30hl	.....	20hl	.....	II
4050.06	.....	2	.....	2	.....	II
4053.06	5	20hl	.....	15hl	1	II
4057.36	.....	4h	.....	4h	.....	II
4058.38	.....	2h	.....	3	.....	II
4061.60	400c	500c	100	400	400cs	II
4063.10	200	20	?	10	200c	I
4078.70	150	200	40	200	50c	II
4081.04	5	.....	.....	.....	.....	I
4081.77	.....	2h	.....	4h	.....	II
4087.76	20	1	5	1	.....	I
4088.44	2000cs	3000cs	200c	3000c	300cs	II
4113.77	80	4	15	5	50cl	I
4113.86	5	10	.....	8	.....	II
4132.42	10	20	2	20	1	II
4136.22	2	5	.....	4	.....	II
4137.99	10	40hl	2	40hl	5c	II
4139.65	20c	2	3c	.....	.....	I
4144.15	3	10	.....	10	.....	II
4152.88	.....	?	.....	1h	.....	II
4168.40	1500cs	2000cs	300c	3000cs	200cs	II
4169.12	.....	.....	.....	2	.....	II
4179.98	1000	50	200	100	1000	I
4183.12	500	20	50	20	800	I
4184.17	6	.....	2	.....	.....	I
4186.05	15	2	4	.....	.....	I
4188.08	2	8hl	.....	7hl	.....	II
4189.75	2	40h	.....	10h	3	II
4194.40	400	20	50	20	400	I
4198.72	30	3	5	2	20	I
4201.92	30c	3	.....	3c	8cs	I
4202.79	.....	2	.....	2	.....	II
4205.70	10	1	.....	.....	3	I
4208.91	50	5	15	5	40c	I
4209.69	80	300	40	300	200cs	II
4218.02	50	5	10	4	20cl	I
4225.99	80	3	10	4	100	I
4232.67	10	20	3	20	2	II
4234.61	10c	2c	.....	.....	3c	I
4246.33	20	3	4	2	.....	I
4246.78	10	1	2	.....	.....	I
4257.82	.....	50hl	.....	40hl	.....	II
4259.65	6	20	.....	20h	.....	II
4261.10	10cl	20cl	.....	6cl	.....	II
4261.67	5	10	.....	10h	.....	II
4262.42	40	3	5	3	.....	I
4266.94	50	4	6	3	.....	I
4268.21	20	40	4	30	.....	II
4294.62	10	.....	.....	.....	.....	I
4311.64	3	10hl	.....	10hl	.....	II
4327.24	1	5	.....	5	.....	II
4336.27	20	2	3	2	3	I
4337.13	20	30	?	20	.....	II
4347.51	10c	?	2c	.....	.....	I
4359.13	300	400	100	300	100	II
4364.08	2	3	.....	.....	.....	II
4375.07	20	3	3	2	.....	I
4384.53	300c	30c	80	20c	150cl	I
4386.41	500	1500	100	1000	100cl	II
4391.43	.....	6	.....	3	.....	II
4396.71	400	30	100	20	200	I
4397.45	3	5	.....	3	.....	II
4402.11	100	10	10	4	10c	I
4413.09	40c	3000h	2	2000h	.....	III
4417.26	30	2	3	.....	2	I
4420.42	20	2	3	3	4	I
4423.15	40	2	4	.....	3	I
4426.85	15	.....	2	.....	.....	I
4442.05	5	20	1	7	.....	II
4452.19	600	700	200	500	50cs	II
4461.16	10	.....	.....	.....	3	I
4462.73	400	50	80	20	300c	I
4467.90	3	10	.....	1	.....	II
4470.59	20	50	3	20	3	II
4471.81	80	5	7	5	20	I

Wavelength	Intensity in silver		Intensity in copper		Intensity in hollow cathode	Spectrum
	Arc	Spark	Arc	Spark		
Å						
4486.63	20	1	2	.....	2c	I
4487.60	40	3	6	3	5c	I
4507.20	2000cl	2000cl	1000cl	1000cl	150cl	II
4511.23	10	15	2	8	.....	II
4526.27	10c	15c	.....	2	.....	II
4539.29	.....	3	.....	.....	.....	II
4544.09	50	100	3	40	.....	II
4552.18	100c	5c	.....	.....	15c	I
4557.28	15	1	2	2	.....	I
4569.87	50c	4000h	5h	3000h	.....	III
4578.24	50	3	5	2	8	I
4585.83	.....	3h	.....	.....	.....	II
4605.45	1000	1000	200	500c	100c	II
4610.10	100	5	15	5	10	I
4611.59	4	.....	.....	.....	.....	I
4613.93	300	20	30	.....	100c	I
4621.69	60	3	8	.....	10c	I
4682.16	100c	6c	6c	4c	.....	I
4684.91	.....	6h	.....	1	.....	II
4690.52	60	4	8c	3c	15c	I
4693.29	10	1	.....	.....	4	I
4705.78	200c	10c	15c	5c	30cs	I
4707.97	60c	5c	10c	7c	10cs	I
4716.58	500	20	50	10	200c	I
4716.74	10	20	2	10	.....	II
4720.16	1000	1000	200c	400c	100cs	II
4740.51	50	200	10	100	5	II
4776.77	10c	2c	.....	.....	6c	I
4786.96	10c	2c	.....	.....	2c	I
4807.83	60	100	15c	20	10c	II
4808.81	10	3	.....	.....	5c	I
4811.06	5	15	.....	2	.....	II
4812.22	500	600	100	300	150c	II
4825.88	40	?	4	.....	.....	I Ra?
4855.68	50c	4	8	4	6c	I
4860.16	150c	10	30	10	60c	I
4868.87	20	3	5	3	3	I
4876.14	3Bl	.....	.....	.....	.....	AcO
4876.31	10Bl	.....	.....	.....	.....	AcO
4879.58	4Bl	.....	.....	.....	.....	AcO
4879.74	20Bl	.....	.....	.....	.....	AcO
4889.10	50	80	7	30	.....	II
4945.18	150	200	20	100	8c	II
4958.23	200	200	40	100	6c	II
4960.87	100	150	20	100	4	II
4963.48	10c	.....	.....	.....	3c	I
4981.55	10	20	.....	7	.....	II
5061.56	5	.....	.....	.....	4c	I
5064.65	6	.....	.....	.....	2	I
5065.07	3	7	.....	3	.....	II
5105.83	30c	1	.....	.....	30cs	I
5156.53	40	60	5	20	4	II
5164.83	4	4	.....	3	.....	II
5193.21	.....	30h	.....	8h	.....	III
5215.40	20	30	.....	10	.....	II
5228.31	60	2	8	2	.....	I
5229.10	5	10	.....	4	.....	II
5230.43	40cl	60cl	.....	15cl	6cl	II
5256.03	7c	7c	.....	3	.....	II
5258.24	300c	20c	60c	10c	200c	I
5261.45	40c	2c	7c	2c	6c	I
5264.48	50	2	7	.....	10	I
5271.56	150	8	30	5	100	I
5273.13	.....	2	.....	1	.....	II
5344.74	100	4	15	5	30	I
5362.61	60	60	7	20	4c	II
5369.63	10	.....	.....	.....	3	I
5424.44	8cl	.....	.....	.....	8cl	I
5430.96	20cs	2c	.....	2	10cs	I
5446.38	300	400	50	150	9	II
5471.71	?	?	.....	5	.....	II
5548.98	7c	9c	.....	2	4c	II
5569.26	200c	10c	40c	5c	200c	I
5573.16	.....	3h	.....	1h	.....	II
5603.77	10	25	1	10	.....	II
5610.90	7c	1c	.....	.....	4cl	I
5618.77	40	4	8	4	5	I
5625.92	.....	3	.....	3	.....	II
5627.57	10	20	2	20	1	II
5636.60	100c	4c	20c	4c	80c	I

TABLE 1. *Emission spectra of actinium*—Continued

Wavelength	Intensity in silver		Intensity in copper		Intensity in hollow cathode	Spectrum
	Arc	Spark	Arc	Spark		
A						
5660.19	40*c*	2*c*	10*c*	2*c*	15	I
5660.93	.....	2*h*	.....	4*h*	.....	II
5663.34	10	20	2	20	1	II
5674.15	80*cl*	5*c*	15*c*	3*c*	15	I
5695.90	10*Bl*	.....	3*Bl*	.....	.....	AcO
5696.12	20*Bl*	.....	4*Bl*	.....	.....	AcO
5707.54	10*Bl*	.....	3*Bl*	.....	.....	AcO
5707.76	10*Bl*	.....	3*Bl*	.....	.....	AcO
5718.44	100*Bl*	1	40*Bl*	1	.....	AcO
5718.66	200*Bl*	2	60*Bl*	2	8*III*	AcO
5728.94	90*Bl*	.....	30*Bl*	.....	.....	AcO
5729.15	180*Bl*	.....	50*Bl*	.....	6*III*	AcO
5732.05	200*cl*	200*cl*	100*cl*	300*cl*	60*cl*	II
5739.78	80*Bl*	.....	20*Bl*	.....	.....	AcO
5740.00	150*Bl*	.....	40*Bl*	.....	5*III*	AcO
5751.18	60*Bl*	.....	10*Bl*	.....	.....	AcO
5751.41	120*Bl*	.....	20*Bl*	.....	5*III*	AcO
5758.97	300*c*	400*c*	50*c*	400*c*	40*c*	II
5763.64	40*Bl*	.....	7*Bl*	.....	.....	AcO
5763.88	80*Bl*	.....	10*Bl*	.....	4*III*	AcO
5779.27	20*Bl*	.....	3*Bl*	.....	.....	AcO
5779.54	40*Bl*	.....	5*Bl*	.....	4*III*	AcO
5812.44	30*d*	2*d*	5*d*	2	40*c*	I
5813.45	.....	5*h*	.....	6*h*	.....	II
5830.55	10	.....	.....	.....	.....	I
5901.10	.....	2	.....	3	.....	II
5905.14	10	7	5	40	1	II
5910.85	1000*c*	1000*c*	200*c*	1000*c*	400*c*	II
5952.86	8*c*	.....	.....	.....	4*c*	I
5957.47	10*c*	2*c*	.....	.....	10*c*	I
5997.40	2*Bl*	.....	.....	.....	.....	AcO
5997.66	4*Bl*	.....	.....	.....	.....	AcO
6006.27	5	9	1	10	2	II
6008.88	2*Bl*	.....	.....	.....	.....	AcO
6009.15	5*Bl*	.....	.....	.....	.....	AcO
6021.59	1*Bl*	.....	.....	.....	.....	AcO
6021.87	5*Bl*	.....	.....	.....	.....	AcO
6026.14	10*c*	1*c*	1*c*	2	2*cs*	I
6109.98	5*c*	.....	.....	.....	3*c*	I
6154.33	9*c*	1*c*	.....	.....	8*c*	I
6161.48	2	2	.....	.....	.....	II
6164.75	500*c*	600*c*	100*c*	600*c*	200*cl*	II
6167.83	50*cl*	100*cl*	10*c*	200*c*	20*cl*	II
6170.18	5*c*	.....	.....	.....	.....	I
6173.35	3	4	.....	4	.....	II
6181.74	15	40	.....	30	1	II
6242.83	300*c*	300*c*	40*c*	400*c*	10*c*	II
6257.12	3*c*	.....	.....	.....	3*c*	I
6275.67	10*cs*	2*c*	.....	.....	3*c*	I
6340.10	15*cs*	1*c*	.....	.....	10*cs*	I
A						
6359.86	300*c*	20*c*	60*c*	20*c*	500*c*	I
6387.39	.....	2	.....	2	.....	II
6424.58	.....	3*h*	.....	2*h*	.....	II
6447.82	40*c*	2*c*	7*c*	1*c*	50*c*	I
6469.68	50*cl*	3*c*	10*cl*	.....	60*cl*	I
6477.35	1*Bl*	.....	.....	.....	.....	AcO
6477.62	2*Bl*	.....	.....	.....	.....	AcO
6494.02	2*Bl*	.....	.....	.....	.....	AcO
6494.25	2*Bl*	.....	.....	.....	.....	AcO
6508.64	1*Bl*	.....	.....	.....	.....	AcO
6508.93	3*Bl*	.....	.....	.....	.....	AcO
6524.70	2*Bl*	.....	.....	.....	.....	AcO
6524.99	6*Bl*	.....	.....	.....	.....	AcO
6535.81	10	15	3	6	.....	II
6541.17	3*Bl*	.....	.....	.....	.....	AcO
6541.53	3*Bl*	.....	.....	.....	.....	AcO
6557.73	2*Bl*	.....	.....	.....	.....	AcO
6558.04	5*Bl*	.....	.....	.....	.....	AcO
6575.03	3*Bl*	.....	.....	.....	.....	AcO
6575.40	3*Bl*	.....	.....	.....	.....	AcO
6618.19	10	1	2	1	.....	I
6660.08	2*Bl*	.....	.....	.....	.....	AcO
6660.44	4*Bl*	.....	.....	.....	.....	AcO
6691.27	200*cl*	20*cl*	50*cl*	20*cl*	300*c*	I
6695.23	150	200	20	100	20	II
6757.29	3*Bl*	.....	.....	.....	.....	AcO
6757.62	4*Bl*	.....	.....	.....	.....	AcO
6773.30	2*Bl*	.....	.....	.....	.....	AcO
6773.66	3*Bl*	.....	.....	.....	.....	AcO
6789.99	2*Bl*?	.....	.....	.....	.....	AcO
6800.22	5*Bl*	.....	.....	.....	.....	AcO
6800.55	10*Bl*	.....	.....	.....	.....	AcO
6815.00	3*Bl*	.....	.....	.....	.....	AcO
6815.32	3*Bl*	.....	.....	.....	.....	AcO
6830.23	2*Bl*	.....	.....	.....	.....	AcO
6830.60	5*Bl*	.....	.....	.....	.....	AcO
6845.95	2*Bl*	.....	.....	.....	.....	AcO
6846.25	3*Bl*	.....	.....	.....	.....	AcO
6861.67	3*Bl*	.....	.....	.....	.....	AcO
6877.64	2*Bl*	.....	.....	.....	.....	AcO
6893.73	2*Bl*	.....	.....	.....	.....	AcO
6933.99	10*c*	15*c*	.....	15*c*	6*c*	II
6996.09	.....	.....	.....	2	.....	II
7290.40	10*c*	.....	.....	6*c*	300*c* 4	I
7567.65	4	4	.....	.....	20*c* 4	II
7617.42	.....	2	.....	.....	.....	II
7866.10	2*cl*	.....	.....	.....	200*cl*	I
7886.82	.....	3	.....	.....	.....	II

3. Spectrum of Doubly Ionized Actinium (Ac III)

Among hundreds of actinium lines there were 8 that clearly comprised a distinctive group; they were weakly excited only at 1 electrode of the arc, and enormously enhanced and hazy in the spark. These lines exhibited the same characteristics as Y III [5] and La III [6] lines; they were naturally assigned to Ac III. When the vacuum wave numbers of these Ac III lines were subtracted from each other the differences, 801.0, 3402.9, and 8597.1 occurred twice. A clue to the correct interpretation of these differences was found in the hyperfine structure of two of the lines. The two Ac III lines, with wavelengths 2626.44 and 3392.78 A, are narrow doublets with equal separation of 1.73 K. This suggested that the duplicity arises from interaction of a penetrating electron with the atomic nucleus, and that the number of observed components is limited by the J-value of the former rather than the I-value of the latter. In other words, these two lines must be interpreted as transitions from two excited levels, $7p\ ^2P^\circ_{0\frac{1}{2},1\frac{1}{2}}$, separated 8597.1 K, to a common ground level, $7s\ ^2S_{0\frac{1}{2}}$. The constant difference, 801.0 K, is then seen to be the separation of $7s\ ^2S_{0\frac{1}{2}}$ and $6d\ ^2D_{1\frac{1}{2}}$, and the difference 3402.9 K is the interval of the $6d\ ^2D_{1\frac{1}{2},2\frac{1}{2}}$ term.

The atomic-energy levels derived from this analysis of the Ac III spectrum are displayed in table 2.

The known lines of Ac III are collected in table 3.

When this material on Ac III was being assembled for publication, attention was directed to a 20-year-old note by R. J. Lang [13], who estimated, from information available for Ra II and Th IV spectra, that the separation of the $7p\ ^2P^\circ$ levels of Ac III cannot be very different from 8,300 cm^{-1}, and that the two strong lines, $7s\ ^2S_{0\frac{1}{2}}$–$7p\ ^2P^\circ_{0\frac{1}{2},1\frac{1}{2}}$, will occur in the neighborhood of 2650 and 3450 A. These estimates

TABLE 2. *Terms in the* Ac III *spectrum*

Configuration	Designation	J	Level	Interval
$6p^6(^1S)7s$	$7s\ ^2S$	$0\frac{1}{2}$	0. 0	
$6p^6(^1S)6d$	$6d\ ^2D$	$1\frac{1}{2}$	801. 0	3402. 9
	$6d\ ^2D$	$2\frac{1}{2}$	4203. 9	
$6p^6(^1S)5f$	$5f\ ^2F°$	$2\frac{1}{2}$	*23454. 5*	2625. 7
	$5f\ ^2F°$	$3\frac{1}{2}$	*26080. 2*	
$6p^6(^1S)7p$	$7p\ ^2P°$	$0\frac{1}{2}$	*29465. 9*	8597. 1
	$7p\ ^2P°$	$1\frac{1}{2}$	*38063. 0*	

TABLE 3. *Classified lines of* Ac III

Wavelength	Intensity		Wave number	Term combinations
	Arc	Spark		
A			*K*	
2626. 44	20*de*	5000*hd*	38063. 00	$7s\ ^2S_{0\frac{1}{2}} - 7p\ ^2P°_{1\frac{1}{2}}$
2682. 90	3*e*	400*h*	37262. 03	$6d\ ^2D_{1\frac{1}{2}} - 7p\ ^2P°_{1\frac{1}{2}}$
2952. 55	30*e*	5000*h*	33859. 13	$6d\ ^2D_{2\frac{1}{2}} - 7p\ ^2P°_{1\frac{1}{2}}$
3392. 78	20*de*	3000*hd*	29465. 90	$7s\ ^2S_{0\frac{1}{2}} - 7p\ ^2P°_{0\frac{1}{2}}$
3487. 59	50*e*	4000*h*	28664. 89	$6d\ ^2D_{1\frac{1}{2}} - 7p\ ^2P°_{0\frac{1}{2}}$
4413. 09	40*e*	3000*h*	22653. 50	$6d\ ^2D_{1\frac{1}{2}} - 5f\ ^2F°_{2\frac{1}{2}}$
4569. 87	50*e*	4000*h*	21876. 33	$6d\ ^2D_{2\frac{1}{2}} - 5f\ ^2F°_{3\frac{1}{2}}$
5193. 21	------	30*h*	19250. 55	$6d\ ^2D_{2\frac{1}{2}} - 5f\ ^2F°_{2\frac{1}{2}}$

are indeed remarkably close to the truth. Lang also stated that the ionization potential will be close to 20 v, but the present authors were unable to derive a value from spectral series.

4. Spectrum of Singly Ionized Actinium (Ac II)

The second spectrum of actinium, like that of lanthanum, is relatively complex; it has strong lines with nearly equal intensity on arc and spark spectrograms, and many weaker lines with increasing intensity ratios of spark to arc, indicating higher excitation potentials. The first group includes transitions between low-energy even and odd levels, and the second represents transitions between high even and high odd levels, or between high odd and a second group of very high even levels. Because the Zeeman effect has not been investigated in actinium spectra, there is no direct way to determine J-values (from Zeeman components) or term designations (from magnetic splitting). This analysis of the Ac II spectrum is based on wave numbers and intensities, on the J selection rule, and on interval and intensity rules for spectral terms.

The lowest energy levels that can arise from s- and d-type electrons are identified with even spectral terms as follows:

Electron configuration	Spectral terms
s^2	^1S
$s\ d$	^1D, ^3D
d^2	^1S, ^1D, ^1G, ^3P, ^3F

All of these have been identified except $(d^2)^1S$, which is also unknown in the homologous spectra, Sc II, Y II, and La II. Which particular electron configuration or spectral term will have the lowest energy and represent the normal state of the atom depends on the relative strength of binding of the individual electrons. It is very remarkable that each of the homologous ions Sc^+, Y^+, and La^+, makes a different choice: the normal state of Sc^+ is $(sd)^3D$; of Y^+, $(s^2)^1S$; and of La^+, $(d^2)^3F$. It was naturally assumed that Ac^+ would closely resemble its nearest neighbor, La^+, but the analysis of Ac II has shown conclusively that the ground state of Ac^+ is $(s^2)^1S$, like that of Y^+, and the remaining low even terms occur also in the same relative order as for Y^+.

Substitution of a p-electron for an s- or a d-electron produces the following (odd) middle terms with 16 levels:

Electron configuration	Spectral terms
$s\ p$	$^1P°$ $^3P°$
$d\ p$	$^1P°$, $^1D°$, $^1F°$, $^3P°$, $^3D°$, $^3F°$

Transitions between these odd terms and the low even ones account for all the easily excited lines of Sc^+ and Y^+, but this was not true for La^+. It was concluded that additional odd terms occur in La^+ on account of the presence of f-type electrons. Thus, the substitution of f- for p-type electrons would yield the following additional (odd) middle terms with 24 levels:

Electron configuration	Spectral terms
$s\ f$	$^1F°$ $^3F°$
$d\ f$	$^1P°$, $^1D°$, $^1F°$, $^1G°$, $^1H°$, $^3P°$, $^3D°$, $^3F°$, $^3G°$, $^3H°$

All of these terms were found in the La II spectrum, and, with the exception of two levels ($J=5$, and 6), they have also been found in Ac II. The major

difference between these two spectra is that the 4*f*-electron is much more tightly bound in La^+ than the 5*f*-electron is in Ac^+. This will be discussed in more detail near the end of this paper. In addition to the above terms, Ac II has revealed a dozen high even levels that probably arise from the electron configuration *fp*, which, in *LS* notation, produces ^1D, ^1F, ^1G and ^3D, ^3F, ^3G.

The terms that have been identified from line intensities and level intervals in the Ac II spectrum are listed in table 4, in which successive columns contain electron configurations (and limits), term designations, *J* values, level values, and intervals between levels of complex terms. The low even terms from s^2, *ds*, and d^2 are complete excepting $d^2\ ^1S$. The middle odd terms from *sp* and *dp* are

TABLE 4. *Terms in the Ac II spectrum*

Configuration	Designation	*J*	Level	Interval	Configuration	Designation	*J*	Level	Interval
$7s^2$	$a\ ^1S$	0	0. 00		$6d(^2D)5f$	$z\ ^3H°$	4	*39807. 14*	1109. 27
$6d(^2D)7s$	$a\ ^3D$	1	4739. 63				5	*40916. 41*	
				527. 53					
		2	5267. 16		$6d(^2D)5f$	$x\ ^3F°$	2	*41578. 57*	1697. 28
				2159. 36					
		3	7426. 52				3	*43275. 85*	1764. 45
$6d(^2D)7s$	$a\ ^1D$	2	9087. 54				4	*45040. 30*	
$6d^2$	$a\ ^3F$	2	13236. 46		$6d(^2D)5f$	$z\ ^1G°$	4	*41627. 79*	
				1712. 75					
		3	14949. 21		$6d(^2D)7p$	$y\ ^1F°$	3	*41937. 05*	
				1807. 69					
		4	16756. 90		$6d(^2D)7p$	$y\ ^1P°$	1	*44199. 94*	
$6d^2$	$a\ ^3P$	0	17737. 10		$6d(^2D)5f$	$y\ ^1D°$	2	*44705. 33*	
				1278. 22					
		1	19015. 32		$6d(^2D)5f$	$z\ ^3G°$	3	*45807. 06*	1620. 61
				3184. 13					
		2	22199. 45				4	*47427. 67*	1723. 87
$6d^2$	$b\ ^1D$	2	19203. 02				5	*49151. 54*	
$6d^2$	$a\ ^1G$	4	20848. 23		$6d(^2D)5f$	$y\ ^3D°$	1	*48518. 41*	960. 64
$7s(^2S)7p$	$z\ ^3P°$	0	*20956. 40*				2	*49479. 05*	580. 65
				1224. 12					
		1	*22180. 52*				3	*50059. 70*	
				9698. 35					
		2	*31878. 87*		$6d(^2D)5f$	$x\ ^3P°$	0	*49780. 60*	455. 00
$6d(^2D)7p$	$z\ ^3F°$	2	*26446. 96*				1	*50235. 60*	1021. 91
				4727. 64					
		3	*31174. 60*				2	*51257. 51*	
				7944. 42					
		4	*39119. 02*		$6d(^2D)5f$	$x\ ^1F°$	3	*53255. 30*	
$7s(^2S)5f$	$y\ ^3F°$	2	*28201. 11*		$6d(^2D)5f$	$x\ ^1P°$	1	*56152. 2*	
				1679. 98					
		3	*29881. 09*		$7s(^2S)8s$	$e\ ^3S$	1	51680. 55	
				3084. 46					
		4	*32965. 55*		$7s(^2S)8s$	$e\ ^1S$	0	53374. 01	
$6d(^2D)7p$	$z\ ^3D°$	1	*29250. 40*		$5f(^2F_{5/2})7p_{1/2}$	$e\ ^3F$	2	54633. 05	
				4054. 56		$e\ ^3G$	3	54644. 11	
		2	*33304. 96*						
				3667. 98	$5f(^2F_{7/2})7p_{1/2}$	$e\ ^3G$	4	57683. 78	
		3	*36972. 94*			$e\ ^3D$	3	57944. 57	
$7s(^2S)7p$	$z\ ^1P°$	1	*33388. 61*		$5f(^2F_{5/2})7p_{3/2}$	$e\ ^3F$	3	59071. 9	
						$e\ ^3D$	2	59807. 51	
$6d(^2D)7p$	$z\ ^1D°$	2	*35397. 12*			$e\ ^1G$	4	59889. 05	
						$e\ ^3D$	1	60063. 0	
$7s(^2S)5f$	$z\ ^1F°$	3	*36144. 35*		$5f(^2F_{7/2})7p_{3/2}$	$e\ ^1F$	3	62350. 68	
$6d(^2D)7p$	$y\ ^3P°$	0	*36780. 01*			$e\ ^3F$	4	62869. 81	
				75. 49		$e\ ^1D$	2	63581. 56	
		1	*36855. 50*			$e\ ^3G$	5	65392. 46	
				1516. 14					
		2	*38371. 64*		Limit				97300

complete. The middle odd terms from *sf* and *df* electrons are also complete, excepting *df* $^1H_5^\circ$ and *df* $^3H_6^\circ$, for the following reasons: $^1H_5^\circ$ has only two possibilities of combining with low even levels, so that if one is unobserved the level is lost, whereas $^3H_6^\circ$ cannot combine with any known even levels for lack of any with $J=5$. Fourteen high even levels have been found between 51680 and 65392; the first two are interpreted as $7s(^2D)8s\ ^3S$ and ^1S, respectively; the remainder fall into four groups typical of *fp* in *jj* coupling.

The levels $7s^2\ a\ ^1S_0$ and $7s\ 8s\ e\ ^1S_0$ are the first two members of a series in which one of the 7*s* electrons acquires successively larger principal quantum numbers. This series may be represented by a Rydberg formula which leads to a limit of 98800 K, or an ionization potential of 12.2 ev. However, other spectra show that the Rydberg denominator n^* changes by more than one unit between the first and second members of this series. In Ra II, Rasmussen [14] found n^* to be 1.055, and if we assume it is the same in Ac II, the series limit is at 97300 K, and the principal ionization potential of Ac^+ is about 12.0 ev. This may be compared with 11.5 ± 0.4 ev obtained by Finkelnburg and Humbach [15] by their method of triple extrapolation.

Available data for the classified lines characteristic of singly ionized actinium atoms are presented in table 5, successive columns of which contain measured wavelengths, estimated intensities in the silver spark, vacuum wave numbers, and term combinations. Although table 5 contains only 76 percent of all Ac II lines in table 1, the classified lines account for 90 percent of the total intensity ascribed to Ac II.

TABLE 5. *Classified lines of* Ac II

Wavelength	Intensity	Wave number	Term combination	Wavelength	Intensity	Wave number	Term combination
A		*K*		*A*		*K*	
2261.75	10	44199.9	$a\ ^1S_0 - y\ ^1P_1^\circ$	3112.83	400	32115.8	$a\ ^3D_1 - y\ ^3P_1^\circ$
2344.87	3	42633.2	$a\ ^3D_3 - y\ ^3D_3^\circ$	3118.78	40	32054.5	$b\ ^1D_2 - x\ ^3P_2^\circ$
2501.39	2	39965.7	$a\ ^3D_1 - y\ ^1D_2^\circ$	3120.16	300	32040.4	$a\ ^3D_1 - y\ ^3P_0^\circ$
2534.85	5	39438.2	$a\ ^3D_2 - y\ ^1D_2^\circ$	3153.09	1000	31705.7	$a\ ^3D_2 - z\ ^3D_3^\circ$
2630.19	50	38008.7	$a\ ^3D_2 - x\ ^3F_3^\circ$	3154.15	4	31695.1	$z\ ^3F_3^\circ - e\ ^3F_4$
2657.81	100*c*	37613.8	$a\ ^3D_3 - x\ ^3F_4^\circ$	3154.41	1000	31692.47	$a\ ^3D_3 - z\ ^3F_4^\circ$
2705.61	5*h*	36949.3	$b\ ^1D_2 - x\ ^1P_1^\circ$	3163.01	5 *h*	31606.31	$y\ ^3F_2^\circ - e\ ^3D_2$
2712.50	40	36855.4	$a\ ^1S_0 - y\ ^3P_1^\circ$	3164.81	500 *cs*	31588.33	$a\ ^3D_2 - y\ ^3P_1^\circ$
2713.72	30	36838.9	$a\ ^3D_1 - x\ ^3F_2^\circ$	3176.83	30	31468.82	$a\ ^3F_2 - y\ ^1D_2^\circ$
2726.23	40	36669.8	$a\ ^3D_2 - y\ ^1F_3^\circ$	3202.12	20	31220.29	$a\ ^3P_1 - x\ ^3P_1^\circ$
2753.15	10*c*	36311.3	$a\ ^3D_2 - x\ ^3F_2^\circ$	3204.87	40 *cs*	31193.50	$z\ ^3P_1^\circ - e\ ^1S_0$
2758.37	3	36242.6	$a\ ^3F_2 - y\ ^3D_2^\circ$	3219.08	100 *h*	31055.81	$a\ ^3P_2 - x\ ^1F_3^\circ$
2788.64	5	35849.2	$a\ ^3D_3 - x\ ^3F_3^\circ$	3221.49	20	31032.57	$b\ ^1D_2 - x\ ^1P_1^\circ$
2806.76	50	35617.8	$a\ ^1D_2 - y\ ^1D_2^\circ$	3228.67	7	30963.57	$a\ ^3F_2 - y\ ^1P_1^\circ$
2833.47	20	35282.0	$a\ ^3F_2 - y\ ^3D_1^\circ$	3230.59	400 *cs*	30945.16	$a\ ^3D_3 - y\ ^3P_2^\circ$
2847.16	300*hl*	35112.4	$a\ ^1D_2 - y\ ^1P_1^\circ$	3237.70	300 *cs*	30877.21	$a\ ^3D_2 - z\ ^1F_3^\circ$
2895.20	20	34529.8	$a\ ^3F_3 - y^3D_2^\circ$	3238.39	5 *h*	30870.63	$y\ ^3F_3^\circ - e\ ^3F_3$
2896.82	100*c*	34510.5	$a\ ^3D_3 - y\ ^1F_3^\circ$	3239.73	20	30857.86	$a\ ^3F_3 - z\ ^3G_3^\circ$
2923.02	100	34201.2	$a\ ^3D_3 - z\ ^1G_4^\circ$	3239.86	100	30856.63	$b\ ^1D_2 - y\ ^3D_3^\circ$
2924.12	20	34188.3	$a\ ^1D_2 - x\ ^3F_3^\circ$	3247.79	20	30781.29	$a\ ^3P_0 - y\ ^3D_1^\circ$
2935.80	5	34052.3	$b\ ^1D_2 - x\ ^1F_3^\circ$	3249.48	10	30765.28	$a\ ^3P_1 - x\ ^3P_0^\circ$
2944.42	5	33952.6	$a\ ^3P_2 - x\ ^1P_1^\circ$	3253.84	30 *cl*	30724.06	$z\ ^3P_0^\circ - e\ ^3S_1$
2966.45	5*h*	33700.5	$y\ ^3F_3^\circ - e\ ^1D_2$	3259.49	30	30670.80	$a\ ^3F_4 - z\ ^3G_4^\circ$
2972.49	10*c*	33632.0	$a\ ^3D_1 - y\ ^3P_2^\circ$	3260.91	1000	30657.45	$a\ ^3D_1 - z\ ^1D_2^\circ$
2994.17	400	33388.5	$a\ ^1S_0 - z\ ^1P_1^\circ$	3281.65	40	30463.70	$a\ ^3P_1 - y\ ^3D_2^\circ$
2996.68	10*hl*	33360.5	$z\ ^3F_2^\circ - e\ ^3D_2$	3301.93	4	30276.60	$z\ ^3D_2^\circ - e\ ^1D_2$
3001.88	40	33302.8	$a\ ^3F_4 - y\ ^3D_3^\circ$	3318.01	300	30129.88	$a\ ^3D_2 - z\ ^1D_2^\circ$
3019.87	300*c*	33104.4	$a\ ^3D_2 - y\ ^3P_2^\circ$	3322.29	40	30091.06	$a\ ^3F_3 - x\ ^3F_4^\circ$
3030.46	7*hl*	32988.7	$y\ ^3F_3^\circ - e\ ^3F_4$	3328.01	30	30039.35	$a\ ^3F_2 - x\ ^3F_3^\circ$
3043.30	1000	32849.5	$a\ ^1D_2 - y\ ^1F_3^\circ$	3331.50	20	30007.88	$y\ ^3F_3^\circ - e\ ^1G_4$
3064.25	40*hl*	32624.9	$z\ ^3F_2^\circ - e\ ^3F_3$	3343.04	10 *h*	29904.29	$y\ ^3F_4^\circ - e\ ^3F_4$
3069.36	400	32570.6	$a\ ^3F_2 - z\ ^3G_3^\circ$	3359.68	6	29756.19	$a\ ^3F_3 - y\ ^1D_2^\circ$
3076.17	10	32498.5	$a\ ^3P_0 - x\ ^3P_1^\circ$	3383.53	400	29546.45	$a\ ^3D_3 - z\ ^3D_3^\circ$
3076.87	40	32491.1	$a\ ^1D_2 - x\ ^3F_2^\circ$	3388.51	6	29503.02	$a\ ^3P_1 - y\ ^3D_1^\circ$
3078.07	300	32478.5	$a\ ^3F_3 - z\ ^3G_4^\circ$	3388.85	10 *c*	29500.07	$z\ ^3P_1^\circ - e\ ^3S_1$
3080.54	10*h*	32452.4	$z\ ^3P_1^\circ - e\ ^3F_2$	3402.11	5 *hl*	29385.09	$y\ ^3F_4^\circ - e\ ^1F_3$
3084.85	20	32407.1	$a\ ^1G_4 - x\ ^1F_3^\circ$	3413.84	400	29284.13	$a\ ^1D_2 - y\ ^3P_2^\circ$
3086.04	300	32394.6	$a\ ^3F_4 - z\ ^3G_5^\circ$	3417.77	600	29250.45	$a\ ^1S_0 - z\ ^3D_1^\circ$
3087.37	200	32380.6	$a\ ^3D_3 - z\ ^3H_4^\circ$	3440.40	20	29058.06	$a\ ^3P_2 - x\ ^3P_2^\circ$
3100.63	20	32242.2	$a\ ^3P_1 - x\ ^3P_2^\circ$	3481.16	1000	28717.83	$a\ ^3D_3 - z\ ^1F_3^\circ$

TABLE 5. *Classified lines of* Ac II—Continued

Wavelength	Intensity	Wave number	Term combination	Wavelength	Intensity	Wave number	Term combination
A		*K*		*A*		*K*	
3481.56	10	28714.54	$z\,^3F_3^\circ - e\,^1G_4$	4088.44	3000*cs*	24452.30	$a\,^3D_3 - z\,^3P_2^\circ$
3483.25	20	28700.61	$a\,^3F_2 - y\,^1F_3^\circ$	4113.86	10	24301.21	$a\,^1D_2 - z\,^1P_1^\circ$
3489.53	400	28648.95	$a\,^3D_1 - y\,^1P_1^\circ$	4132.42	20	24192.07	$a\,^1G_4 - x\,^3F_4^\circ$
3491.47	3 *h*	28633.04	$z\,^3F_3^\circ - e\,^3D_2$	4136.22	5	24169.85	$a\,^3F_3 - z\,^3F_4^\circ$
3499.75	20	28565.30	$a\,^3D_1 - z\,^3D_2^\circ$	4137.99	40*hl*	24159.51	$a\,^3F_4 - z\,^3H_5^\circ$
3527.31	200	28342.11	$a\,^3F_2 - x\,^3F_2^\circ$	4144.15	10	24123.60	$z\,^3D_1^\circ - e\,^1S_0$
3529.24	200	28326.62	$a\,^3F_3 - x\,^3F_3^\circ$	4152.88	1*h*	24072.89	$b\,^1D_2 - x\,^3F_3^\circ$
3532.14	15	28303.36	$a\,^1G_4 - z\,^3G_5^\circ$	4168.40	2000*cs*	23983.26	$a\,^3D_2 - z\,^3D_1^\circ$
3534.63	250	28283.42	$a\,^3F_4 - x\,^3F_4^\circ$	4169.12	2	23979.12	$y\,^3P_2^\circ - e\,^1F_3$
3545.44	10	28197.18	$z\,^3F_2^\circ - e\,^3G_3$	4209.69	300	23748.03	$a\,^3D_3 - z\,^3F_3^\circ$
3546.83	15	28186.14	$z\,^3F_2^\circ - e\,^3F_2$	4232.67	20	23619.10	$a\,^3F_2 - y\,^3P_1^\circ$
3547.07	2*h*	28184.23	$z\,^3P_2^\circ - e\,^3D_1$	4257.82	50*hl*	23479.59	$y\,^3F_3^\circ - e\,^3S_1$
3554.99	400	28121.44	$a\,^3D_2 - z\,^1P_1^\circ$	4259.65	20	23469.50	$z\,^3F_3^\circ - e\,^3G_3$
3562.33	30	28063.50	$y\,^3F_2^\circ - e\,^3D_3$	4261.10	20*cl*	23461.51	$a\,^3D_1 - y\,^3F_2^\circ$
3565.59	2000	28037.84	$a\,^3D_2 - z\,^3D_2^\circ$	4261.67	10	23458.38	$z\,^3F_3^\circ - e\,^3F_2$
3579.53	15*hl*	27928.66	$z\,^3P_2^\circ - e\,^3D_2$	4268.21	40	23422.40	$a\,^3F_3 - y\,^3P_2^\circ$
3583.55	30*hl*	27897.33	$z\,^3F_3^\circ - e\,^3F_4$	4337.13	30	23050.24	$a\,^3F_4 - z\,^3H_4^\circ$
3585.09	40	27885.34	$a\,^1D_2 - z\,^3D_3^\circ$	4359.13	400	22933.91	$a\,^3D_2 - y\,^3F_2^\circ$
3588.31	5	27860.32	$a\,^3P_2 - y\,^3D_3^\circ$	4364.08	3	22907.89	$a\,^3F_2 - z\,^1F_3^\circ$
3595.75	20	27802.68	$y\,^3F_3^\circ - e\,^3G_4$	4386.41	1500	22791.28	$a\,^1D_2 - z\,^3P_2^\circ$
3600.24	4	27768.00	$a\,^1D_2 - y\,^3P_1^\circ$	4391.43	6	22765.23	$z\,^3P_2^\circ - e\,^3G_3$
3643.62	8*hl*	27437.41	$z\,^1F_3^\circ - e\,^1D_2$	4397.45	5	22734.06	$b\,^1D_2 - y\,^1F_3^\circ$
3664.69	10	27279.67	$a\,^3P_2 - y\,^3D_2^\circ$	4442.05	20	22505.81	$a\,^3P_2 - y\,^1D_2^\circ$
3683.66	30	27139.19	$a\,^3D_1 - z\,^3P_2^\circ$	4452.19	700	22454.55	$a\,^3D_3 - y\,^3F_4^\circ$
3694.88	150	27056.78	$a\,^1D_2 - z\,^1F_3^\circ$	4467.90	10	22375.60	$b\,^1D_2 - x\,^3F_2^\circ$
3704.32	9	26987.83	$a\,^3F_3 - y\,^1F_3^\circ$	4470.59	50	22362.14	$a\,^3F_4 - z\,^3F_3^\circ$
3709.03	3	26953.56	$z\,^1D_2^\circ - e\,^1F_3$	4507.20	2000*cl*	22180.50	$a\,^1S_0 - z\,^3P_1^\circ$
3713.17	6*h*	26923.51	$y\,^3F_4^\circ - e\,^1G_4$	4511.23	15	22160.69	$a\,^3F_2 - z\,^1D_2^\circ$
3734.47	5*h*	26769.95	$z\,^3F_3^\circ - e\,^3D_3$	4526.27	15*c*	22087.05	$a\,^1D_2 - z\,^3F_3^\circ$
3740.67	2	26725.58	$z\,^1F_3^\circ - e\,^3F_4$	4539.29	3	22023.70	$a\,^3F_3 - z\,^3D_3^\circ$
3747.25	5	26678.65	$a\,^3F_3 - z\,^1G_4^\circ$	4544.09	100	22000.44	$a\,^3P_2 - y\,^1P_1^\circ$
3754.18	15	26629.41	$a\,^3F_3 - x\,^3F_2^\circ$	4585.83	3*h*	21800.19	$z\,^1F_3^\circ - e\,^3D_3$
3756.67	500*c*	26611.76	$a\,^3D_2 - z\,^3P_2^\circ$	4605.45	1000	21707.32	$a\,^3D_1 - z\,^3F_2^\circ$
3761.24	20	26579.42	$a\,^1G_4 - z\,^3G_4^\circ$	4684.91	6*h*	21339.15	$z\,^3D_2^\circ - e\,^3G_3$
3769.82	20	26518.93	$a\,^3F_4 - x\,^3F_4^\circ$	4716.74	20	21195.15	$a\,^3F_3 - z\,^1F_3^\circ$
3771.21	2*h*	26509.16	$z\,^3F_3^\circ - e\,^3G_4$	4720.16	1000	21179.80	$a\,^3D_2 - z\,^3F_2^\circ$
3772.14	7*h*	26502.59	$z\,^3D_2^\circ - e\,^3D_2$	4740.51	200	21088.88	$a\,^1G_4 - y\,^1F_3^\circ$
3777.80	3	26462.92	$a\,^3P_0 - y\,^1P_1^\circ$	4807.83	100	20793.59	$a\,^1D_2 - y\,^3F_3^\circ$
3799.82	200	26309.57	$a\,^1D_2 - z\,^1D_2^\circ$	4811.06	15	20779.63	$a\,^1G_4 - z\,^1G_4^\circ$
3805.05	40*hl*	26273.40	$z\,^3F_4^\circ - e\,^3G_5$	4812.22	600	20774.62	$a\,^3D_3 - y\,^3F_2^\circ$
3814.78	5*hl*	26206.39	$z\,^1F_3^\circ - e\,^1F_3$	4889.10	80	20447.93	$a\,^3F_3 - z\,^1D_2^\circ$
3858.80	2	25907.45	$a\,^3D_2 - z\,^3F_3^\circ$	4945.18	200	20216.07	$a\,^3F_4 - z\,^3D_3^\circ$
3863.12	2000*c*	25878.48	$a\,^3D_3 - z\,^3D_2^\circ$	4958.23	200	20162.86	$a\,^1D_2 - z\,^3D_1^\circ$
3879.82	2*h*	25767.09	$z\,^3D_3^\circ - e\,^3F_3$	4960.87	150	20152.13	$a\,^3F_2 - z\,^1P_1^\circ$
3907.38	4*h*	25585.35	$z\,^3H_4^\circ - e\,^3G_5$	4981.55	20	20068.47	$a\,^3F_2 - z\,^3D_2^\circ$ $a\,^1G_4 - z\,^3H_5^\circ$
3914.47	200	25539.01	$a\,^3D_1 - y\,^3F_2^\circ$	5065.07	7	19737.56	$a\,^3P_2 - y\,^1F_3^\circ$
3920.10	50	25502.33	$b\,^1D_2 - y\,^1D_2^\circ$	5156.53	60	19387.48	$a\,^3F_4 - z\,^1F_3^\circ$
3938.58	10*h*	25382.68	$z\,^3D_1^\circ - e\,^3F_2$	5164.83	6	19356.33	$a\,^3P_1 - y\,^3P_2^\circ$
3977.36	100	25135.19	$a\,^3F_2 - y\,^3P_2^\circ$	5215.40	30	19168.65	$b\,^1D_2 - y\,^3P_2^\circ$
3999.36	50*hl*	24996.93	$b\,^1D_2 - y\,^1P_1^\circ$	5229.10	10	19118.43	$a\,^3P_0 - y\,^3P_1^\circ$
4002.23	10*hl*	24979.01	$y\,^3F_4^\circ - e\,^3D_3$	5230.43	60*cl*	19113.57	$a\,^1D_2 - y\,^3F_2^\circ$
4005.47	10	24958.80	$a\,^1G_4 - z\,^3G_5^\circ$	5256.03	7*c*	19020.47	$a\,^3D_3 - z\,^3F_2^\circ$
4019.64	80	24870.82	$a\,^3F_4 - z\,^1G_4^\circ$	5273.13	2	18958.79	$a\,^1G_4 - z\,^3H_4^\circ$
4037.15	4*h*	24762.95	$y\,^3F_3^\circ - e\,^3G_3$	5362.61	60	18642.45	$a\,^3F_2 - z\,^3P_2^\circ$
4038.93	2*h*	24752.04	$y\,^3F_3^\circ - e\,^3F_2$	5446.38	400	18355.72	$a\,^3F_3 - z\,^3D_2^\circ$
4044.45	30*hl*	24718.26	$y\,^3F_4^\circ - e\,^3G_4$	5471.71	5	18270.75	$a\,^1G_4 - z\,^3F_4^\circ$
4053.06	25*hl*	24665.75	$z\,^1D_2^\circ - e\,^3D_1$	5548.98	9*c*	18016.33	$a\,^3F_3 - y\,^3F_4^\circ$
4057.36	4*h*	24639.61	$z\,^3D_2^\circ - e\,^3D_3$	5573.16	3*h*	17938.16	$a\,^3F_2 - z\,^3F_3^\circ$
4061.60	500*c*	24613.89	$a\,^3D_2 - y\,^3F_3^\circ$	5603.77	25	17840.18	$a\,^3P_1 - y\,^3P_1^\circ$
4078.70	200	24510.70	$a\,^3D_1 - z\,^3D_1^\circ$	5625.92	3	17769.94	$b\,^1D_2 - z\,^3D_3^\circ$

TABLE 5. *Classified lines of* Ac II—Continued

Wavelength	Intensity	Wave number	Term combination
A		*K*	
5627.57	20	17764.73	$a\ ^3P_1 - y^3P$
5660.93	4*h*	17660.04	$z\ ^3D_3^\circ - e\ ^3F_2$
5663.34	20	17652.53	$b\ ^1D_2 - y\ ^3P_1^\circ$
5732.05	200*cl*	17440.93	$a\ ^3D_1 - z\ ^3P_1^\circ$
5758.97	400*c*	17359.41	$a\ ^1D_2 - z\ ^3F_2^\circ$
5901.10	3	16941.30	$b\ ^1D_2 - z\ ^1F_3^\circ$
5905.14	40	16929.71	$a\ ^3F_3 - z\ ^3P_2^\circ$
5910.85	1000*c*	16913.35	$a\ ^3D_2 - z\ ^3P_1^\circ$
6006.27	9	16644.66	$a\ ^3F_2 - y\ ^3F_3^\circ$
6161.48	2	16225.39	$a\ ^3F_3 - z\ ^3F_4^\circ$
6164.75	600*c*	16216.77	$a\ ^3D_1 - z\ ^3P_0^\circ$
6167.83	100*cl*	16208.67	$a\ ^3F_4 - y\ ^3F_4^\circ$
6173.35	4	16194.18	$b\ ^1D_2 - z\ ^3D_1^\circ$
6181.74	40	16172.20	$a\ ^3P_2 - y\ ^3P_2^\circ$
6242.83	300*c*	16013.94	$a\ ^3F_2 - z\ ^3D_1^\circ$
6387.39	2	15651.52	$a\ ^3P_0 - z\ ^1P_1^\circ$
6535.81	15	15296.10	$a\ ^1G_4 - z\ ^1F_3^\circ$
6695.23	200	14931.88	$a\ ^3F_3 - y\ ^3F_3^\circ$
6933.99	15*c*	14417.73	$a\ ^3F_4 - z\ ^3F_3^\circ$
6996.09	2	14289.76	$a\ ^3P_1 - z\ ^3D_2^\circ$
7567.65	4	13210.50	$a\ ^3F_2 - z\ ^3F_2^\circ$
7617.42	2	13124.19	$a\ ^3F_4 - y\ ^3F_3^\circ$
7886.82	3	12675.89	$b\ ^1D_2 - z\ ^3P_2^\circ$

5. Spectrum of Neutral Actinium (Ac I)

Lacking Zeeman data that identify atomic-energy levels, the only way to find such levels in the Ac I spectrum was to search wave numbers for constant differences. Such a search among selected strong lines promptly revealed a difference of 2231.43 K, which was interpreted as the interval between ^2D levels arising from ds^2, and representing the ground term. This is in perfect agreement with the homologous spectra, Sc I, Y I, and La I, all of which have $(ds^2)\,^2D$ as ground term.

In each case, the next lowest energy belongs to a quartet-F term arising from d^2s, and the analogous ^4F term in Ac I was located between 9217 and 12078, much higher than in La I, but approximately in the same position as in Y I. The same d^2s configuration also produces higher even terms, viz, ^4P, ^2S, ^2P, ^2D, ^2F, ^2G, but these are too high to be detected in Ac I without more red or infrared data. This analysis of Ac I was extended by using Y I as a guide. The lowest odd term in Y I is $(s^2p)\,^2P^\circ$, which is even lower than $(d^2s)\,^4F$. A similar case was found in Lu I, and Klinkenberg [16] was able to evaluate this $^2P^\circ$ term with the help of two infrared lines. Lacking infrared data for Ac I this $^2P^\circ$ term cannot be established, but many of the other odd terms arising from dsp and one from d^2p could be identified by comparison with Y I. The known energy levels derived from this analysis of the Ac I spectrum are presented in table 6 with electron configurations (and limits), term designations, J-values, energy levels, and intervals in successive columns. No evidence for terms arising from configurations including a $5f$ electron, nor for high even (third set) terms could be found in the available list of Ac I lines. Such terms were found in La I [6] because that spectrum was fully observed from 2600 to 11000 A, whereas the observations of Ac I are confined to about half that range. Because the first ionization potential of Ac is not obtainable from spectral series at this time, we must accept the value 6.89 $\pm$0.6 v derived by Finkelnburg and Humbach [15] by their method of triple extrapolation.

TABLE 6. *Terms in the* Ac I *spectrum*

Configuration	Designation	J	Level	Interval
$6d\ 7s^2$	$a\ ^2D$	$1\frac{1}{2}$	0.00	2231.43
		$2\frac{1}{2}$	2231.43	
$6d^2\ 7s$	$a\ ^4F$	$1\frac{1}{2}$	9217.28	646.31
		$2\frac{1}{2}$	9863.59	1042.43
		$3\frac{1}{2}$	10906.02	1172.05
		$4\frac{1}{2}$	12078.07	
$7s^2(a\ ^1S)7p$	$z\ ^2P^\circ$	$0\frac{1}{2}$	?	
		$1\frac{1}{2}$	?	
$6d\ 7s(a\ ^3D)7p$	$z\ ^4F^\circ$	$1\frac{1}{2}$	*13712.90*	1227.82
		$2\frac{1}{2}$	*14940.72*	2743.15
		$3\frac{1}{2}$	*17683.87*	
		$4\frac{1}{2}$	?	
$6d\ 7s(a\ ^3D)7p$	$z\ ^2D^\circ$	$1\frac{1}{2}$	*17736.26*	214.45
		$2\frac{1}{2}$	*17950.71*	
$6d\ 7s(a\ ^3D)7p$	$z\ ^4D^\circ$	$0\frac{1}{2}$	*17199.71*	1812.75
		$1\frac{1}{2}$	*19012.46*	2183.41
		$2\frac{1}{2}$	*21195.87*	2280.07
		$3\frac{1}{2}$	*23475.94*	
$6d\ 7s(a\ ^3D)7p$	$z\ ^4P^\circ$	$0\frac{1}{2}$	*22401.52*	399.58
		$1\frac{1}{2}$	*22801.10*	1097.76
		$2\frac{1}{2}$	*23898.86*	
$6d\ 7s(a\ ^3D)7p$	$z\ ^2F^\circ$	$2\frac{1}{2}$	*23916.84*	1052.46
		$3\frac{1}{2}$	*24969.30*	
$6d\ 7s(a\ ^1D)7p$	$y\ ^2D^\circ$	$1\frac{1}{2}$	*26066.04*	467.12
		$2\frac{1}{2}$	*26533.16*	
$6d\ 7s(a\ ^3D)7p$	$y\ ^2P^\circ$	$0\frac{1}{2}$	*25729.03*	1280.81
		$1\frac{1}{2}$	*27009.84*	
$6d\ 7s(a\ ^1D)7p$	$y\ ^2F^\circ$	$2\frac{1}{2}$	*26836.20*	1732.20
		$3\frac{1}{2}$	*28568.40*	
$6d\ 7s(a\ ^1D)7p$	$x\ ^2P^\circ$	$0\frac{1}{2}$	?	
		$1\frac{1}{2}$	*30396.61*	
$6d^2(a\ ^3F)7p$	$z\ ^4G^\circ$	$2\frac{1}{2}$	*31494.68*	724.94
		$3\frac{1}{2}$	*32219.62*	647.77
		$4\frac{1}{2}$	*32867.39*	561.37
		$5\frac{1}{2}$	*33429.76*	
$6d^2(a\ ^3F)7p$		$1\frac{1}{2}$	*31800.35*	
		$2\frac{1}{2}$	*32495.67*	
		$1\frac{1}{2}$	*32918.40*	
		$1\frac{1}{2}$	*33673.66*	
		$3\frac{1}{2}$	*33756.43*	
		$3\frac{1}{2}$	*34360.25*	
		$2\frac{1}{2}$	*34658.47*	
		$4\frac{1}{2}$	*34788.12*	
		$4\frac{1}{2}$	*35870.00*	

The strength of Ac II lines in the hollow cathode, and especially in the arc, indicates that actinium has a relatively low ionization potential (probably between 6 and 7 v), and accounts for the reduced intensity of Ac I in the sources. Barely 140 Ac I lines were observed between 2968 and 6691 A, and only two with greater wavelength (7290 and 7866 A).

If another sample of actinium becomes available it will be possible to extend the observation of Ac I with an electrodeless quartz lamp containing metal-halide [17] because it is now known that such lamps, when excited by ultrahigh frequency, strongly favor the emission of the first spectra. It was possible to classify 85 Ac I lines as shown in table 7. Although table 7 contains only 62 percent of the total number of Ac I lines, it includes 88 percent of the total observed intensity.

TABLE 7. *Classified lines of* Ac I

Wavelength	Intensity	Wave number	Term combination	Wavelength	Intensity	Wave number	Term combination
A		*K*		*A*		*K*	
2968. 82	5	33673. 6	$a\ ^2D_{1½}-336^{\circ}_{1½}$	4396. 71	400	22737. 89	$a\ ^2D_{2½}-z\ ^2F^{\circ}_{3½}$
3036. 93	10	32918. 4	$a\ ^2D_{1½}-329^{\circ}_{1½}$	4402. 11	100	22710. 00	$a\ ^4F_{4½}-347^{\circ}_{4½}$
3076. 44	30	32495. 66	$a\ ^2D_{1½}-324^{\circ}_{1½}$				
3082. 96	2	32427. 0	$a\ ^2D_{2½}-346^{\circ}_{2½}$	4417. 26	30	22632. 12	$a\ ^4F_{2½}-324^{\circ}_{1½}$
3111. 57	50	32128. 80	$a\ ^2D_{2½}-343^{\circ}_{3½}$	4426. 85	15	22583. 08	$a\ ^4F_{1½}-318^{\circ}_{1½}$
				4462. 73	400	22401. 52	$a\ ^2D_{1½}-z\ ^4P^{\circ}_{2½}$
3143. 71	100	31800. 34	$a\ ^2D_{1½}-318^{\circ}_{1½}$	4471. 81	80	22356. 03	$a\ ^4F_{2½}-z\ ^4G^{\circ}_{3½}$
3171. 17	150	31524. 98	$a\ ^2D_{2½}-337^{\circ}_{3½}$	4486. 63	20	22282. 19	$a\ ^4F_{4½}-343^{\circ}_{3½}$
3174. 23	20	31494. 65	$a\ ^2D_{1½}-z\ ^4G^{\circ}_{2½}$				
3179. 52	3	31442. 19	$a\ ^2D_{2½}-336^{\circ}_{1½}$	4487. 60	40	22277. 38	$a\ ^4F_{1½}-z\ ^4G^{\circ}_{2½}$
3257. 77	4	30687. 00	$a\ ^2D_{2½}-329^{\circ}_{1½}$	4552. 18	100	21961. 34	$a\ ^4F_{3½}-z\ ^4G^{\circ}_{4½}$
				4557. 28	15	21936. 76	$a\ ^4F_{2½}-318^{\circ}_{1½}$
3288. 90	15	30396. 55	$a\ ^2D_{1½}-x\ ^2P^{\circ}_{1½}$	4610. 10	100	21685. 43	$a\ ^2D_{2½}-z\ ^2F^{\circ}_{2½}$
3303. 28	20	30264. 22	$a\ ^2D_{2½}-324^{\circ}_{1½}$	4611. 59	4	21678. 42	$a\ ^4F_{4½}-337^{\circ}_{3½}$
3380. 96	10	29568. 91	$a\ ^2D_{2½}-318^{\circ}_{1½}$				
3416. 29	15	29263. 29	$a\ ^2D_{2½}-z\ ^4G^{\circ}_{3½}$	4613. 93	300	21667. 43	$a\ ^2D_{2½}-z\ ^4P^{\circ}_{2½}$
3549. 47	5	28165. 17	$a\ ^2D_{2½}-x\ ^2P^{\circ}_{1½}$	4621. 69	60	21631. 05	$a\ ^4F_{2½}-z\ ^4G^{\circ}_{2½}$
				4682. 16	100	21351. 69	$a\ ^4F_{4½}-z\ ^4G^{\circ}_{5½}$
3701. 30	80	27009. 85	$a\ ^2D_{1½}-y\ ^2P^{\circ}_{1½}$	4690. 52	60	21313. 63	$a\ ^4F_{3½}-z\ ^4G^{\circ}_{3½}$
3725. 22	4	26836. 22	$a\ ^2D_{1½}-y\ ^2F^{\circ}_{2½}$	4705. 78	200	21244. 51	$a\ ^2D_{2½}-z\ ^4D^{\circ}_{3½}$
3767. 80	30	26533. 15	$a\ ^2D_{1½}-y\ ^2D^{\circ}_{2½}$				
3795. 86	10	26337. 01	$a\ ^2D_{2½}-y\ ^2F^{\circ}_{3½}$	4716. 58	500	21195. 87	$a\ ^2D_{1½}-z\ ^4D^{\circ}_{2½}$
3835. 32	100	26066. 05	$a\ ^2D_{1½}-y\ ^2D^{\circ}_{1½}$	4808. 81	10	20789. 35	$a\ ^4F_{4½}-z\ ^4G^{\circ}_{4½}$
				4855. 68	50	20588. 68	$a\ ^4F_{3½}-z\ ^4G^{\circ}_{2½}$
3885. 56	400	25729. 03	$a\ ^2D_{1½}-y\ ^2P^{\circ}_{2½}$	4860. 16	150	20569. 71	$a\ ^2D_{2½}-z\ ^4P^{\circ}_{1½}$
3929. 52	5	25441. 20	$a\ ^4F_{1½}-346^{\circ}_{2½}$	4868. 87	20	20532. 91	$a\ ^4F_{2½}-x\ ^2P^{\circ}_{1½}$
4004. 64	20	24963. 98	$a\ ^4F_{3½}-346^{\circ}_{2½}$				
4031. 95	40	24794. 90	$a\ ^4F_{2½}-346^{\circ}_{2½}$	4963. 48	10	20141. 53	$a\ ^4F_{4½}-z\ ^4G^{\circ}_{3½}$
4034. 63	200	24778. 42	$a\ ^2D_{2½}-y\ ^2P^{\circ}_{1½}$	5258. 24	300	19012. 48	$a\ ^2D_{1½}-z\ ^4D^{\circ}_{1½}$
				5271. 56	150	18964. 44	$a\ ^2D_{2½}-z\ ^4D^{\circ}_{2½}$
4063. 10	200	24604. 80	$a\ ^2D_{2½}-y\ ^2F^{\circ}_{2½}$	5344. 74	100	18704. 78	$a\ ^4F_{2½}-y\ ^2F^{\circ}_{3½}$
4081. 04	5	24496. 64	$a\ ^4F_{2½}-343^{\circ}_{3½}$	5569. 26	200	17950. 72	$a\ ^2D_{1½}-z\ ^2D^{\circ}_{2½}$
4087. 76	20	24456. 38	$a\ ^4F_{1½}-336^{\circ}_{1½}$				
4113. 77	80	24301. 75	$a\ ^2D_{2½}-y\ ^2D^{\circ}_{2½}$	5618. 77	40	17792. 55	$a\ ^4F_{1½}-y\ ^2P^{\circ}_{1½}$
4179. 98	1000	23916. 82	$a\ ^2D_{1½}-z\ ^2F^{\circ}_{2½}$	5636. 60	100	17736. 27	$a\ ^2D_{1½}-z\ ^2D^{\circ}_{1½}$
				5660. 19	40	17662. 35	$a\ ^4F_{3½}-y\ ^2F^{\circ}_{3½}$
4183. 12	500	23898. 87	$a\ ^2D_{1½}-z\ ^4P^{\circ}_{2½}$	5674. 15	80	17618. 90	$a\ ^4F_{1½}-y\ ^2F^{\circ}_{2½}$
4184. 17	6	23892. 87	$a\ ^4F_{2½}-337^{\circ}_{3½}$	5812. 44	30	17199. 71	$a\ ^2D_{1½}-z\ ^4D^{\circ}_{0½}$
4186. 05	15	23882. 14	$a\ ^4F_{3½}-347^{\circ}_{4½}$				
4194. 40	400	23834. 60	$a\ ^2D_{2½}-y\ ^2D^{\circ}_{1½}$	5830. 55	10	17146. 29	$a\ ^4F_{2½}-y\ ^2P^{\circ}_{1½}$
4198. 72	30	23810. 07	$a\ ^4F_{2½}-336^{\circ}_{1½}$	5957. 47	10	16781. 00	$a\ ^2D_{2½}-z\ ^4D^{\circ}_{1½}$
				6170. 18	5	16202. 50	$a\ ^4F_{2½}-y\ ^2D^{\circ}_{1½}$
4201. 92	30	23791. 94	$a\ ^4F_{4½}-358^{\circ}_{4½}$	6275. 67	10	15930. 15	$a\ ^4F_{3½}-y\ ^2F^{\circ}_{2½}$
4208. 91	50	23752. 43	$a\ ^4F_{3½}-346^{\circ}_{2½}$	6359. 86	300	15719. 27	$a\ ^2D_{2½}-z\ ^2D^{\circ}_{2½}$
4218. 02	50	23701. 13	$a\ ^4F_{1½}-329^{\circ}_{1½}$				
4262. 42	40	23454. 25	$a\ ^4F_{3½}-343^{\circ}_{3½}$	6447. 82	40	15504. 83	$a\ ^2D_{2½}-z\ ^2D^{\circ}_{1½}$
4294. 62	10	23278. 40	$a\ ^4F_{1½}-324^{\circ}_{1½}$	6469. 68	50	15452. 44	$a\ ^2D_{2½}-z\ ^4F^{\circ}_{3½}$
				6618. 19	10	15105. 70	$a\ ^4F_{2½}-z\ ^2F^{\circ}_{3½}$
4336. 27	20	23054. 81	$a\ ^4F_{2½}-329^{\circ}_{1½}$	6691. 27	200	14940. 72	$a\ ^2D_{1½}-z\ ^4F^{\circ}_{2½}$
4375. 07	20	22850. 36	$a\ ^4F_{3½}-337^{\circ}_{3½}$	7290. 40	300	13712. 90	$a\ ^2D_{1½}-z\ ^4F^{\circ}_{1½}$
4384. 53	300	22801. 06	$a\ ^2D_{1½}-z\ ^4P^{\circ}_{1½}$	7866. 10	200	12709. 28	$a^2\ D_{2½}-z\ ^4F^{\circ}_{2½}$

6. A Comparison of Homologous Spectra of Sc, Y, La, and Ac

Now that the main features of the first three spectra of scandium, yttrium, lanthanum, and actinium are known, a detailed comparison of the homologous spectra may be of interest in connection with atomic structure and electron binding. Such a comparison is facilitated by tables and graphs. Beginning with the one-electron spectra (Sc III, Y III, La III, and Ac III) of doubly-ionized homologous atoms, the terms, levels and intervals are given in table 8, and shown graphically in figure 4. The relative strength of binding of s, p, and d electrons in these four ions is seen to be quite different; the d electron is tightly bound in the first three, but in the fourth the s electron is preferred. In Ac III the $5f$ electron is more firmly bound than $7p$; in La III the $4f$ term is probably even lower but has not been located.

The levels and intervals of 2-electron spectra (Sc II, Y II, La II, and Ac II) are collected in table 9, but the data for high even levels (third set) are omitted for brevity. Figure 5 shows the relative positions of the low (even) levels of four homologous spectra; it makes obvious the remarkable differences in binding of s and d electrons and proves that for these levels the similarity of Ac II and Y II is greater than for any other pair. The stability is greatest for s^2, and decreases progressively for sd, and d^2.

TABLE 8. *Levels and intervals in homologous spectra*

Designation	Sc III		Y III		La III		Ac III	
$3-6d\ ^2D_{1½}$	0. 0	197. 5	0. 0	724. 8	0. 0	1603. 23	801. 0	3402. 9
$^2D_{2½}$	197. 5		724. 8		1603. 23		4203. 9	
$4-7s\ ^2S_{0½}$	25536. 7		7466. 2		13590. 76		0. 0	
$4-5f\ ^2F^{o}_{2½}$					?		*23454. 5*	2625. 7
$^2F^{o}_{3½}$					?		*26080. 2*	
$4-7p\ ^2P^{o}_{0½}$	*62102. 2*	473. 7	*41401. 2*	1553. 5	*42014. 92*	3095. 72	*29465. 9*	8597. 1
$^2P^{o}_{1½}$	*62575. 9*		*42954. 7*		*45110. 64*		*38063. 0*	
$4-7d\ ^2D_{1½}$	112254. 2	45. 0	88378. 8	198. 3	82378. 75	433. 76		?
$^2D_{2½}$	112299. 2		88577. 1		82812. 51			?
$5-8s\ ^2S_{0½}$	114863. 8		86713. 9		82345. 0			?

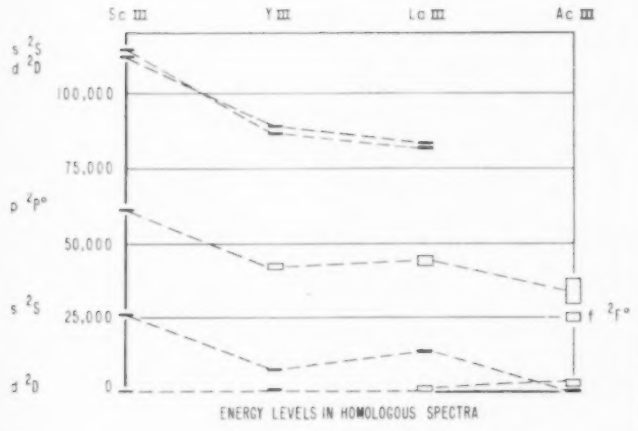

FIGURE 4. *Energy levels derived from the third spectra of scandium, yttrium, lanthanum, and actinium.*

Ordinates in K.

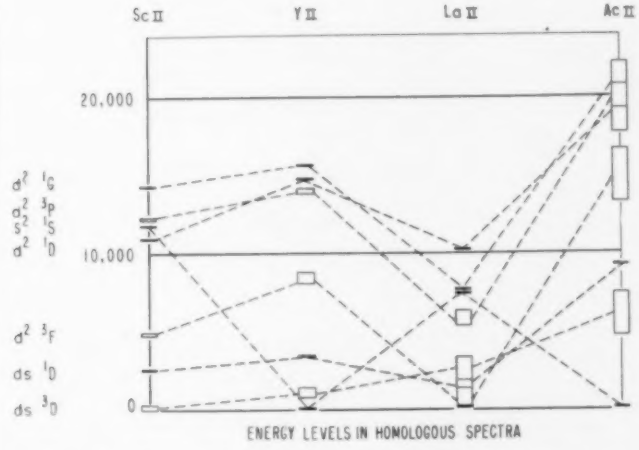

FIGURE 5. *Energy levels derived from the second spectra of scandium, yttrium, lanthanum, and actinium.*

Ordinates in K.

No plot of the odd levels from *sp*, *dp*, *sf*, and *df* is given, but a study of table 9 shows that the 4 levels identified with *sp* in Ac II average about 8000 K smaller than the corresponding levels in La II, whereas 10 levels associated with *dp* average about 7000 K greater than the analogous levels in La II. The most spectacular difference between these spectra appears in the levels assigned to *sf* and *df* configurations; in Ac II the 4 *sf* levels average about 17000 K higher than the analogous levels in La II, and the 18 *df* levels average nearly 26000 K higher. This is perhaps the most interesting result of these investigations of actinium spectra; it proves that the 5*f* electron is loosely bound in actinium compared with the binding of the 4*f* electron in lanthanum. It will be interesting to see how the 5*f* electron is bound in thorium and protactinium. In fact, the 5*f* electron has already been detected in several spectra of thorium; in Th IV it represents the ground state according to Klinkenberg and Lang [18], in Th III configurations containing the 5*f* electron give a level that is only 809.9 K above the ground state [19], in Th II the configurations including the 5*f* electron are 4490.3 K higher than those without [20], and in Th I the configurations with 5*f* electron are still unknown.

The principal levels and intervals of 3-electron spectra (Sc I, Y I, La I, and Ac I) are collected in table 10. Because the data for Ac I are deficient compared with the others, table 10 is abbreviated to include primarily the identified terms of Ac I and show how the close resemblance of Ac I and Y I served as a guide for such identifications.

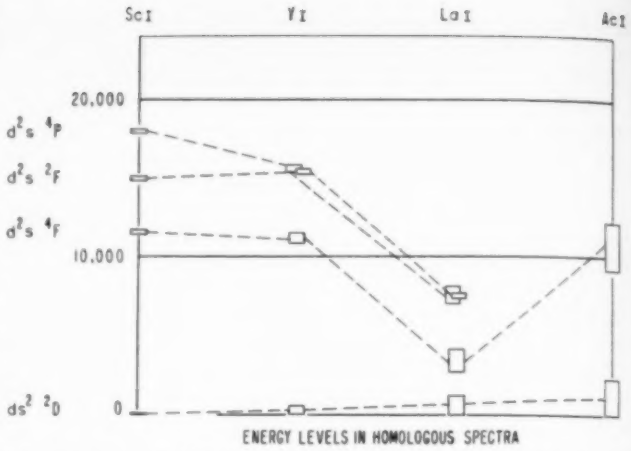

FIGURE 6. *Energy levels derived from the first spectra of scandium, yttrium, lanthanum, and actinium.*

Ordinates in K.

In figure 6 some low even terms in four comparable spectra are plotted; it shows the impossibility of finding the missing $(d^2s)^2F$, ^4P terms in Ac I without infrared data.

TABLE 9. *Levels and intervals in homologous spectra*

Electrons	Terms	Sc II	Interval	Y II	Interval	La II	Interval	Ac II	Interval
s^2	$^1S_0$	11736. 35		0. 00		7394. 57		0. 00	
$d(^2D)s$	$^3D_1$	0. 00		840. 18		1895. 15		4739. 63	
			67. 68		204. 89		696. 45		527. 53
	$^3D_2$	67. 68		1045. 07		2591. 60		5267. 16	
			109. 95		404. 68		658. 75		2159. 36
	$^3D_3$	177. 63		1449. 75		3250. 35		7426. 52	
$d(^2D)s$	$^1D_2$	2540. 97		3296. 20		1394. 46		9087. 54	
d^2	$^3F_2$	4802. 75		8003. 12		0. 00		13236. 46	
			80. 67		324. 91		1016. 10		1712. 75
	$^3F_3$	4883. 42		8328. 03		1016. 10		14949. 21	
			104. 22		415. 30		954. 60		1807. 69
	$^3F_4$	4987. 64		8743. 33		1970. 70		16756. 90	
d^2	$^3P_0$	12074. 00		13883. 44		5249. 70		17737. 10	
			27. 45		134. 86		468. 42		1278. 22
	$^3P_1$	12101. 45		14018. 24		5718. 12		19015. 32	
			52. 89		79. 84		509. 30		3184. 13
	$^3P_2$	12154. 34		14098. 08		6227. 42		22199. 45	
d^2	$^1D_2$	10944. 51		14832. 89		10094. 86		19203. 02	
d^2	$^1G_4$	14261. 40		15682. 91		7473. 32		20848. 23	
$s(^2S)p$	$^3P_0^o$			*23445. 05*		*31785. 82*		*20956. 40*	
					331. 20		375. 17		1224. 12
	$^3P_1^o$			*23776. 25*		*32160. 99*		*22180. 52*	
					870. 89		1043. 42		9698. 35
	$^3P_2^o$			*24647. 14*		*33204. 41*		*31878. 87*	
$d(^2D)p$	$^1D_2^o$	*26081. 32*		*26147. 27*		*24462. 66*		*35397. 12*	

TABLE 9. *Levels and intervals in homologous spectra*—Continued

Electrons	Terms	Sc II	Interval	Y II	Interval	La II	Interval	Ac II	Interval
$d(^2D)\,p$	$^3F_2^3$	*27443. 65*		*27227. 00*		*26414. 01*		*26446. 96*	
			158. 67		305. 34		423. 65		4727. 64
	$^3F_3^3$	*27602. 32*		*27532. 34*		*26837. 66*		*31174. 60*	
			238. 85		861. 83		1727. 74		7944. 42
	$^3F_4^3$	*27841. 17*		*28394. 17*		*28565. 40*		*39119. 02*	
$d(^2D)\,p$	$^1P_1^3$	*30815. 65*		*27516. 70*		*30353. 33*		*44199. 94*	
$d(^2D)\,p$	$^3D_1^3$	*27917. 69*		*28595. 27*		*25973. 37*		*29250. 40*	
			103. 52		134. 75		1414. 74		4054. 56
	$^3D_2^3$	*28021. 21*		*28730. 02*		*27388. 11*		*33304. 96*	
			139. 82		483. 93		927. 14		3667. 98
	$^3D_3^3$	*28161. 03*		*29213. 95*		*28315. 25*		*36972. 94*	
$d(^2D)\,p$	$^3P_0^3$	*29736. 22*		*32048. 76*		*27545. 85*		*36780. 01*	
			5. 90		75. 31		608. 70		75. 49
	$^3P_1^3$	*29742. 12*		*32124. 07*		*28154. 55*		*36855. 50*	
			81. 80		159. 36		1343. 50		1516. 14
	$^3P_2^3$	*29823. 92*		*32283. 43*		*29498. 05*		*38371. 64*	
$d(^2D)\,p$	$^1F_3^3$	*32349. 98*		*33336. 74*		*32201. 05*		*41937. 05*	
$s(^2S)\,p$	$^1P_1^3$	*55715. 52*		*44568. 63*		*45692. 17*		*33388. 61*	
$s(^2S)f$	$^3F_2^3$					*14147. 98*		*28201. 11*	
							227. 19		1679. 98
	$^3F_3^3$					*14375. 17*		*29881. 09*	
							1323. 57		3084. 46
	$^3F_4^3$					*15698. 74*		*32965. 55*	
$s(^2S)f$	$^1F_3^3$					*15773. 77*		*36144. 35*	
$d(^2D)f$	$^1G_4^3$					*16599. 17*		*41627. 79*	
$d(^2D)f$	$^3F_2^3$					*17211. 93*		*41578. 57*	
							1023. 63		1697. 28
	$^3F_3^3$					*18235. 56*		*43275. 85*	
							978. 98		1764. 45
	$^3F_4^3$					*19214. 54*		*45040. 30*	
$d(^2D)f$	$^3H_4^3$					*17825. 62*		*39807. 14*	
							754. 79		1109. 27
	$^3H_5^3$					*18580. 41*		*40916. 41*	
							1169. 21		
	$^3H_6^3$					*19749. 62*		?	
$d(^2D)f$	$^1D_2^3$					*18895. 41*		*44705. 33*	
$d(^2D)f$	$^3G_3^3$					*20402. 82*		*45807. 06*	
							928. 78		1620. 61
	$^3G_4^3$					*21331. 60*		*47427. 67*	
							951. 30		1723. 87
	$^3G_5^3$					*22282. 90*		*49151. 54*	
$d(^2D)f$	$^3D_1^3$					*21441. 73*		*48518. 41*	
							664. 29		960. 64
	$^3D_2^3$					*22106. 02*		*49479. 05*	
							431. 28		580. 65
	$^3D_3^3$					*22537. 30*		*50059. 70*	
$d(^2D)f$	$^3P_0^3$					*22683. 70*		*49780. 60*	
							21. 45		455. 00
	$^3P_1^3$					*22705. 15*		*50235. 60*	
							541. 78		1021. 91
	$^3P_2^3$					*23246. 93*		*51257. 51*	
$d(^2D)f$	$^1F_3^3$					*24522. 70*		*53255. 30*	
$d(^2D)f$	$^1P_1^3$					*27423. 91*		*56152. 2*	
$d(^2D)f$	$^1H_5^3$					*28525. 71*		?	

TABLE 10. *Levels and intervals in homologous spectra*

Electrons	Terms	Sc I	Interval	Y I	Interval	La I	Interval	Ac I	Interval
$d\,s^2$	$^2D_{1\frac{1}{2}}$	0. 00	168. 34	0. 00	530. 36	0. 00	1053. 20	0. 00	2231. 43
	$^2D_{2\frac{1}{2}}$	168. 34		530. 36		1053. 20		2231. 43	
$d^2(^3F)s$	$^4F_{1\frac{1}{2}}$	11520. 15	37. 49	10937. 35	141. 26	2668. 20	341. 81	9217. 28	646. 31
	$^4F_{2\frac{1}{2}}$	11557. 64	52. 60	11078. 61	199. 35	3010. 01	484. 57	9863. 59	1042. 43
	$^4F_{3\frac{1}{2}}$	11610. 24	67. 07	11277. 96	254. 17	3494. 58	627. 03	10906. 02	1172. 05
	$^4F_{4\frac{1}{2}}$	11677. 31		11532. 13		4121. 61		12078. 07	
$d^2(^3F)s$	$^2F_{2\frac{1}{2}}$	14926. 24	115. 74	15326. 83	537. 52	7011. 90	1040. 25		
	$^2F_{3\frac{1}{2}}$	15041. 98		15864. 35		8052. 15			
$d^2(^3P)s$	$^4P_{0\frac{1}{2}}$	17918. 85	29. 13	15221. 81	107. 23	7231. 36	259. 10		
	$^4P_{1\frac{1}{2}}$	17947. 98	52. 27	15329. 04	147. 65	7490. 46	189. 48		
	$^4P_{2\frac{1}{2}}$	18000. 25		15476. 69		7679. 94			
$s^2(^1S)\,p$	$^2P^o_{0\frac{1}{2}}$			*10529. 20*	830. 50	*15219. 90*	1060. 30		
	$^2P^o_{1\frac{1}{2}}$			*11359. 70*		*16280. 20*			
$d\,s(^3D)\,p$	$^4F^o_{1\frac{1}{2}}$	*15672. 55*	83. 96	*14949. 00*	296. 80	*13260. 36*	370. 72	*13712. 90*	1227. 82
	$^4F^o_{2\frac{1}{2}}$	*15756. 51*	125. 25	*15245. 80*	466. 60	*13631. 08*	1388. 47	*14940. 72*	2743. 15
	$^4F^o_{3\frac{1}{2}}$	*15881. 76*	144. 76	*15712. 40*	522. 10	*15019. 55*	1223. 70	*17683. 87*	
	$^4F^o_{4\frac{1}{2}}$	*16026. 52*		*16234. 50*		*16243. 25*		?	
$d\,s(^3D)\,p$	$^2D^o_{1\frac{1}{2}}$	*24866. 18*	147. 97	*16146. 10*	−80. 10	*18172. 39*	1207. 05	*17736. 26*	214. 45
	$^2D^o_{2\frac{1}{2}}$	*25014. 15*		*16066. 00*		*19379. 44*		*17950. 71*	
$d\,s(^3D)\,p$	$^4D^o_{0\frac{1}{2}}$	*16009. 71*	12. 07	*16435. 80*	161. 50	*14095. 70*	613. 26	*17199. 71*	1812. 75
	$^4D^o_{1\frac{1}{2}}$	*16021. 78*	119. 26	*16597. 30*	219. 30	*14708. 96*	794. 71	*19012. 46*	2183. 41
	$^4D^o_{2\frac{1}{2}}$	*16141. 04*	69. 76	*16816. 60*	299. 70	*15503. 67*	595. 61	*21195. 87*	2280. 07
	$^4D^o_{3\frac{1}{2}}$	*16210. 80*		*17116. 30*		*16099. 28*		*23475. 94*	
$d\,s(^3D)\,p$	$^4P^o_{0\frac{1}{2}}$	*18504. 05*	11. 72	*18976. 30*	51. 20	*17567. 56*	229. 74	*22401. 52*	399. 58
	$^4P^o_{1\frac{1}{2}}$	*18515. 77*	55. 63	*19027. 50*	120. 50	*17797. 30*	359. 70	*22801. 10*	1097. 76
	$^4P^o_{2\frac{1}{2}}$	*18571. 40*		*19148. 00*		*18157. 00*		*23898. 86*	
$d\,s(^3D)\,p$	$^2F^o_{2\frac{1}{2}}$	*25584. 64*	140. 08	*21528. 60*	386. 80	*16856. 82*	1053. 36	*23916. 84*	1052. 46
	$^2F^o_{3\frac{1}{2}}$	*25724. 72*		*21915. 40*		*17910. 18*		*24969. 30*	
$d\,s(^1D)\,p$	$^2D^o_{1\frac{1}{2}}$	*16096. 86*	−74. 14	*24131. 20*	615. 40	*15031. 65*	−227. 55	*26066. 04*	467. 12
	$^2D^o_{2\frac{1}{2}}$	*16022. 72*		*24746. 60*		*14804. 10*		*26533. 16*	
$d\,s(^3D)\,p$	$^2P^o_{0\frac{1}{2}}$	*24656. 80*	0	*24698. 80*	−218. 20	*25453. 92*	496. 47	*25729. 03*	1280. 81
	$^2P^o_{1\frac{1}{2}}$	*24656. 80*		*24480. 60*		*25950. 39*		*27009. 84*	
$d\,s(^1D)\,p$	$^2F^o_{2\frac{1}{2}}$	*21032. 78*	53. 06	*24518. 80*	80. 70	*15196. 80*	341. 64	*26836. 20*	1732. 20
	$^2F^o_{3\frac{1}{2}}$	*21085. 84*		*24899. 50*		*16538. 44*		*28568. 40*	

TABLE 10. *Levels and intervals in homologous spectra*—Continued

Electrons	Terms	Sc I	Interval	Y I	Interval	La I	Interval	Ac I	Interval
$d\,s(^3D)\,p$	$^2P^o_{0\frac{1}{2}}$	*18711. 03*	144. 73	*27824. 50*	315. 10	*20197. 38*	−178. 38	?	
	$^2P^o_{1\frac{1}{2}}$	*18855. 76*		*28139. 60*		*20019. 00*		*30396. 61*	
$d^2(^3F)\,p$	$^4G^o_{2\frac{1}{2}}$	*29022. 87*	73. 33	*28694. 00*	294. 90	*27022. 60*	432. 74	*31494. 68*	724. 94
	$^4G^o_{3\frac{1}{2}}$	*29096. 20*	93. 63	*28988. 90*	375. 30	*27455. 34*	633. 84	*32219. 62*	647. 77
	$^4G^o_{4\frac{1}{2}}$	*29189. 83*	113. 69	*29364. 20*	456. 20	*28089. 18*	654. 03	*32867. 39*	562. 37
	$^4G^o_{5\frac{1}{2}}$	*29303. 52*		*29820. 40*		*28743. 21*		*33429. 76*	

7. Molecular Spectrum of AcO

The visible spectra of actinium include several sequences of bands that may be attributed to actinium monoxide. These bands are usually double headed, and are always shaded toward longer waves, like those of LaO [21]. The AcO bands were most intense in the arc spectrum of silver and actinium, but the stronger ones were first found in the hollow cathode containing actinium. The observed sequences of AcO bands begin at 4876, 5696, 5718, 5997, 6477, and 6757 A; they probably exist also in the unobserved infrared. Because the observation of AcO spectra is incomplete, and of no special interest in this investigation of atomic spectra of actinium, no attempt has been made to analyze and interpret the AcO spectrum.

It is a pleasure to acknowledge helpful advice from C. E. Moore, G. Racah, and R. E. Trees on questions of interpretation and notation of the Ac II spectrum.

WASHINGTON, October 30, 1956.

8. References

[1] A. Debierne, Compt. rend. **129,** 593–5 (1899).
[2] A. Debierne, Compt. rend. **130,** 906–8 (1900).
[3] W. A. Lub, Compt. rend. **204,** 1417–8 (1937); J. phys. radium **8,** 366–8 (1937); Koninkl. Akad. Wetenschap. Amsterdam **40,** 584–9 (1937).
[4] W. F. Meggers and H. N. Russell, BS Sci. Pap. **22,** 329–73 (1927).
[5] W. F. Meggers and H. N. Russell, BS J. Research **2,** 733–69 (1929) RP55.
[6] H. N. Russell and W. F. Meggers, BS J. Research **9,** 625–68 (1932) RP497.
[7] W. F. Meggers, Science **105,** 514–6 (1947).
[8] M. Fred, F. S. Tomkins, and N. H. Nachtrieb, J. Opt. Soc. Amer. **37,** 279–88 (1947).
[9] H. Schüler and H. Gollnow, Z. Physik **93,** 611–9 (1935).
[10] F. S. Tomkins, M. Fred, and W. F. Meggers, Phys. Rev. **84,** 168 (1951).
[11] M. Fred, F. S. Tomkins, and W. F. Meggers, Phys. Rev. **98,** 1514 (1955).
[12] W. F. Meggers, M. Fred, and F. S. Tomkins, J. Opt. Soc. Amer. **41,** 867–8A (1951).
[13] R. J. Lang, Can. J. Research [A] **14,** 46–7 (1936).
[14] E. Rasmussen, Z. Physik **86,** 24–32 (1933).
[15] W. Finkelnburg and W. Humbach, Naturwiss. **42,** 35–37 (1955).
[16] P. F. A. Klinkenberg, Physica **21,** 53–62 (1954).
[17] C. H. Corliss, W. R. Bozman, and F. O. Westfall, J. Opt. Soc. Amer. **43,** 398–400 (1953).
[18] P. F. A. Klinkenberg and R. J. Lang, Physica **15,** 774–88 (1949).
[19] P. F. A. Klinkenberg, Physica **16,** 618–50 (1950).
[20] T. L. de Bruin, P. F. A. Klinkenberg, and P. Schuurmans, Z. Physik **122,** 23–35 (1955).
[21] W. F. Meggers and J. A. Wheeler, BS J. Research **6,** 239–275 (1931) RP273.

Journal of Research of the National Bureau of Standards Vol. 58, No. 6, June 1957 Research Paper 2764

Thermal Design of Large Storage Vessels for Liquid Hydrogen and Helium [1]

Russell B. Scott

Principles of insulating vessels for the storage and transportation of liquefied gases are discussed. The use of shields cooled by the vapor leaving the liquid being stored is analyzed, and formulas, graphs, and tables are presented for the convenience of the designer of large vessels for storing and transporting liquid hydrogen and liquid helium. An analysis is given of the use of escaping vapor to intercept heat entering by conduction through solid supporting members. The evidence presented indicates that substantial improvements are possible in the design of such vessels.

1. Introduction

The current expansion in large-scale production of liquid hydrogen and helium has increased the importance of efficient storage and transport vessels for these expensive liquids. Published information on the design of low-loss containers includes descriptions [1,2,3,4,5,6] [2] of small laboratory vessels designed for storage of liquid helium. These, of course, are suitable also for storing liquid hydrogen. Some large, rugged, transportable liquid-hydrogen vessels have been constructed but have not yet been described in the open literature. It is the purpose of this paper to discuss some of the general principles relating to the thermal design of low-loss vessels and to present analyses of methods that can be used to improve the performance of an insulated vessel by utilizing the refrigerative effect of the escaping vapor. The material presented will relate specifically to the design of large vessels for liquid hydrogen and helium, although the principles used can be employed in the design of vessels for other liquefied gases.

The invention of the vacuum-insulated vessel for liquefied gases by James Dewar in 1892 was a breakthrough in the field of thermal insulation that has not yet been matched by further developments. All of the advances since Dewar's time have been improvements on Dewar's original concept, usually means of reducing radiant-heat transfer by attaining surfaces of higher reflectivity or by interposing shields that reflect or intercept the radiant energy. The Dewar vessel is illustrated in figure 1. At its best, the vacuum is so good that heat transfer by residual gas is almost negligible. Accordingly, the designer is mainly concerned with reducing the heat transferred by mechanical supports or conveyed across the insulating vacuum by radiation. The heat transferred by the supports is a problem involving the mechanical strength required for a specific application and has no general solution. If there is no restriction on the dimensions of the vessel, the heat conducted through the supports can usually be made quite small simply by using supports of low thermal conductivity and making their lengths great enough. Even in restricted space the clever designer can usually find a way to provide a long thermal path through the solid supports. On the other hand, the heat transferred by radiation is little affected by the thickness of the insulating space. However, this latter mode of heat transfer can be reduced by interposing thermal shields between the warm and cold surfaces of the vessel. The shield is an opaque, highly reflecting surface, geometrically similar to the surface of the liquid container and suspended with the minimum of thermal contact approximately midway between the inner and outer walls of the vacuum space. If the shield has the same reflectivity as that of the boundary walls and contains no openings or irregularities, the radiant-heat transfer will be re-

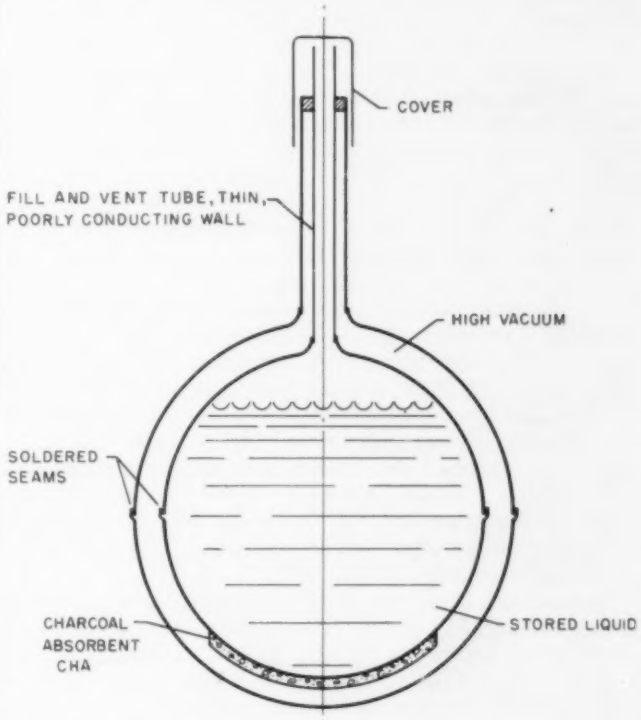

FIGURE 1. *Metal Dewar vessel.*

Commercial vessels of this type usually are mounted in an outer protective shell of sheet steel.

[1] This work was supported by the U. S. Atomic Energy Commission.
[2] Figures in brackets indicate the literature references at the end of this paper.

duced by about one-half. Additional shields will further reduce the heat transferred by radiation. However, the design of mechanical supports, which will hold the shields in place without providing objectionable heat leaks, becomes a formidable task as the number of shields is increased. Also, openings and irregularities that are needed to accommodate the piping and supports for the inner container greatly reduce the effectiveness of this type of multiple shielding.

2. Evacuated-Powder Insulation

Fortunately, a method has been discovered that does not complicate the mechanical design and yet provides a barrier to thermal radiation comparable with multiple shields. This method consists of filling the insulating vacuum space with a fine light powder, such as perlite, sil ca-aerogel, carbon black, or diatomaceous earth. If the thickness of the insulating space is sufficient, filling with powder will greatly reduce the radiant-heat transfer. Moreover, the vacuum requirement is quite modest; the minimum heat transfer is very closely approached when the interstitial gas pressure is reduced to 10 μ of mercury in an insulating powder (e. g., perlite or silica-aerogel) with one boundary at room temperature, 300° K, and the other at the temperature of liquid nitrogen, 77° K. A layer of evacuated powder several centimeters thick will effectively stop radiation and yet not provide an objectionable amount of thermal conduction through the touching particles of powder. When the space between the walls must be small, of the order of 1 cm, the thermal conduction through the powder is objectionable, so in this case the most effective insulation is a high vacuum bounded by highly reflecting walls. Because the principal function of the powder is to stop radiation, it is useful only when radiation constitutes an important heat leak. If an insulating vacuum is bounded by highly reflecting surfaces, such as clean annealed copper, silver, or aluminum, and the surfaces are at 77° and 20° K, respectively, adding powder may actually increase the heat transfer by providing paths of solid conduction. The radiant-heat transfer between the surfaces at these temperatures is so small that its elimination by adding powder is of little consequence. Radiation from a surface at 77° K is only about 0.004 of that from an identical surface at 300° K, because it is proportional to the fourth power of the absolute temperature. Of course the thickness of the insulating space must be considered in such a comparison. It is probably more correct to say that for boundaries at 77° and 20° K a rather large thickness of powder would be required to compete with high-vacuum insulation.

It appears then that evacuated-powder insulation is very desirable if the warm boundary is at ordinary room temperature and the insulating space is thick enough (10 cm or more) so that solid conduction through the powder is not serious.

Of course, evacuated-powder insulation is not new. It has been used for many years in large industrial containers for liquid oxygen and liquid nitrogen. It is particularly suitable for large containers. Now that liquid hydrogen is being stored and transported in large quantities, evacuated powder appears attractive as the insulation to use in large liquid-hydrogen vessels. Evacuated powder has been used in conjunction with a liquid-nitrogen-cooled shield for some vessels holding 750 liters of liquid hydrogen, and there are now under construction some liquid-hydrogen vessels of 6,000-liter capacity that utilize only powder insulation (no refrigerated shield).

3. Dependence of the Rate of Evaporation Upon the Size and Shape of the Vessel

It is quite easy to formulate for liquefied-gas containers some general relationships between the size and shape of the vessel and the rate of evaporation of the liquid it contains. First, because the heat leak into the container increases as the surface area increases, the most favorable shape is the sphere (the greatest ratio of volume to surface). The sphere also has some advantages of mechanical strength but in large sizes it may be expensive to fabricate. The next most favorable common shape is the square cylinder in which the length equals the diameter. The practical approach to this shape is the cylinder with standard commercial dished or elliptical heads. This design has good mechanical strength and is readily fabricated. It is stronger and has a somewhat larger ratio of volume to surface than the cylinder with the flat ends. However, in many cases, particularly vessels that are to be transported by rail or highway, the maximum diameter is fixed.

Thus most of the designs for large insulated tanks for storing and transporting liquefied gases can be assigned to two categories: (1) fixed shape and (2) fixed diameter. It is of interest to see how the performance of such containers varies with the size of the vessel. The effectiveness of a container for liquefied gas is commonly given as the fraction (or percent) of the total contents that evaporates in 1 day.

3.1. Vacuum-Insulated Vessels

For vacuum-insulated containers of fixed shape, that is, containers of geometric similarity but of different sizes, the heat leak by radiation and residual-gas conduction is proportional to the surface area of the inner container, that is, proportional to L^2, where L is a linear dimension of the container. The heat leak through the supports is also proportional to L^2, because the supports will have a length proportional to the linear dimension and a total cross-sectional area proportional to the volume (and weight) of the inner container. Then the total rate of heat leak is

$$W = CL^2 = C_1 V^{(2/3)},$$

where C_1 is a constant and V is the volume of the inner container. The fractional rate of evaporation is

$$\frac{W}{L_v \rho V} = \frac{C_1 V^{(2/3)}}{L_v \rho V} = \frac{C_1}{L_v \rho V^{(1/3)}},$$

where L_v is the heat of vaporization of the liquid and ρ its density.

3.2. Vessels With Porous Insulation

For containers insulated with porous materials, e. g., evacuated powders, the situation is somewhat different because, for similar geometry, the thickness, and therefore the effectiveness of the insulation, is proportional to the linear dimension of the container. The relation between the size and the performance of such vessels is not simple unless the heat conducted by the supports can be neglected. In this case the total heat leak is proportional to the linear dimension, so the fractional evaporation is proportional to $1/V^{(2/3)}$. Thus it is seen that for vessels utilizing this type of insulation, large size is even more advantageous than it is for high-vacuum-insulated vessels.

3.3. Vessels of Fixed Diameter and Different Lengths

The case of the container for rail or road transportation, in which the maximum diameter cannot exceed a certain value but the length may be varied, can be conveniently analyzed on the assumption that the ends are spherical, so its shortest length and minimum volume are those of a sphere having the permitted diameter. In this case the thickness of the insulation is greatly restricted, so it will be assumed that the thickness is constant. This means that the heat leak through the insulation will be proportional to the surface area both for high-vacuum insulation and for porous insulation. It should be emphasized that this does not imply that the effectiveness of the various insulations is the same. It only means that in this circumstance the heat leak for unit area is constant for a given type of insulation and is not a function of the total area. Then, if we again ignore the heat leak through the supports,

$$W=C\,[4\pi r^2+2\pi r(L-2r)],$$

where C is a constant, r is the maximum permissible radius, and L the length of the container. The fractional evaporation is

$$\frac{W}{L_v\rho V}=\frac{2CL}{L_v\rho r(L-\frac{2}{3}r)}.$$

As one would expect, the fractional evaporation changes very little with length, decreasing by only one-third when the length of the container is changed from $2r$ to infinity.

3.4. Comparison of Evaporation Rate Versus Size for Different Vessels

Figure 2 shows graphically how the fractional rate of evaporation depends upon the volume of the container for the three conditions just discussed. It should be pointed out that the three curves should be compared with each other in regard to trend, not in regard to magnitude. The actual rates of evaporation can be determined only by computing the heat leaks for the particular insulation being used.

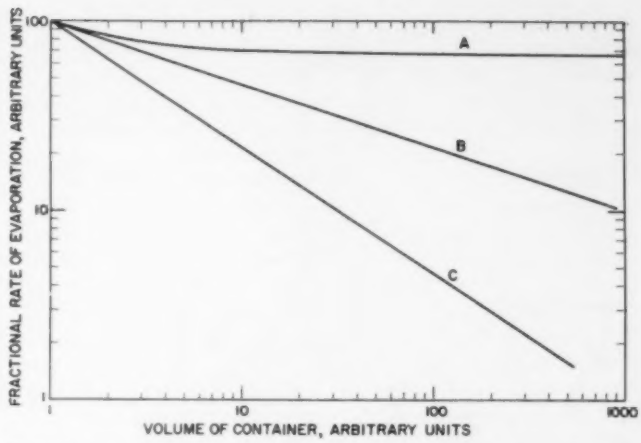

FIGURE 2. *Dependence of the evaporation rate upon the size of the vessel.*

A, Vessels of fixed diameter and various lengths; B, high-vacuum-insulated containers or containers having constant insulating thickness and similar geometry; C, powder-insulated vessels of similar geometry throughout, including a constant ratio of insulating thickness to the other linear dimensions of the vessel.

3.5. Convenient Formula for Porous Insulation

A good approximation for the heat transfer through a porous insulation of constant thickness in a vessel of conservative shape is given by

$$W=\frac{\bar{k}(T_2-T_1)}{t}\times\sqrt{A_1A_2},$$

where $\bar{k}$ is the mean effective thermal conductivity between the tempertaure T_2 and T_1, T_2 is the temperature of the outer surface, T_1 is the temperature of the inner surface, A_1 and A_2 are the areas of the inner and outer surfaces respectively, and t is the thickness of the insulation. This formula is exact for concentric spheres. For cylinders with spherical, dished, or elliptical heads it has been estimated that the formula will give results within 5 percent if the thickness of the insulating space is not more than 50 percent of the radius of the cylinder. It is correspondingly reliable for other shapes in which the thickness of the insulation is a small fraction of the minor perimeter of the vessel. In reporting values of the thermal properties of insulators, the mean effective thermal conductivity is often given between commonly encountered temperatures. If the available data are presented in the more general form of instantaneous conductivities as a function of temperature, the mean effective thermal conductivity can be obtained from the relation

$$\bar{k}=\left[\int_{T_1}^{T_2}k\,dT\right]/(T_2-T_1),$$

where k is the thermal conductivity at temperature T. If k is a linear function of T, $\bar{k}$ is the arithmetic mean conductivity between T_1 and T_2.

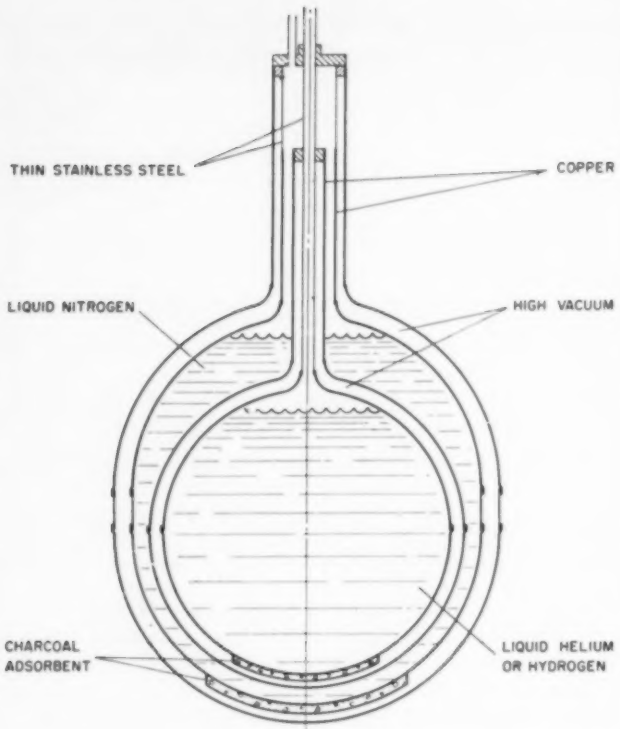

FIGURE 3. *Simplified cross section of a Dewar vessel with a liquid-nitrogen-cooled shield.*

4. Shield Cooled With Liquid Nitrogen

The vessels described in references [1] to [6] use liquid nitrogen to reduce the rate at which heat reaches the liquid helium or hydrogen being stored. In some cases the Dewar is simply immersed in liquid nitrogen contained in a larger vessel. Other designs are of unit construction, like that shown in figure 3, in which there is a liquid-nitrogen-cooled shield suspended in the vacuum between the inner container and the warm wall. Most of the heat entering from the exterior is absorbed by the relatively inexpensive liquid nitrogen. This design is the most effective yet produced and is the most practical for storing small quantities of liquid hydrogen and helium. However, as the size of the vessel increases, the fractional evaporation rate without the shield decreases, and eventually a point is reached at which the extra initial cost of the liquid-nitrogen-cooled shield and the cost and bother of supplying liquid nitrogen are not worth the extra saving of the liquid being stored. This change-over point depends on the relative costs and heats of vaporization of liquid nitrogen and the liquid being stored.

5. Vapor-Refrigerated Shields

The vapor leaving the inner container of an insulated vessel is normally at a temperature very near the boiling temperature of the liquid being stored. This cold vapor constitutes a source of refrigeration that can be used to absorb some of the heat leaking into the vessel. In most vessels some of this refrigeration is utilized more or less accidentally in absorbing some of the heat which flows by solid thermal conduction down the vent pipe. An analysis of this process will be given later.

A way to make good use of the refrigeration available in the escaping vapor is to have it cool a shield suspended between the inner liquid container and the outer warm wall of the vessel. This device can be applied to high-vacuum-insulated vessels, as well as vessels utilizing evacuated-powder insulation. The openings in the shield required to admit piping and supports or reentrant irregularities that may be produced by attaching piping to one side of a shield will have little effect when powder insulation is used, but when the shield is in an empty space these openings and irregularities may somewhat reduce the effective over-all reflectivity of the shield. Moreover, in a vessel having sufficient room between the walls to accommodate a shield, the insulation thickness may be great enough to show a substantial improvement when powder is used. Because of the simpler construction and the fact that the ideal is more nearly approached, it is believed that the vapor-cooled shield is more aptly applied to a vessel with evacuated-powder insulation.

Some commercial powder-insulated vessels make partial use of the cold escaping vapor by having it flow through several turns of pipe that lie between the inner and outer walls. It is believed, however, that the available refrigeration can be used more effectively if it is made to cool a shield located at the optimum position between the inner and outer walls of the insulating space.

The following analysis presents the general method of determining the optimum location of a vapor-cooled shield and the expected gain in performance. The results are applied to the specific case of spherical containers for liquid hydrogen and helium with evacuated perlite insulation.

With evacuated-powder insulation filling the entire insulating space, the rate at which heat reaches the liquid is

$$W_1=\frac{4\pi k_1 r_1 r_2(T_2-T_1)}{r_2-r_1}=\dot{m}L_v, \tag{1}$$

where k_1 is the mean thermal conductivity of the powder in the temperature range T_1 to T_2, r_1 is the radius of the liquid container, r_2 is the radius of the vapor-cooled shield, $\dot{m}$ is the mass rate of evaporation, and L_v is the heat of vaporization of unit mass of the liquid.

The rate at which heat reaches the shield is

$$W_2=\frac{4\pi k_2 r_2 r_3(T_3-T_2)}{r_3-r_2}=\dot{m}L_v+\dot{m}\Delta h, \tag{2}$$

where r_3 is the radius of the outer boundary of the insulation, k_2 is the mean thermal conductivity of the powder in the temperature range T_2 to T_3, and Δh is the change of specific enthalpy of the vapor as it is warmed from T_1 to T_2.

Dividing (1) by (2) gives

$$\frac{L_v}{L_v+\Delta h}=\frac{k_1}{k_2}\frac{(r_3-r_2)}{(r_2-r_1)}\frac{r_1}{r_3}\frac{(T_2-T_1)}{(T_3-T_2)}.$$

Let $r_3=ar_1$ and $r_2=br_1$, then

$$\frac{a(b-1)}{a-b}=\frac{k_1}{k_2}\frac{L_v+\Delta h}{L_v}\frac{(T_2-T_1)}{(T_3-T_2)}=g.$$

From (1),

$$\frac{L_v\dot{m}}{4\pi r_1}=k_1\frac{b}{b-1}(T_2-T_1). \tag{3}$$

Because b is a function of a and g only, and g and k are functions of T_2 only, $\dot{m}/r_1$ is a function of a and T_2 only.

For each value of a there is an optimum value of T_2 and a corresponding optimum value of b, which will make $\dot{m}/r_1$ a minimum. Because, for a given insulation, k_1, k_2, and g depend only upon the properties of the liquid and vapor, the fixed boundary temperatures T_1 and T_3, and the variable temperature T_2, we can compute values of g for a series of temperatures T_2 in the range $T_1<T_2<T_3$ and use these g's for all subsequent computations dealing with the particular liquid being stored.

Then, for a given value of a, values of $\dot{m}/r_1$ can be computed and the minimum can be determined by graphical means. By plotting $\dot{m}/r_1$ versus the position of the shield, $(b-1)/(a-1)$, the location of the minimum will also yield the optimum value of b, the important design parameter. It will be noted also that for this vessel the rate of evaporation is proportional to the first power of the radius or to $(\text{volume})^{1/3}$, if heat conduction through supports is neglected. Thus this design offers the same premium for large size as that shown in curve C of figure 2.

5.1. Liquid-Hydrogen Containers

A series of computations was made for values of a ranging from 1.05 to 1.5 for a vessel containing liquid parahydrogen with evacuated-perlite insulation. The thermal conductivity of perlite is shown in figure 4, a curve based on two determinations made at NBS, one giving the mean effective conductivity between 304° and 76° K, the other the mean conductivity between 76° and 20° K. These data are admittedly not as complete as they should be for the purpose at hand, but they will serve to demonstrate the usefulness of the vapor-cooled shield in this application. Errors arising from the linear interpolation used in figure 4 are not expected to exceed 20 percent. Additional measurements of the thermal conductivities of powders as functions of temperature are in progress at NBS. The values of Δh were taken from the paper of Wooley, et al. [7].

Figure 5 shows the results of a representative computation for a liquid-hydrogen container. It is seen that at the optimum position of the shield, about 35 percent of the distance from the cold wall to the warm wall, the shielded vessel will have an evaporation rate of about 38 percent of the unshielded vessel. It is seen that the optimum location of the shield is not critical; the curve of $\dot{m}/\dot{m}^*$ has a very flat minimum. It was found that the effectiveness of the shield, $\dot{m}/\dot{m}^*$, at its optimum location is practically the same for values of a ranging from 1.05 to 1.5.

It will be noted that the shield is somewhat warmer than liquid nitrogen. The rate of evaporation will be lower if a liquid-nitrogen-cooled shield is used. The decision about the use of this method rather than liquid-nitrogen shielding will depend upon the relative costs of liquid nitrogen and liquid hydrogen and the cost of keeping the liquid nitrogen shield replenished. Also, the complete design study will include heat leaks from piping and supports, which cannot be resolved here because they are peculiar to the specific application and mechanical design.

It is remarkable also that the temperature of the shield and its optimum location, that is, its distance from the inner container divided by the distance between the inner and outer walls, $(b-1)/(a-1)$, are practically independent of the value of a. This is a consequence of the temperature dependence of the thermal conductivity of the powder and the specific heat of the vapor. As more complete data on the

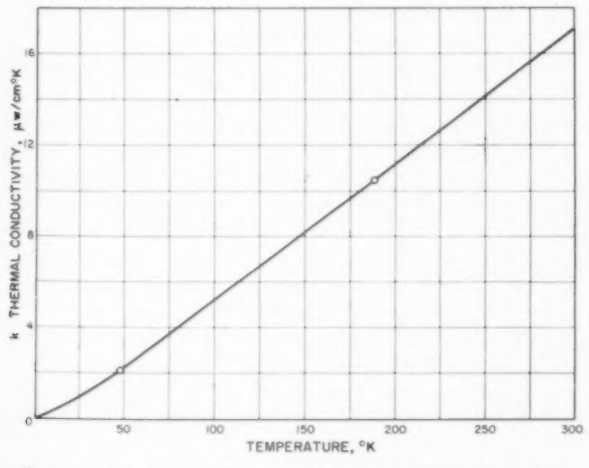

FIGURE 4. *Thermal conductivity of −80-mesh perlite.*

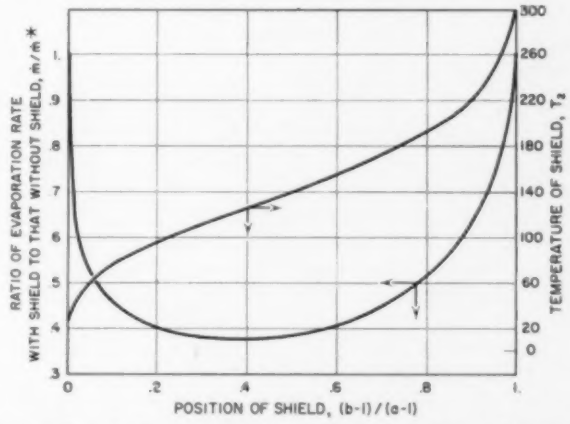

FIGURE 5. *Optimum position and temperature of a vapor-cooled shield in a powder-insulated vessel for liquid hydrogen.*

thermal conductivity of powder insulations become available, the optimum position should be recomputed.

To gain an idea of the performance that might be realized in a practical vessel, the results of these computations were applied to a spherical container for liquid hydrogen having an inner shell 2 m in outside diameter and an outer shell 3 m in inside diameter. This will have a capacity of slightly more than 4,000 liters. The evaporation rate resulting from heat leak through evacuated-perlite insulation was found to be sufficient to evaporate 25 liters, or 0.62 percent, of the contents per day. A vapor-cooled shield reduces this to 0.24 percent per day.

5.2. Containers for Liquid Helium

It is quite apparent that the effectiveness of the vapor-cooled shield depends upon the ratio of the heat of vaporization of the liquid being stored to the specific heat of the vapor. Accordingly the application of this device to the storage of liquid helium is very attractive because of the favorable ratio between the specific heat of the vapor and the heat of vaporization.

The results of computations for $a=1.5$ fully justified this optimism because it was learned that the vapor-cooled shield of a powder-insulated container for liquid helium at its optimum location will have a temperature of 62° K, substantially lower than that of a liquid-nitrogen-cooled shield. The optimum position of such a shield was found to be $(b-1)/(a-1)=0.25$. The designer should again be cautioned against using this value after more data on the thermal conductivity become available. Measurements now in progress will undoubtedly yield more accurate data for this application.

Applying these results to the 4,000-liter spherical container described above, it was found that the heat leak through the insulation would cause liquid helium to evaporate at a rate of 7.7 percent per day from the unshielded vessel and 0.7 percent per day from the shielded vessel.

5.3. Combination of High-Vacuum and Evacuated-Powder Insulation

A logical refinement of the foregoing design is to use a high vacuum in the space between the coldest wall and the vapor-cooled shield, and powder insulation in the outer space. If the surfaces bounding the vacuum space have a low emissivity, this arrangement will result in a considerable improvement, gained at the expense of greater construction costs. The heat leak to the inner vessel, exclusive of solid conduction, can be computed by a method rather similar to that used earlier. In this case, however, the thickness of the high-vacuum space should be made as small as practical, so we can idealize the problem by assuming that the vacuum space has negligible thickness ($r_1 \cong r_2$). Then the rate at which heat is transmitted to the inner container by radiation from a shield at the temperature T_2 is

$$\sigma \frac{e}{2-e} 4\pi r_1^2 (T_2^4 - T_1^4) = \dot{m} L_v, \tag{4}$$

where σ is the Stefan-Boltzman radiation constant, e is the emissivity of the surfaces facing the vacuum space, r_1 is the radius of the inner container, T_2 and T_1 are the temperatures of the shield and inner container respectively, $\dot{m}$ is the mass rate of evaporation of the liquid being stored, and L_v is its heat of vaporization. The heat that reaches the shield by conduction through the powder is

$$\frac{k_2 4\pi r_1 r_3 (T_3 - T_2)}{(r_3 - r_1)} = \dot{m} L_v + \dot{m} \Delta h, \tag{5}$$

where k_2 is the mean thermal conductivity of the powder, r_3 is the radius of the outer shell at temperature T_3, and Δh is the change in enthalpy of the vapor as it is warmed from T_1 to T_2. Dividing eq (4) by (5) and letting $a=r_3/r_1$ gives

$$\frac{L_v}{L_v + \Delta h} = \frac{\sigma e r_1 (a-1)(T_2^4 - T_1^4)}{(2-e) k_2 a (T_3 - T_2)}. \tag{6}$$

Because Δh and k_2 are functions of T_2 that are not available from analytic expressions, the simplest method of solving this equation for T_2 is to use successive approximations. A general solution cannot be given. The equation must be solved for specific values of r_1 and a. For this reason the performance of the 4,000-liter vessel with an inner diameter of 2 m and an outer diameter of 3 m, described earlier, was computed so that the results can be compared with those resulting from other insulation methods. It was found that with liquid hydrogen, the shield temperature will be 129° K and the evaporation rate will be 0.13 percent per day. When this system is used with liquid helium, the temperature of the shield is 86° K and the evaporation rate 0.33 percent per day. These computations assume an emissivity of 0.02 for the surfaces facing the vacuum space and ignore the heat leak through the supporting members.

5.4. Discussion

Table 1 shows the rates of heat transfer in terms of loss of liquid hydrogen and liquid helium in percent per day for several different types of insulation for a vessel of 4,000-liter capacity. These results do not take account of heat transfer by conduction through the supports nor heat conduction through the residual gas in a high vacuum. It should be emphasized that the designer and fabricator have a great amount of control over these latter sources of heat leak. The length of thermal path through insulating supports is particularly pliant to the ingenuity of the designer. Figure 6 gives a suggestion for increasing the length of supports.

The computations show that the effectiveness of the vapor-cooled shield in powder insulation, $\dot{m}/\dot{m}^*$, is practically independent of the thickness of the

TABLE 1.—*A comparison of the heat leaks through various insulations for a 4,000-liter spherical Dewar*

The outside diameter of the inner vessel is 2 m and, when powder insulation is used, the outer shell has an inside diameter of 3 m. For the cases in which no powder is used, the diameter of the outer shell will be smaller. The emissivity of the surfaces facing the high-vacuum spaces is taken as 0.02.

Insulation	Evaporation rate caused by the heat flow through the insulation (excluding conduction by solid supports and assuming no conduction by residual gas)	
	Liquid hydrogen	Liquid helium
	%/Day	*%/Day*
High vacuum *	4.0	49.0
Evacuated perlite	0.62	7.7
Evacuated perlite plus vapor-cooled shield	.24 (shield temperature=124° K)	0.70 (shield temperature=62° K)
Evacuated perlite plus high vacuum * plus vapor-cooled shield	.13 (shield temperature=129° K)	.36 (shield temperature=86° K)
High vacuum * plus liquid N_2 shield (77° K)	.017	.21

* These are idealized conditions. The vacuum space is assumed to be negligibly thin and the vacuum is assumed to be so good that heat conducted by residual gas can be ignored.

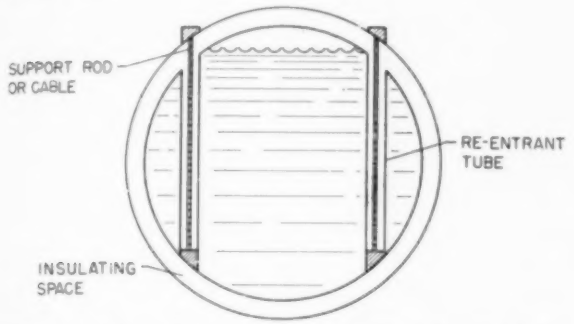

FIGURE 6. *Reduction of thermal conduction through supports by increasing their length.*

insulation, here measured by the constant a. The optimum location of the shield is slightly affected by the thickness of the powder. For the liquid-hydrogen vessel, the optimum position varied from 39 percent of the way from the cold to the warm surface for a=1.05 to 32 percent of the way for a=1.5. The two computations for helium gave 30 percent for a=1.2 and 25 percent for a=1.5. These variations are rather trivial considering the flatness of the minimum in figure 5.

The attainment of a first-rate high vacuum in an insulating space protecting the inner container requires first of all a completely leak-free construction, and also a thorough outgassing of all the metal surfaces bounding the high vacuum. The use of an adsorbent cooled to the temperature of the liquid being stored is highly recommended. The attainment of a superior vacuum is more easily accomplished in vessels for liquid helium storage than in liquid-hydrogen vessels because liquid helium provides a temperature at which all gases except helium have a negligible vapor pressure. Helium is not likely to be found in an insulating vacuum unless there is a leak. It has been observed that commercial containers with liquid-nitrogen-cooled shields have a much smaller heat leak when they are used to store liquid helium than when used with liquid hydrogen, probably because hydrogen gas is very thoroughly condensed when the container holds liquid helium. On the other hand, hydrogen is dissolved in, and is slowly released by, nearly all materials used to construct containers for cryogenic liquids, so provision should be made for its disposal if a high vacuum is to be maintained in vessels for other than helium.

A very obvious extension is the use of multiple shields. Because the cold vapor has a substantial refrigerative value after it leaves the shield discussed here, it is apparent that it could be utilized to cool additional shields.

Another source of refrigeration that could be utilized to cool the shield of a container for liquid parahydrogen is the heat absorbed by para-to-ortho conversion. If the proper catalyst is put into the vent tubes that cool the chield, the endothermic conversion to a higher ortho concentration will provide extra refrigeration. The cooling produced by converting hydrogen of 99.8 percent para (the equilibrium concentration at the normal boiling temperature) to 38.6 percent para (the equilibrium concentration at 100° K) is 44 percent of the cooling produced by warming the gas from the hydrogen boiling point to 100° K.

Finally, a word should be said about the storage of liquid oxygen and nitrogen. Because the ratio of the heat of vaporization to the change in enthalpy of the vapor upon being warmed to room temperature is much greater for these materials than it is for hydrogen and helium, it should be expected that the value of a vapor-cooled shield will be correspondingly less. However, the principles just discussed are equally valid for this application and should be given adequate consideration in the design of vessels for the long-term storage of liquid oxygen and nitrogen.

6. Vapor-Cooled Vent Tube

In those cases in which heat conduction through the supports or fill and vent tubes is a substantial part of the total, it may be worthwhile to use the escaping vapor to intercept part of the heat. This is an important consideration in the vent tubes of

some Dewars. The escaping vapor maintains good thermal contact with the wall of the tube and absorbs a great deal of the heat that would otherwise enter and cause evaporation of the liquid being stored. The maximum possible saving from this process can be computed upon the assumption that the heat transfer between the vapor and the tube is perfect; that both have the same temperature at each level. Also, it is assumed that there is no lateral conduction or radiation to or from the tube. Because, in the temperature regions that are of interest, the thermal conductivity of the tube or support is a function of temperature, the practical solution of the problem can be simplified by assuming that this function is linear, that

$$k=k_0+a(T-T_0),$$

where k is the thermal conductivity at the variable temperature T, k_0 is the thermal conductivity at the cold end, which has the temperature T_0, and a is a constant. Then

$$W=A[k_0+a(T-T_0)](dT/dx), \qquad (7)$$

which is the equation for heat conduction where W_0 is the heat current at any point in the tube, A is the cross-sectional area of the tube, and x is the distance from the cold end. Now the issuing vapor will absorb some of the heat traveling down the tube, so that

$$W=W_0+\dot{m}C_p(T-T_0), \qquad (8)$$

where W_0 is the heat current that reaches the cold end of the tube, $\dot{m}$ is the mass rate of flow of the issuing vapor and Cp is its specific heat.

Upon combining eq (7) and (8) and integrating, it is found that

$$L/A=[1/(\dot{m}C_p)] \times\left[a\Delta T+\left(k_0-W_0\frac{a}{\dot{m}C_p}\right)\ln\frac{W_0+\dot{m}C_p\Delta T}{W_0}\right], \qquad (9)$$

where L is the length of the tube and ΔT the temperature difference between the warm and cold ends.

The thermal conductivities of alloys commonly used for vent tubes of metal Dewars are rather complex functions of temperatures. However, eq (9) can be employed by dividing the total temperature interval into smaller intervals in which the thermal conductivity can be considered to be a linear function of temperature. Then eq (9) is applied to the lowest temperature interval, $\Delta T_1=T_2-T_1$, and the dependence of W_0 upon L_1/A for various values of $\dot{m}$ is determined; L_1 is the length of tube lying in the lowest temperature interval. Then values of heat current W_0' at the bottom of the next higher temperature interval are determined by the relation

$$W_0'=W_0+\dot{m}C_p\Delta T_1.$$

These values of W_0' are then used in eq (9) to compute values of L_2/A for the second temperature interval, and the process is repeated as required. Finally, total values of L/A are obtained by adding the individual values, L_n/A.

For a stainless-steel vent tube for hydrogen it is a sufficiently good approximation to use just two temperature intervals, from 20° to 80° K and from 80° to 300° K. In figure 7 are plotted values of W_0

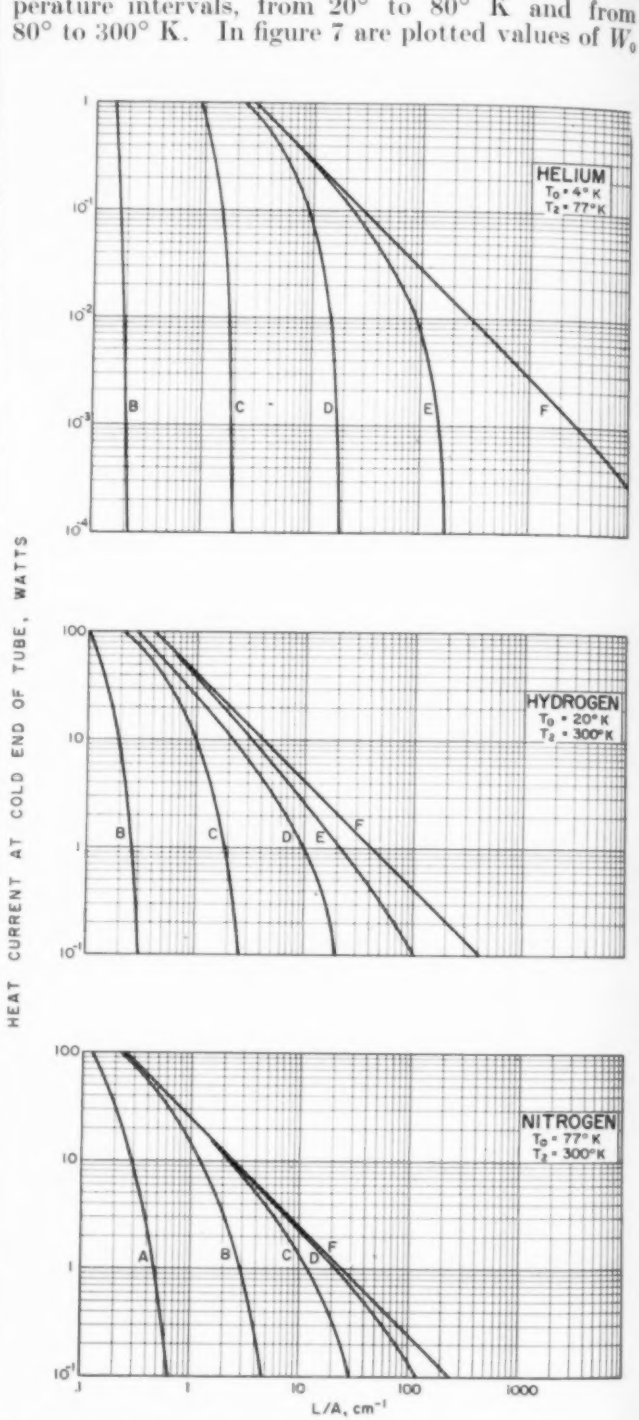

FIGURE 7. *Results of computations of heat current reaching the cold end of a solid conductor counter to a stream of cold vapor.*

A, $\dot{m}=1$ g/sec; B, 10^{-1} g/sec; C, 10^{-2} g/sec; D, 10^{-3} g/sec; E, 10^{-4} g/sec, F, $\dot{m}=0$.

as a function of L/A for stainless-steel vent tubes. It should be remembered that these are limiting values, which assume complete heat exchange between the escaping vapor and the vent tube. In practical vessels, it may be necessary to provide baffles or other means for promoting heat transfer between the escaping vapor and the vent tube to approach the thermal equilibrium assumed for these computations. For hydrogen, which has a variable specific heat, $\dot{m}C_p$ can be replaced by $\dot{m}(\Delta h/\Delta T)$, where Δh is the change of specific enthalpy for the temperature interval ΔT. Values of thermal conductivities of stainless steel were taken from the data compiled by Powell and Blanpied [8].

7. Conclusions

The foregoing analyses show quite clearly that important benefits can be realized by utilizing the refrigerative value of the vapor which escapes from an insulated vessel for liquid hydrogen or helium. The problems were idealized in order to make their solution simpler; thus in many practical designs the values reported in this paper may be substantially altered by the mechanical requirements. However, there is some definite experimental evidence that these computed values are not unrealistic. A 50-liter commercial container for liquid helium, similar to that illustrated in figure 3, protected with a liquid-nitrogen-cooled shield, showed an evaporation loss of 0.35 liter per day. If all this heat leak is attributed to thermal radiation from the shield at liquid-nitrogen temperature, the emissivities of the surfaces facing the vacuum space (assumed equal) are found to be 0.015, which is an excellent value for copper, better than the 0.02 assumed in table 1. This result implies that the heat conduction through residual gas and through the supporting neck of the Dewar was negligible. From the dimensions of the Dewar neck, 15.9 mm o.d., 0.5 mm thick, and 31.8 cm long ($L/A=130$ cm^{-1}), figure 7 shows that if no vapor were escaping, the heat flow down the neck would be about 0.022 w, more than twice that required to cause the observed evaporation rate. However, with the observed rate of evaporation, 0.35 liter per day, 5.1×10^{-4} g/sec, an interpolation [3] of the curves of figure 7 shows that the heat that actually reaches the cold end of the neck is less than 10^{-4} w, a result consistent with the observations. Thus, it appears that a performance very near the ideal has been achieved in a relatively small vessel with a shield cooled with liquid nitrogen. Accordingly it should be entirely practical to approach the ideal in large vessels having either liquid-nitrogen-cooled shields or vapor-cooled shields.

In many applications the neck of the 50-liter helium container described above is inconveniently small. It is possible to increase the neck diameter substantially, keeping the wall thickness and length the same, without seriously increasing the heat flow to the liquid helium. A value of L/A of 80 cm^{-1} will give a heat current of very nearly 10^{-4} w, only 1 percent of the total heat leak. Doubling the diameter of the neck, making $L/A=65$ cm^{-1}, will result in a heat current at the bottom of the neck of 2×10^{-3} w, a 20-percent increase. When the larger neck tubes are used, removable baffles should be provided, both to increase heat transfer between the escaping vapor and the tube, and to stop radiation down the tube.

[3] The spacing of the lower parts of the curves of figure 7 indicates that logarithmic interpolation should be satisfactory in the region under consideration.

The assistance of James A. Brennan in performing the tedious computations is gratefully acknowledged.

8. References

[1] W. F. Giauque, Rev. Sci. Instr. **18,** 852 (1947).
[2] W. E. Henry and R. L. Dolecek, Rev. Sci. Instr. **21,** 496 (1950).
[3] A. Wexler, J. Appl. Phys. **22,** 1463 (1951).
[4] H. L. Johnston, O. D. Gonzalez, and D. White, Rev. Sci. Instr. **22,** 915 (1951).
[5] A. Wexler and H. S. Jacket, Rev. Sci. Instr. **22,** 282 (1951).
[6] S. G. Sydoriak and H. S. Sommers, Jr., Rev. Sci. Instr. **22,** 915 (1951).
[7] H. W. Wooley, R. B. Scott, and F. G. Brickwedde, J. Research NBS **41,** 379 (1948) RP1932.
[8] Robert L. Powell and William A. Blanpied, NBS Circular 556 (1954).

Boulder, Colo., December 14, 1956.

Journal of Research of the National Bureau of Standards Vol. 58, No. 6, June 1957 Research Paper 2765

Further Studies on the Pyrolysis of Polytetrafluoroethylene in the Presence of Various Gases

J. D. Michaelsen and L. A. Wall

The thermal decomposition of polytetrafluoroethylene in the presence of gases or vapors has been explored in the range 450° to 500° C. Gases that have been used can be divided into three groups, depending on whether they inhibit, catalyze, or exert no effect on the thermal-decomposition process. Fluorine-containing gases, i. e., ClF_3 and IF_5, which are capable of dissociating at the pyrolysis temperatures to give fluorine atoms, showed the most marked inhibition yet observed. From the brevity of the duration of inhibition, it is concluded that the fluorine atoms directly attack the polymer to produce scissions through a metathetical reaction.

1. Introduction

Polytetrafluoroethylene is the most thermally stable linear polymer known at the present time. Therefore, a considerable number of investigations have been carried out at the Bureau in an effort to extend its useful temperature range. Polymers of tetrafluoroethylene prepared with different catalysts [1] [1] or with admixed organic and inorganic solids [2] were found not to be different from commercial samples in their rates of thermal volatilization. The lack of inhibitory effects with the admixed solids and their obvious incompatibility with polytetrafluoroethylene suggested that gases that could diffuse into the material would produce more pronounced effects. In a previous article [3] the results of such a study were reported. Both catalysis and inhibition were observed, although some gases or vapors produced no effect.

These results are interpreted in terms of free-radical chain mechanisms [4, 5], which are applicable to the degradation of numerous polymers. In the case of polytetrafluoroethylene the following mechanism appears applicable for its thermal decomposition in a vacuum or under nitrogen.

$$\left.\begin{array}{ll} P \xrightarrow{k_1} R{-}CF_2{-}CF_2{-}CF_2\cdot + R{-}CF_2\cdot & \text{Initiation} \\ R{-}CF_2{-}CF_2{-}CF_2\cdot \xrightarrow{k_2} R{-}CF_2\cdot + CF_2{=}CF_2 & \text{Propagation} \\ \left.\begin{array}{l} 2R{-}CF_2\cdot \xrightarrow{k_4} P \text{ or } 2P \\ \text{and/or} \\ R_mCF_2\cdot \xrightarrow{k_4'} \text{evaporation} \end{array}\right\} & \text{Termination} \end{array}\right\} \quad (1)$$

The P represents any size polymer, R is part of a polymer chain, the k's are the specific rate constants, and R_m is a chain of about 70 carbon atoms.

This picture of the degradation admits the possibility of inhibiting the weight loss of the polymer by increasing the probability of a termination step compared to the propagation (or depolymerization) step.

The earlier study [3] has shown that it is possible to inhibit the degradation of the polymer to some extent by a termination reaction in which a molecule or an atom from the gas combines with the polymer radical. However, along with this inhibition is a catalytic effect, presumably caused by the reaction of an atom with the polymer chain to give a new polymer radical. This catalytic effect also causes a drop in molecular weight. Specifically then, the applicable additional steps for the mechanism of this inhibition with hydrogen is

$$\left.\begin{array}{l} R{-}CF_2{-}CF_2\cdot + H_2 \xrightarrow{k_4''} R{-}CF_2{-}CF_2H + H\cdot \\ R{-}CF_2{-}CF_2{-}R + H\cdot \xrightarrow{k_3} HF + R{-}CF{=}CF_2 + R\cdot \\ H\cdot + H\cdot \xrightarrow{k_4'''} H_2 \end{array}\right\} \quad (2)$$

[1] Figures in brackets indicate the literature references at the end of this paper.

The effect of the k_3 step is to counteract the inhibition produced by the k_4'' step. The net result is a conversion of the unraveling mechanism to a random one, which initially has a very slow rate of volatilization but in subsequent stages becomes faster than the rate under vacuum. As the temperature is raised, the length of the inhibition period becomes less and less, until at 480° C or higher the over-all effect is catalytic.

From this mechanism it is to be expected that the best inhibition step is one in which a very strong bond is formed in the inhibition reaction, whereas a weak bond is formed in the catalytic reaction. In other words, if the inhibiting gas is AB, a strong C—A bond is desired giving a very stable B radical so that BF is labile.

From a consideration of the bond-dissociation energies listed in table 1 it was conceivable that fluorine would have an inhibitory effect. The results of a study along these lines are reported here, along with some experiments with other gases and vapors and with more complicated mixtures, such as an H_2 and NO mixture and Cl_2 and NO mixture.

TABLE 1. *Bond-dissociation energies* [6]

X	X—X	X—F	C—X
	kcal	*kcal*	*kcal*
I	35	.....	53 [9]
Br	45	50 [8]	65
Cl	57	60	78
F	37 [7]	37 [7]	114 [10]
H	100	148	90

2. Experimental Reagents

The polymer used was in the form of a water suspension obtained from E. I. du Pont de Nemours & Co., Inc., and designated by them as TD–3. The suspension was frozen and then dried in a vacuum while frozen, and the powder so obtained was used in the experiments.

The Freons were all from E. I. du Pont de Nemours & Co., Inc., and the bromine, chloroform, cumene, pyridine, aniline, nitrobenzene, and benzaldehyde were obtained from Fisher Scientific Co. in the purest grades available. The NO, Cl_2, ClF_3, and H_2 were the purest obtainable from Matheson Co., Inc. The IF_5 was obtained from the General Chemical Co. as research grade.

The CF_3I was prepared in the Bureau according to the procedure of Henne and Finnegan [11] by the decomposition of perfluoro silver acetate in the presence of I_2 and purification by distillation (bp—22° C).

3. Experimental Procedure

The rate of degradation was measured by determining the weight loss of the polymer after periodic heating under the various flowing gases. The sample of polymer was usually about 1 g in size and was placed in a porcelain boat for heating for all but the corrosive gases ClF_3 and IF_5. For these two gases the samples were heated in a nickel boat, which was found not to corrode during the course of the experiment.

The porcelain boats were heated in a glass tube surrounded with a brass furnace. The temperature was determined by a thermocouple placed in the tube so as to center the space above the porcelain boat. The temperature was regulated with a hand-operated powerstat to ±1° C.

Because of the very corrosive nature of fluorine and the fluorine-halogen compounds, especially at the temperatures of pyrolysis, it was found by experience that a tube of nickel was needed to contain the reaction. For this purpose a special nickel tube was obtained, and its ends were machined so as to fit a 29/42 standard-taper joint. The rest of the apparatus leading to the tube and away from the tube was made of glass. It was attached to the nickel tube by means of two water-cooled joints. Although the glass would corrode during the experiments, this corrosion was slow compared with the over-all duration of the experiments.

A brass furnace placed around the nickel tube was used to bring the tube to the desired temperature. The temperature was measured in the space between the furnace and the nickel tube by an iron-constantan thermocouple. The ends of this space were plugged with asbestos paper.

A typical measurement was made by first placing the boat containing a weighed sample of the polymer in the unheated portion of the tube. The system was then thoroughly flushed with the gas or vapor under study, and a steady flow was established. The temperature of the furnace was brought up to, and maintained at, the desired level. The boat was pushed into the furnace. The manually operated variable transformer sometimes had to be readjusted in order to maintain the desired temperature. Temperature equilibrium was usually reached about 3 to 4 min after the introduction of the boat into the furnace. The time at which the temperature first reached the desired level was taken as the zero time for that particular run. At the end of a given interval of time, usually 1 hr, the boat was withdrawn from the furnace into the unheated part of the tube. This time was taken as the end of the interval of pyrolysis. Experience showed that it made no difference to the results whether the boat was withdrawn from the tube and allowed to cool to room temperature in the air or left to cool in the tube.

When pyrolyzed in a vacuum or under nitrogen, polytetrafluoroethylene was found to retain its original form [3]. In many of the experiments reported here the polymer became very fluid at the temperature of pyrolysis. Although the molecular weight of the polymer could not be determined quantitatively, this change in viscosity from a solid to what is often a very fluid liquid was taken as an indication of a very pronounced drop in molecular weight during the course of pyrolysis under the gases.

The materials with boiling points above room temperature were usually introduced by passing nitrogen as a carrier through the liquid at room temperature and passing the N_2 saturated with the vapor into the system. Water, however, was boiled directly into the flow system in which case the vapor pressure was near atmospheric.

4. Results

The gases studied are divided into three groups according to their effect on the rate of volatilization at 460° and 470° C: (1) Those gases that exhibit a catalytic effect on the rate from the beginning of the study, (2) those that produce little or no effect on the rate, and (3) those that produce an initial inhibitory effect. The gases used and their effects are shown in table 2. Because it has been shown [3] that the rate under N_2 (e. g., 0.017% per minute at 457° C) is quite close to those observed previously under vacuum (e. g., 0.017% per minute at 453° C) [12], the results under N_2 are used as blank runs for comparison purposes in these experiments.

TABLE 2. *Effect of various gases on the thermal decomposition of polytetrafluoroethylene*

Inhibitory	Catalytic	No effect
IF_5	H_2S[a]	N_2[a]
ClF_3	H_2O	$C_6H_5CF_3$[a]
H_2[a]	O_2[a]	Br_2
Cl_2[a]	SO_2[a]	CCl_3H
Cl_2 and NO (10:1)	NO[a]	$C_6H_5NH_2$
CCl_4[a]	H_2 and NO (3:1)	CCl_2F_2
$CClF_2H$	NH_3	CF_3I
$C_6H_5CH_3$[a]	Pyridine	CF_3H
$C_6H_5NO_2$	.....	Cl_2 and NO (1:1)
C_6H_5CHO	.....	.....

[a] Previous work, reference [3].

4.1. Catalytic Effect

The curves representing the degradation of polytetrafluoroethylene under several gases and vapors exhibiting catalytic effects are shown in figure 1, in which the percentage of weight loss of polytetrafluoroethylene is plotted versus time. In these cases the slopes of the curves are greater than that of the blank, i. e., degradation under N_2. The gases shown exhibiting this effect are H_2O, NH_3, and a mixture of 3 moles of H_2 to 1 mole of NO. Pure NO was previously found to be catalytic but not to the extent of this H_2 and NO system, whereas, on the other hand, pure H_2 was found to be an inhibitor at these temperatures [3]. The combination of H_2 and NO seems to have the same effect as an increase in temperature does, i. e., decreases the period of inhibition. Because hydrogen atoms are most surely formed as intermediates in these reactions, it is possible that the NO could increase the steady state concentration of the atoms by catalyzing the rate of initiation of the over-all rate. A steady-state concentration of hydrogen atoms greater than the equilibrium value might have been indicated by the observation that

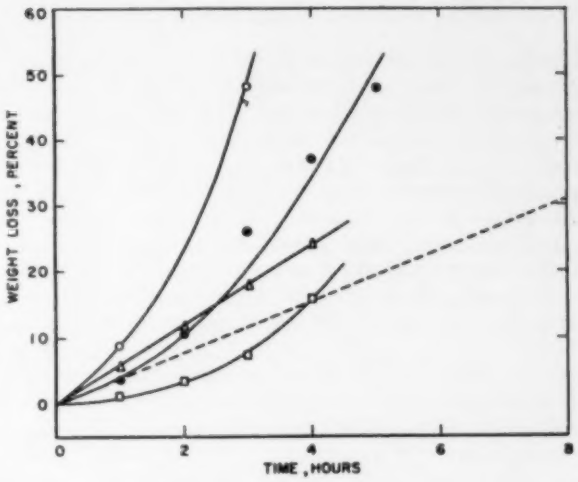

FIGURE 1. *Pyrolysis of polytetrafluoroethylene in the presence of hydrogen-containing gases.*

○, Ammonia; ●, hydrogen and nitric oxide in 3:1 mole ratio; △, water vapor; □, hydrogen; dashed line, nitrogen; temperature 470° C; pressure ~ 1 atmosphere.

the Nichrome wire would glow when inserted into the reaction system above the polymer. The catalysis of the recombination of the atoms on the metal giving a high heat of recombination could cause this. On the other hand, the hydrogen could have reacted with the NO on the wire to give a very exothermic reaction producing N_2 and H_2O. Thus the water produced from the reaction of atomic hydrogen and NO, together with the NO might give the increased catalytic effect of the mixture. Water in a separate experiment was found to have a catalytic effect.

The catalytic effect of the water vapor seems to confirm the suspected polar or ionic character of the C–F bond. This enhanced decomposition of the polymer in the presence of H_2O parallels the behavior of metal fluorides.

The NH_3, besides giving an over-all catalytic effect, was found to be incorporated in the polymer in large proportions. Because of this fact, little can be said about its mode of action.

4.2. No Effect

Those compounds listed in table 2 that show no effect may have some influence on the rate at other temperatures and may interact with the polymer. However, at the temperatures at which these experiments were studied, i. e., 450° to 480° C, the rate of degradation of the polymer under these gases was, within a factor of two, the same as for N_2.

It seems definite, however, that very little, if any, reaction is taking place between the degrading polymer and CF_3I or CF_3H. This is extremely interesting and would seem to indicate either high C—H and C—I bond strengths in these compounds or an exceptional inertness of the CF_3. radical.

4.3. Inhibitory Effect

The best inhibitors, as a study of bond-strength data might lead one to expect, were those that decomposed to give F_2, e. g., ClF_3 and IF_5. Their effects, when compared with those of Cl_2 and N_2, are shown in figure 2; the result that at 480° C these fluorine-containing halides exhibit only a catalytic effect is not shown. When in contact with the fluorine-containing gases the polymer liquefied, and the rate of weight loss approached or surpassed that caused by N_2 after 5 to 7 hours at the indicated temperatures. Although a 1:1 mixture of Cl_2 and NO gave but little effect, a 10:1 mixture had about the same effect as Cl_2 alone, as shown in figure 3.

The polymerization inhibitor, nitrobenzene, was found to be surprisingly good despite its low vapor pressure.

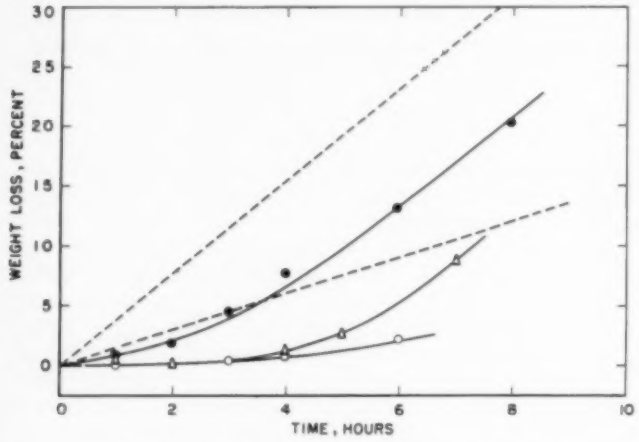

FIGURE 2. *Pyrolysis of polytetrafluoroethylene in the presence of halogen gases.*

●, Chlorine at 470° C; △, chlorine trifluoride at 470° C; ○, iodine pentafluoride at 460° C; upper dashed line, nitrogen at 470° C; lower dashed line, nitrogen at 460° C.

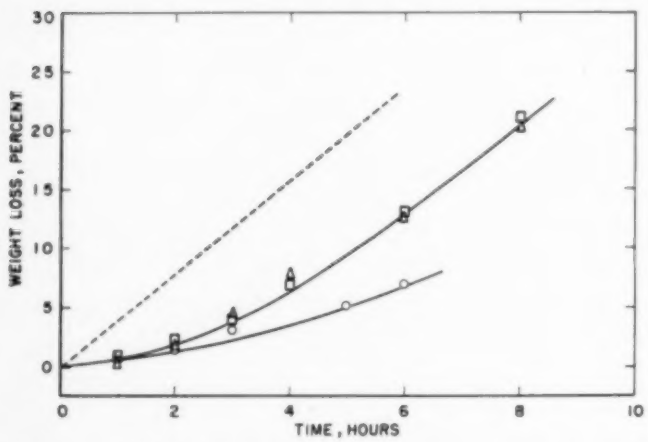

FIGURE 3. *Pyrolysis of polytetrafluoroethylene in the presence of additional gases.*

△, Chlorine; □, chlorine and nitric oxide in 10:1 mole ratio; ○, nitrobenzene; dashed line, nitrogen; temperature 470° C.

5. Discussion

The aim of this work was to find an inhibitor for the thermal decomposition of the polymer that would be effective at 500° C and yet would not cause a rapid decrease in the molecular weight of the polymer. As pointed out in the introduction, the effort was directed to the search for a compound that would terminate the fluorocarbon radical, and still not produce in this reaction a radical that is too reactive. Fluorine was found to be the best inhibitor, but it still apparently caused a certain induced reaction or catalytic effect. There is very likely present a large concentration of F atoms because the bond energy of F_2 is low. A lower concentration of F_2, through the use of IF_5 at its room-temperature vapor pressure, gave no significant increase in inhibition.

Thus, the rapid onset of fluidity in the polymer and the failure to obtain a longer inhibition time than that observed, suggest that F atoms attack the polymer chains in the following manner:

$$F\cdot + {-}CF_2CF_2CF_2{-} \longrightarrow {-}CF_2CF_3 + {-}CF_2\cdot$$

Such reactions are probably more exothermic in the fluorocarbon system than in the corresponding hydrogen-hydrocarbon system. In the latter system the low probability of metathetical reactions has been studied theoretically [13] and experimentally [14]. An important objection to these reactions is the high energy of activation of these steps due to the shielding of the carbon and the low resonance energy in the activated complex resulting from the large displacement of the carbon atom from its equilibrium position.

In the fluorine-fluorocarbon system, however, no alternative low activation process is possible. Also, only a very few breaks need be induced by the above reaction for the process to be entirely random. If such a reaction is ruled out, then one needs to assume a very short kinetic chain length in order to explain the decomposition reaction in the absence of gases. However, this is contradicted by the observed kinetic behavior.

In the previous work [3] with H_2 and Cl_2 it was considered likely that the failure to obtain a greater degree of inhibition was the result of the attack reaction, k_3, by the H or Cl atoms formed by the inhibition reaction, k_4'' (see eq. 2). Consequently, the mixtures of gases, H_2 with NO, and Cl_2 with NO, were tried with the idea that one gas (NO) would inhibit the attack reaction, k_3. From table 2 it is clear that the results were in the opposite direction.

Along with these ideas and results may be placed the fact that an increase in temperature very rapidly increases the rate of catalysis relative to inhibition. Concurrently, changing the partial pressure of the inhibiting gas influences the ratio slightly. This indicates that the order of the rate of inhibition with respect to the inhibiting gas is different from that for the catalytic step. Therefore, steps k_3 and k_4''' must both be important in the kinetic scheme proposed.

This can best be seen from the following considerations. If a steady state in hydrogen atoms exists, then from equations k_4'', k_3, and k_4'''

$$d(\mathrm{H}\cdot)/dt = 0 = k_4''(\mathrm{RCF_2}\cdot)(\mathrm{H_2}) - k_3(\mathrm{H}\cdot)(\mathrm{R{-}CF_2{-}R}) - k_4'''(\mathrm{H}\cdot)^2.$$

When k_4''' step is not important

$$(\mathrm{H}\cdot) = \frac{k_4''(\mathrm{H_2})(\mathrm{RCF_2}\cdot)}{(k_3 R{-}\mathrm{CF_2}{-}R)}.$$

Therefore,

$$\frac{\text{Rate of inhibition}}{\text{Rate of catalysis}} = \frac{k_4''(\mathrm{H_2})(\mathrm{RCF_2}\cdot)}{k_3(\mathrm{H}\cdot)(\mathrm{R{-}CF_2{-}R})}.$$

Substituting for (H·),

$$\frac{\text{Rate of inhibition}}{\text{Rate of catalysis}} = \text{Constant} = 1.$$

Therefore, varying the hydrogen-gas concentration should have no effect on this ratio nor should the temperature.

However, if k_4''' step is very important, then to a first approximation

$$(\mathrm{H}\cdot) = \left[\frac{k_4''(\mathrm{H_2})(\mathrm{RCF_2R})}{k_4'''}\right]^{1/2}.$$

Therefore, substituting for (H·),

$$\frac{\text{Rate of inhibition}}{\text{Rate of catalysis}} = \frac{k_4''(\mathrm{H_2})(\mathrm{R{-}CF_2}\cdot)}{k_3\left[\frac{k_4''(\mathrm{H_2})(R{-}\mathrm{CF_2}{-}\mathrm{R})}{k_4'''}\right]^{1/2}} = \frac{[k_4''k_4'''(\mathrm{H_2})(\mathrm{R{-}CF_2}\cdot)]^{1/2}}{k_3(\mathrm{R{-}CF_2{-}R})}.$$

Consequently, by lowering the partial pressure of the inhibiting gas, there should be an increase in the catalytic effect relative to inhibition. Also, as an increase in temperature in these experiments decreases the inhibitory period, or rather markedly increases the rate of catalysis over a 10 to 20 deg C range, $E_3 >> E_4'''$, since $E_4''' = 0$.

Therefore, once a free radical or atom is formed in step k_4'' that will enter into reaction in step k_3, it is better that $E_3 < E_4$. Then inhibition increases faster with temperature than catalysis. No example of this type was observed in these experiments.

The results in table 2 show a few anomalies. The first is the inhibitory effect of CCl_4 and $CClF_2H$ compared with no effect of CCl_3H, CF_3H, and CCl_2F_2.

The effectiveness of the low-temperature polymerization inhibitors, nitrobenzene and benzaldehyde, is surprising. Their effect is to be contrasted with those of aniline, which gave no over-all effect at these high temperatures; pyridine, which acted much like ammonia; and benzotrifluoride, which had previously [3] been shown to have no effect. The aniline showed a slight inhibitory effect, but it was less than a factor of two at these temperatures. Its slight effect on the rate data could be attributed to its very slow solution into the bulk polymer.

According to the bond data given in table 1 and the discussion given in the introduction, the behavior of Br_2 should contrast with that of F_2. Bromine has no effect, whereas fluorine-containing halides are very good inhibitors, as can be seen in table 2.

The results in general indicate that very good inhibitors for the thermal decomposition of fluorine-containing polymers are within the realm of possibility. It is also evident from table 2 that relatively small changes in molecular structure or chemical composition play a large role in the behavior of a given substance. Thus achievement of the utmost possible degree of inhibition will require a large amount of investigation because of the obvious necessity to balance critically the various factors.

6. References

[1] R. E. Florin, L. A. Wall, D. W. Brown, L. A. Hymo, and J. D. Michaelsen, J. Research NBS **53,** 121 (1954) RP2524.
[2] J. D. Michaelsen and S. Straus, NBS, unpublished experiments.
[3] L. A. Wall and J. D. Michaelsen, J. Research NBS **56,** 27 (1956) RP2644.
[4] R. Simha, L. A. Wall, and P. J. Blatz, J. Polymer Sci. **5,** 615 (1950).
[5] R. Simha and L. A. Wall, J. Phys. Chem. **56,** 707 (1952).
[6] A. G. Gaydon, Dissociation energies and spectra of diatomic molecules (Dover Publications, Inc., New York, N. Y., 1950).
[7] H. Wise, J. Phys. Chem. **58,** 389 (1954).
[8] G. Herzberg, Molecular spectra and molecular structure: I. Diatomic molecules (Prentice-Hall, New York, N. Y., 1939).
[9] Measured by NBS Mass Spectrometry Section from CH_3I. (Private communication.)
[10] R. M. Potocki and D. E. Mann (informal communication).
[11] A. L. Henne and W. G. Finnegan, J. Am. Chem. Soc. **72,** 3806 (1950).
[12] S. L. Madorsky, V. E. Hart, S. Straus, and V. A. Sedlak, J. Research NBS **51,** 327 (1953) RP2461.
[13] F. O. Rice and E. Teller, J. Chem. Phys. **6,** 489 (1938).
[14] R. E. Varnerin, J. Am. Chem. Soc. **77,** 1426 (1955).

Washington, October 22, 1956.

Journal of Research of the National Bureau of Standards Vol. 58, No. 6, June 1957 Research Paper 2766

A Nonlinear Instrument Diaphragm

Fidel Cordero, Harry Matheson, and Daniel P. Johnson

Details of fabrication for the production of sensitive diaphragms having a controlled nonlinear pressure-deflection characteristic are presented. The desired characteristic was such that when the diaphragm formed one plate of a condenser in the frequency-controlling network of a Wien-bridge oscillator, the resulting pressure-frequency transfer characteristic would be linear between −30 and +30 dynes per square centimeter. Typical transfer curves are shown.

1. Introduction

The diaphragm described herein was required to have a deflection versus pressure characteristic such that, with the diaphragm as the moving plate of a condenser inserted in the frequency-controlling circuit of a Wien-bridge oscillator, the frequency deviations of the oscillator would be proportional to the pressure difference across the diaphragm. For a Wien-bridge oscillator the frequency-capacitance relation for variation of one capacitor is $f \propto C^{-1/2}$. Assuming an ideal parallel-plate condenser, the wanted pressure-displacement relation over the working range of the diaphragm was $p \propto d^{+1/2}$. The imperfect inverse proportionality between capacitance and plate separation in a physically realizable condenser necessitated some empirical adjustment of the diaphragm configuration to obtain the required characteristic.

Additional specifications for the diaphragm-oscillator combination called for a sensitivity of 0.3- to 1.0-percent frequency change per dyne per square centimeter, good linearity between −30 and +30 d/cm^2, and good long-time stability. In addition, the diaphragm was required also to tolerate momentary overpressure of the order of 1,000 d/cm^2.

2. Description of Diaphragm

2.1. Forming Die

The diaphragms were pressed from 0.001-in.-thick commercial soft-brass shim stock. Figure 1 shows the arrangement of the 4 circumferential and 60 radial corrugations impressed in a finished diaphragm. Not discernible in the photograph is the slight concavity, or cupping, imparted to the diaphragm during the forming operation.

The combined effect of the radial corrugations and concavity compels the diaphragm to execute an umbrella-like motion when pressure is applied. It is more compliant when pressure is applied to its convex side than to its concave side.

Figure 2 gives the essential dimensions of the die. Each radial groove was 0.015 in. deep at its outer end and 0.005 in. deep at its inner end, and the central areas were depressed 0.005 in. with respect to the circumferential flats. Although the grooves in the die were cut with a sharp V-pointed tool, the forming pressure was not great enough to force the metal to the bottom of the grooves. As a result, the cross sections acquired by the corrugations were nearly arcs of circles.

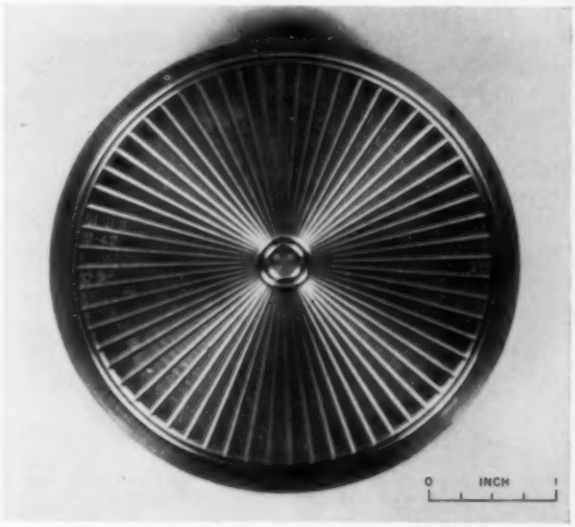

FIGURE 1. *Matrix for forming a nonlinear diaphragm.*

Earlier dies had a single, small hole at the center to allow escape of air during the forming operation. Later dies were provided with holes for each circumferential groove. In addition, the edges of the circumferential grooves of later dies were rounded to reduce the tendency of the sheet metal to tear during the forming operation. This rounding also resulted in more uniform characteristics in the finished diaphragms. The surface of the die, including the grooves, was brought to a medium polish.

2.2. Diaphragm Fabrication

Annealed brass shim stock, commercially available in rolls 6 in. wide, was first examined for pinholes under back lighting. Disks, somewhat greater than 3½ in. in diameter, were cut out of pinhole-free areas with scissors, using care not to kink the material. Similar disks were cut from unbleached paper. Two of the brass and three paper disks were then interleaved, clamped between brass blocks in a lathe, and turned to the final diameter.

The diaphragms were formed by pressing them against the clean oilfree die in a hydraulic press arranged as shown in figures 3 and 4. One of the

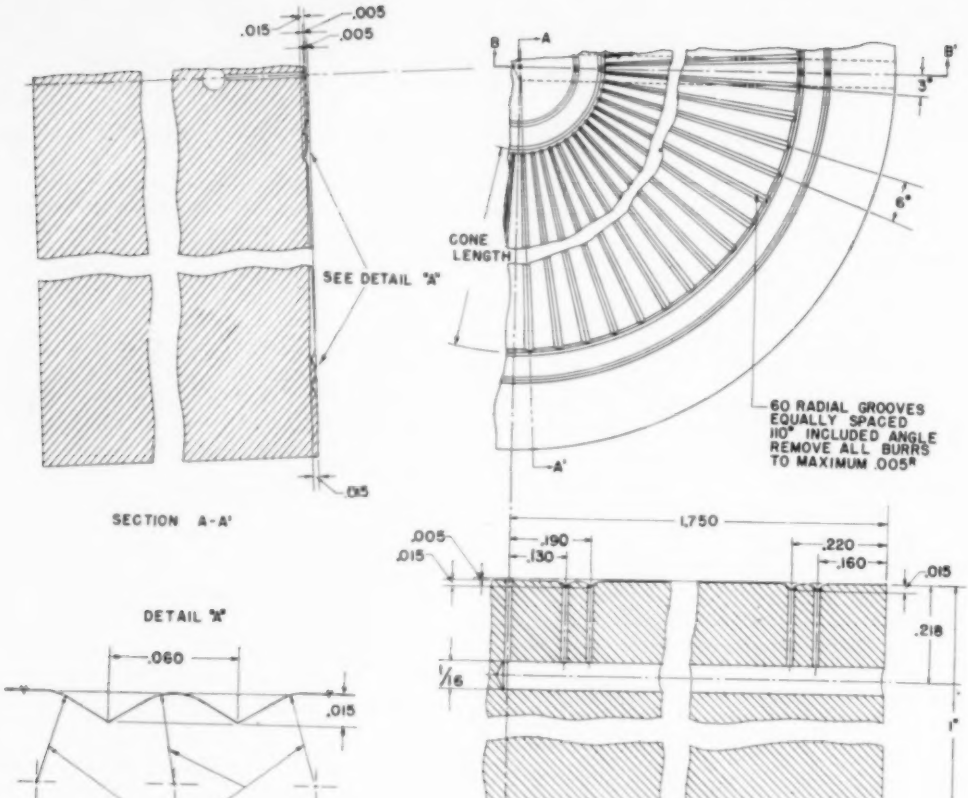

FIGURE 2. *Drawing for reproducing a matrix.*

Note that each radial groove is 0.015 in. deep at its outer end and 0.005 in. deep at its inner end and that the central areas are depressed 0.005 in. with respect to the circumferential flats.

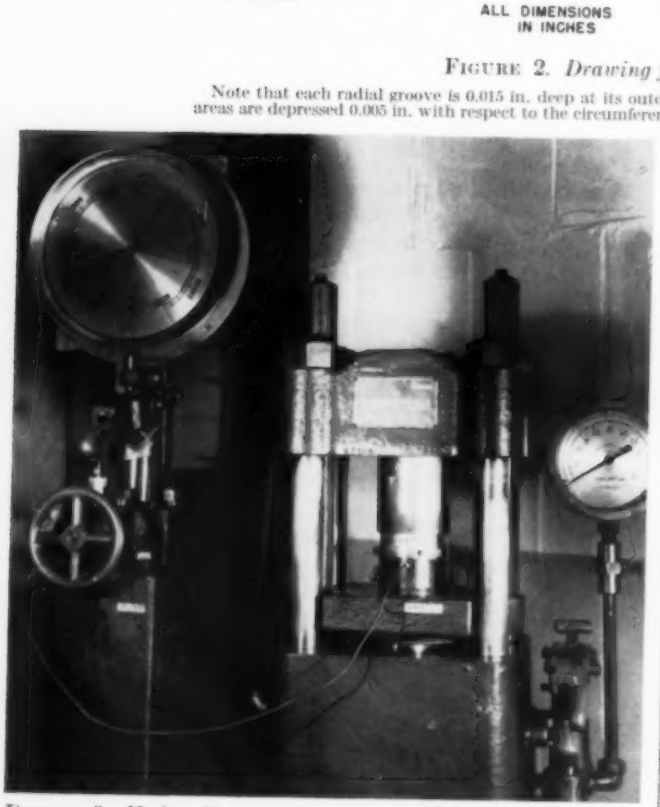

FIGURE 3. *Hydraulic press arranged for forming diaphragms, using dental dam.*

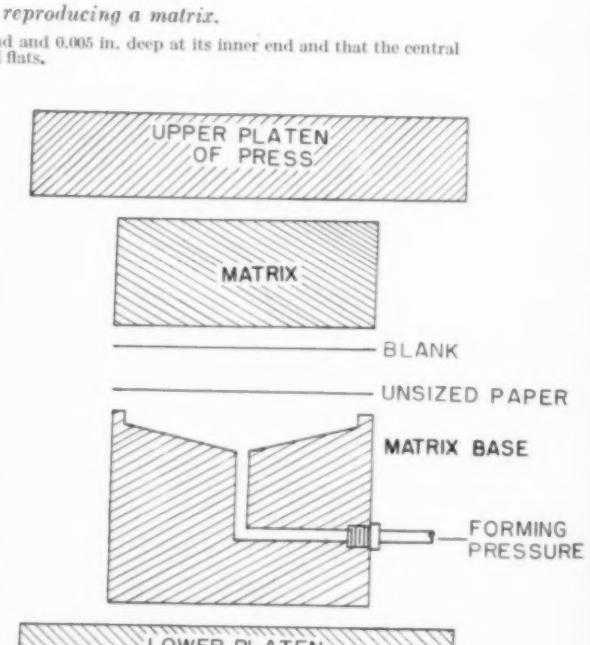

FIGURE 4. *Original arrangement of equipment for forming diaphragms.*

paper disks was used as a gasket to seal the joint between the lower platen and the diaphragm. After the press was closed with a force of 10 tons concentrated on an annulus 0.170 in. wide at the edge of the diaphragm, the diaphragm was formed by the application of 1,500 psi for several seconds.

After release of the forming pressure, the press was opened and the die was removed. Absence of oil on the face of the die indicated that the diaphragm was not torn during the forming process. The diaphragm and paper gasket were carefully slid off the annulus of the lower platen and the gasket peeled from the diaphragm. The diaphragm was rinsed in petroleum ether, using a wire holder, carefully examined for pinholes and tears under back lighting, and stored in a cardboard rack.

More recently the fabrication procedure has been modified either as a matter of convenience or because it was felt that a more uniform product resulted. The modifications were

(1) The blanks were cut without paper interleaves, turning the lathe by hand and using a razor blade as a cutting edge.

(2) Rolled edges and burrs on the disks were removed by laying the blank on a piece of plate glass and dragging a razor blade over the edge of the blank to straighten the edge.

(3) The blank was protected from the hydraulic fluid by a sheet of dental dam. The dam was clamped between brass rings and was held over the bottom platen. The rings also served to center the blank and die for forming.

(4) Lens paper was substituted for the bulkier, unsized paper and placed between the blank and the dental dam.

(5) After forming the diaphragm it was removed from the recess formed by the brass rings and dental dam by gently touching its edge with scotch tape and lifting it from the recess.

(6) The petroleum ether dip was omitted.

Once a diaphragm was formed, it became essential not to handle it by the edge or in any manner that would produce distortion across a chord or diameter.

3. Proof Tests

The diaphragms were formed against a die with the center recessed 0.005 in. When the forming pressure was removed, the central part of the diaphragm sprang away from the die, so that the center of the diaphragm was above the plane of the rim, i. e., the diaphragm acquired a cupped shape.

3.1. Cupping and Compliance

For measurement of cupping and compliance, the diaphragms were mounted in a jig consisting of two brass disks with clamping rings cut on their mating surfaces. The jig was mounted to hold the diaphragm horizontally on the carriage of a milling machine. The position of the diaphragm was detected by a fixed-wire probe connected to an electronic indicator (capacitance bridge). The diaphragm was brought into contact with the probe by moving the carriage vertically or horizontally by the positioning screws of the carriage. Displacements were measured with the micrometers on the positioning screws.

Most of the diaphragms showed a cupping of 0.004 to 0.008 in., with occasional values as low as 0 and as high as 0.015 in. or more. As no direct relation between cupping and either sensitivity or dynamic range was observed, diaphragms whose cupping was within the range 0.004 to 0.008 in. were considered acceptable for further testing.

The mechanical compliance of each diaphragm was measured by determining the pressure necessary to produce central displacements of +0.010, +0.005, −0.005 and −0.010 in. of the diaphragm. Some typical values are shown in table 1. A water-filled manometer with a 1:20 slope was adequate for determining the pressure.

TABLE 1. *Mechanical compliance of representative diaphragms*

Diaphragm	Pressure for the following deflections in inches [1]				
	+0.010	+0.005	0	−0.005	−0.010
	d/cm²	d/cm²	d/cm²	d/cm²	d/cm²
208	+134	+53	0	−38	−67
170	+125	+47	0	−35	−61
226	+124	+49	0	−37	−64
222	+135	+52	0	−38	−66
162	+118	+45	0	−31	−53
249	+134	+51	0	−37	−64
33	+144	+52	0	−33	−52
14	+130	+47	0	−32	−49
10	+142	+54	0	−34	−57
9	+144	+53	0	−36	−58

[1] The diaphragm moves toward the backplate for a positive pressure difference.

The mechanical compliance was not found to be directly related to the observed sensitivity or dynamic range of a finished capsule, probably because of the effect of clamping pressure discussed below. However, the measurements did serve to reject diaphragms that were obviously too stiff, too compliant, or for which the curvature of the load-deflection curve was obviously wrong. It was occasionally surprising to see two diaphragms with quite similar mechanical compliances result in finished capsules, one of which would be quite satisfactory, whereas the other showed only a limited linear range.

3.2. Pressure-Frequency Relation

After completion of the mechanical tests the diaphragm was mounted in its permanent holder, or capsule, as shown in figure 5, and the backplate was

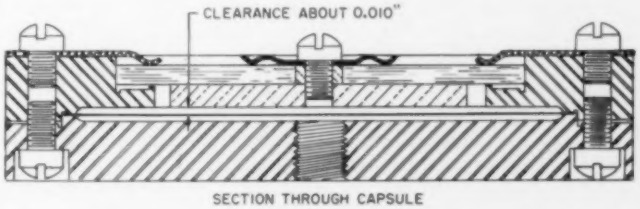

FIGURE 5. *Cross-sectional sketch of assembled capsule showing the relative positions of the diaphragm and backplate.*

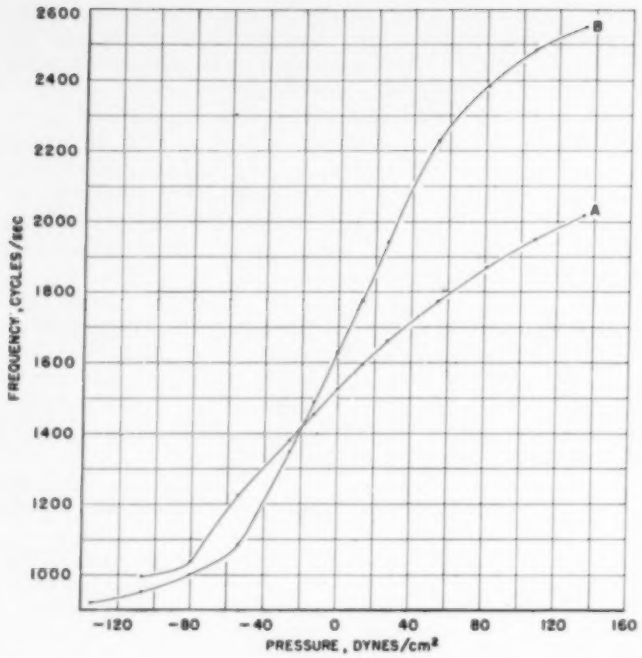

FIGURE 6. *Pressure-frequency relations for capsule-oscillator combinations with adequate linear range.*

A, Minimum acceptable sensitivity; B, excellent sensitivity. The diaphragm moves away from the backplate for a positive pressure difference.

shimmed to give an electrical capacitance of 100 ± 5 $\mu\mu$f. Final acceptance of a diaphragm was based on a plot of the pressure difference across the diaphragm in its own capsule against the frequency of a Wien-bridge oscillator connected to the capsule. For these measurements the pressure differences were obtained with a gas-pressure balance.

Calibration curves for two diaphragms with extreme characteristics are shown in figure 6. Except when intended for special purposes, the minimum acceptable linear range was from -25 to $+25$ d/cm ^{2} and the acceptable range of sensitivities in the linear region was 5 to 11 cps per d/cm^2.

4. Capsule

The diaphragm was clamped in a capsule body consisting of two heavy-brass rings, a backplate, an insulating glass plate, and miscellaneous screws and fittings. Figure 7 shows the parts in an exploded view. The three critical surfaces were the two that clamp the edge of the diaphragm and that which positions the glass plate in the top half of the capsule body, figure 5. Where it was necessary to seal the interface between the glass plate and capsule body and the threads of the backplate against leaks of air, a silicone grease was found to be satisfactory.

To avoid electric short circuits in a capsule when the diaphragm was subjected to excessive pressure, the exposed surface of the backplate was coated with an insulating lacquer.

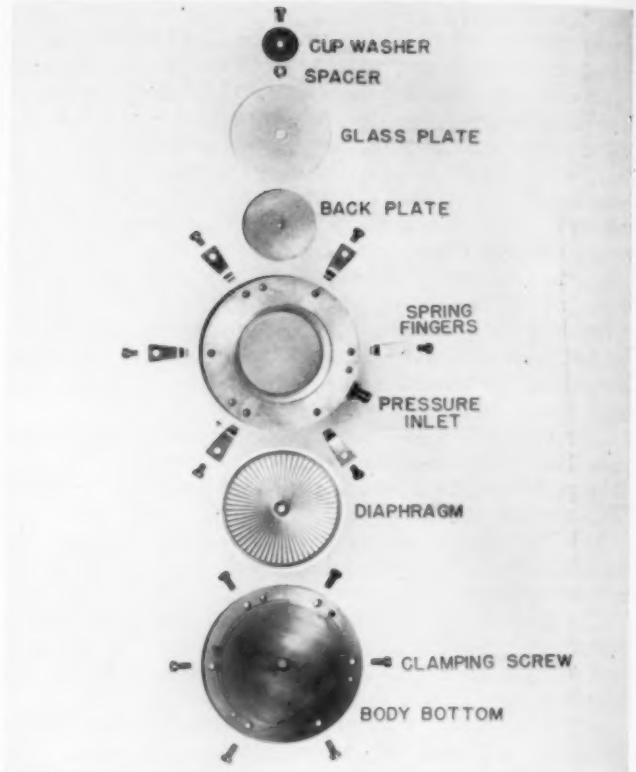

FIGURE 7. *Parts of a complete capsule for comparison with figure 5.*

The two halves of the capsule body were held together by six 10–32 brass screws. A study of the optimum clamping pressure showed, surprisingly enough, that very small distortions of the capsule body were often essential to obtain optimum characteristics.

4.1. Transfer Characteristic

The family of curves in figure 8 are typical of the pressure-frequency transfer characteristics of a capsule-oscillator combination. A number of diaphragms, made from the same roll of material and formed on the same die, showed essentially the same family. Curve Aa was obtained with the clamping screws barely tight. Tightening the clamping screws with a torque screwdriver in 5-in.-lb increments produced progressively higher sensitivities and improved linearity up to 20 in.-lb of torque. Note that for 25 in.-lb the curve is quite unsymmetrical and the linear range is markedly reduced. A quite similar family of curves could be obtained by loosening all screws and progressively retightening them, but not by progressive loosening only.

Attempts have been made to determine the volume compliance of these diaphragms at the rest-point. The results indicate a range of about 0.002 to 0.008 cm^3 per d/cm^2.

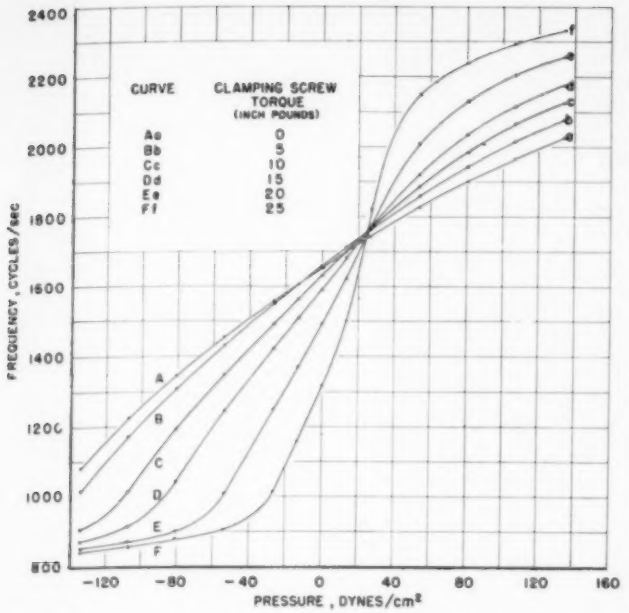

FIGURE 8. *Curves showing the effect of clamping pressure, on a diaphragm, on the transfer characteristics of a capsule-oscillator combination.*

4.2. Serviceability

The unmounted diaphragms had to be handled with considerable care. Injudicious flexing of an unmounted diaphragm impaired its performance, probably because the cupping was disturbed. Even edge damage limited to the portion of the diaphragm that was firmly clamped, altered the pressure-deflection characteristics. In practice, the diaphragms were never handled with the fingers or with tweezers but were manipulated on sheets of paper by tilting the paper to slide the diaphragm as required. Diaphragms could be picked up from a flat surface by slipping a sheet of paper under them and lifting the paper. When necessary, they could be grasped safely between thumb and finger at the center. Storage and shipment in paper envelopes with a cardboard stiffener against the back of the diaphragm has been quite successful, provided the surfaces of the envelope were protected from pressure. Prolonged storage of diaphragms at high humidity produced surface staining, which, though unsightly, had no detectable effect on performance.

Diaphragms have, on many occasions, been removed from a capsule and returned to it without detectable effect on the pressure-frequency curve.

Over 1,200 capsule-months of operation have shown that the diaphragms will remain stable in sensitivity and rest-point when subjected to alternating pressures up to 100 d/cm² at intervals of several minutes. The service life of an assembled capsule is known to exceed 2 years and appears to be indefinite. Observations over a period of months indicate that the sensitivity of a capsule may increase on the order of 5 percent a year.

No data is available on temporary or permanent changes in rest-point resulting from long sustained pressure difference across representative diaphragms. One series of experiments on a single diaphragm indicated that a momentary pressure of 4,000 d/cm² produced a detectable effect on the rest-point. The momentary application of 6,000 d/cm² shifted, at least temporarily, the pressure-frequency curve of the capsule-oscillator combination, but the diaphragm was judged to be still serviceable.

WASHINGTON, November 9, 1956.

Journal of Research of the National Bureau of Standards Vol. 58, No. 6, June 1957 Research Paper 2767

Optical Studies of Crazed Plastic Surfaces[1]

Sanford B. Newman and Irvin Wolock

Optical studies were made of crazed surfaces, principally those of cast polymethyl methacrylate. The techniques used for these studies were multiple-beam interferometry and light and electron microscopy.

The dimensions of the craze cracks produced by short-time stress crazing and by stress-solvent crazing were determined by the above techniques. Stress-crazed specimens contained the smallest cracks observed during this investigation. The dimensions determined in some of these specimens were: Length, 2 to 10 microns; width, 0.1 to 0.25 micron; depth, 0.05 to 0.15 micron. In other specimens and in solvent-crazed surfaces the dimensions were larger. The craze cracks did not appear to approach dimensions unresolvable by the electron microscope, but instead appeared to have a minimum crack length.

An elevation of the surface in the vicinity of craze cracks was observed, of the order of 0.02 micron for cracks produced by stress-crazing and 0.3 micron for those produced by stress-solvent crazing. This rise was observed in crazed specimens while still under load. The typical surface displacement was observed in specimens crazed in tension produced by flexure as well as in pure tension, and was observed in polystyrene and in polymethyl alpha-chloroacrylate as well as in polymethyl methacrylate.

Some crazed specimens in which the crazing had apparently "recovered" when viewed with the unaided eye still exhibited the surface displacement typical of crazed specimens. Experiments conducted by heating stress-crazed specimens and stress-solvent-crazed specimens to accelerate the recovery of crazing indicated that surface recovery is essentially complete in the former case but not in the latter. This difference in recovery behavior is probably due to the nature of the deformation associated with the two types of crazing.

Tensile specimens to which loads had been applied that were slightly too low to produce immediate crazing did not exhibit surface displacements typical of crazed specimens.

1. Introduction

When transparent thermoplastics such as polymethyl methacrylate or polystyrene are exposed to a sufficiently high tensile stress or to solvents, deterioration of their optical properties occurs. This deterioration results from the formation of cracks that impair light transmission, cause optical aberrations, and reduce the strength properties of the material. Commonly known as "crazing," this phenomenon is encountered in a variety of products ranging from aircraft glazing and canopies to watch crystals, and is obviously of considerable economic importance to manufacturers and users of plastic items. A number of investigators have reported the results of work on the mechanism, characteristics, and elimination or prevention of crazing [1 to 7].[2] However, crazing remains a serious consideration in plastics applications and many aspects of the problem require intensive study.

Photomicrographs and descriptions of the craze cracks can be found in the literature [2, 4, 5]. The cracks vary greatly in their length and fineness. In tensile specimens crazed by the application of stress or by stress and solvent together, the cracks are almost invariably normal to the applied stress. Individual cracks can usually be observed using a low-power microscope; a 16-mm objective and 10× ocular is generally more than adequate. The length and number of the cracks can often be determined in this fashion. Some crazed surfaces contain cracks that appear to approach the limits of resolution of the microscope, and these require a more powerful tool for the measurement of crack dimension.

Although the length and fineness of crazing cracks can be studied with the bright-field microscope, the determination of the depth of cracks and how they affect surface topography requires other techniques and instruments. Both the electron microscope and the multiple-beam interferometer suggest themselves for these purposes. Saunders [8] has reported observations on minute irregularities in optical surfaces by means of multiple-beam interferometry. Because of the great magnification of minute detail and the relatively large surface areas that can be examined simultaneously, multiple-beam interferometry lends itself readily to the precise study of the topography of plastic sheets. The multiple-beam or Fabry-Perot-type fringe is a classical interferometric technique. A number of applications and refinements of the method have appeared in recent years, many of which have been the work of Tolansky and his associates [9, 10]. These techniques yield magnification of detail in one direction only, the direction of height or depth. In the measurement of height this method equals or surpasses results obtained with the electron microscope, at the same time eliminating the elaborate specimen preparation required by the latter instrument. The electron microscope, however, yields other information that would be difficult or impossible to obtain with available interferometric techniques. Some indication of how these tools supplement one another is evident in the observations presented.

The acrylic and styrene plastics used in this study are amorphous high polymers. In these materials the total response to an applied stress contains three

[1] This investigation was conducted at the National Bureau of Standards under the sponsorship and with the financial assistance of the National Advisory Committee for Aeronautics; the help of this agency and members of its staff is gratefully acknowledged.

[2] Figures in brackets indicate the literature references at the end of this paper.

components. These are the instantaneous elasticity, retarded configurational elasticity, and flow. When the stress is removed there results an instantaneous recovery of the deformation due to the first component and a slower recovery from the second. Deformation due to flow is not recovered. These elements in the viscoelastic behavior of the polymer can be related to observed microstructural characteristics of crazed surfaces. It also aids in categorizing the mechanisms responsible for changes in the cracks and their associated deformations on exposure to elevated temperature or stress.

2. Materials

Specimens of cast commercial polymethyl methacrylate were the ones chiefly used in this investigation. Both the general-purpose and heat-resistant grades were studied. The sheets of cast polystyrene were also of commercial origin. The cast polymethyl alpha-chloroacrylate was experimental polymer.

Samples of acrylic laminate were also examined. The two outer layers of this laminate consisted of polymethyl methacrylate and the interlayer was plasticized polyvinyl butyral. The inner face of the acrylic outerlayer was examined.

3. Methods

3.1. Preparation of Crazed Specimens

The standard tensile specimens used were type I specimens described in Method 1011 of Federal Specification L–P–406b [11]. The specimens were stress-crazed by tensile loading in a hydraulic universal testing machine with the rate of head separation at 0.05 in./min. In some cases, the specimens were loaded until crazing occurred and then the load was released, whereas in other cases the load was applied until failure occurred.

This same type of specimen was also stress-solvent crazed. In this case, a sufficiently high load was applied and then the surface of the specimen was exposed to solvent either by holding a benzene-saturated blotter against one face for 10 sec or by stroking the surface with a small camel's hair brush saturated with solvent.

Whereas crazing in polymethyl methacrylate manifests itself primarily on the surface, in cast polystyrene and cast polymethyl alpha-chloroacrylate sheets it is also apparent throughout the matrix. In the two latter materials, the interior craze cracks appear to be associated with impurities. However, the surface craze cracks of these two materials were similar in shape and orientation to those observed in polymethyl methacrylate.

Flow lines were observed in some crazed specimens of polymethyl methacrylate, emanating from the ends of craze cracks. These flow lines were observed after the craze cracks appeared, and formed at angles of 35° to 45° to the cracks. The craze cracks did not appear to grow after the flow lines appeared.

Tapered tensile specimens which had been stress-solvent-crazed for use in another investigation were also examined. These specimens tapered in width from 0.500 to 0.333 in. over a 3-in. reduced section. The methods of crazing were the same as those described in the previous paragraph.

Solvent-crazed surfaces were also prepared by placing 2-in. squares cut from cast sheets of polymethyl methacrylate in boiling water for 2 or 3 min and then exposing them to monomeric methyl methacrylate until they were visibly crazed.

Flexural specimens were stressed statically as cantilevers to produce crazing.

3.2. Preparation of Surfaces for Interferometric Studies

Exposed surfaces of the plastic sheets quickly accumulated a film of dust particles from the surrounding air. These particles were thoroughly removed to facilitate the microscopic examination and permit the deposition of suitable metallic films on those specimens used for multiple-beam interferometry. Cleansing was carried on with extreme caution, as even gentle wiping with commercial cellulose tissues or with absorbent cotton was sufficient to produce surface marks that could be detected microscopically. Immersion in a stream of tap water followed by blotting with a good grade of lens tissue caused little apparent surface degradation. Such a procedure, however, is not adequate for removing all detritus, and foreign bodies were constantly encountered during the examinations.

The glass optical flats and other reference surfaces were handled by washing in soap and water and drying with lens tissue or boiled cotton or linen cloths. Old silver coatings were removed with a 30-percent solution of hydrogen peroxide.

The cleansed specimens and reference surfaces for multiple-beam interferometric studies were then placed in a metal evaporator. A film of silver was deposited on the crazed and uncrazed surfaces to be examined and on the optical or other glass surface to be used as the reference flat.

Plastic specimens on which the fringes were observed in transmission were coated with a layer of silver 400 to 500 A in thickness. Such films approach a reflectivity of 90 percent. Tolansky [9] presents considerable detail of the technique for evaporating a layer of the proper thickness and reflectivity. The films applied to these specimens were formed in a vacuum of 1×10^{-4} mm Hg or better. The heated tungsten filament was held at least 20 cm from the plastic to avoid overheating the specimen. A film of the desired thickness range was a deep blue color when viewed in transmission. With experience it was possible to make a visual estimate of the film thickness by its color and transmission. Observing the image of a small piece of white paper placed beneath the specimen also assisted in evaluating the layer of metal during its deposition. The extinction of the image can be used as the end point. Alternately, a measured amount of silver computed

to be sufficient to produce a film of the desired thickness at the distance of the specimen from the filament can be evaporated in its entirety.

Silver films of the same thickness were evaporated on all reference surfaces.

A layer of silver sufficiently thick to be totally reflecting (at least 1000 A) [12] was deposited on the plastic surfaces used for multiple-beam interferometric studies by reflection.

3.3. Preparation of Replicas for Electron Microscope Studies

Specimens were prepared by a slight modification of a replica technique described by Zworykin and Ramberg [13]. Crazed specimens of polymethyl methacrylate were placed in a vacuum unit which was pumped to 1×10^{-4} mm of Hg or less. Silver was evaporated perpendicularly on the specimens from a distance of 20 cm. A totally reflecting surface of silver was obtained (thickness of 1000 A or more). The specimens with their evaporated coatings were removed from the unit and melted paraffin was applied to the edges of the surface bearing the silver layer. The coated plastic was then placed in an electroplating solution and a layer of copper about 0.01 in. thick was deposited on the back of the silver film. The solution contained 4 g of copper sulfate and 0.6 mg of sulfuric acid per 20 ml of water. Deposition of the copper was accomplished with 0.1 to 0.2 amp/in.^{2}, but this value can be varied over wide limits. The metal layer was then cleanly stripped from the plastic specimen. The paraffin prevents the electroplating solution from attacking the evaporated film at the edges and eliminates the right-angle fins that tend to grow over the edge of the plastic during plating, thus complicating removal of the metal. The metal replica was washed in distilled water and dried.

The replicas were shadowed with chromium while displaced 4 cm vertically and 16 cm horizontally from the heated filament containing the metal. A thin layer of collodion in amyl acetate (about a 1% solution) was flowed over the replica, the excess allowed to drain, and the metal replica permitted to dry in a dust-free location. Then a 25-percent (by volume) solution of nitric acid was used to dissolve away the copper and silver, leaving a positive shadowed replica of collodion. The replica was washed in several changes of distilled water and mounted on wire grids. Steps involved in replication are shown schematically in figure 1.

3.4. Microscopic Techniques

For bright-field observations, the crazed specimens were examined with a compound microscope equipped with 16-mm or 4-mm objectives and a 10× ocular. Some tensile specimens were also studied with a dark-contrast 4-mm phase contrast objective. However, it was found that the methods of multiple-beam interference were most valuable for determining structures present in the plastic surfaces.

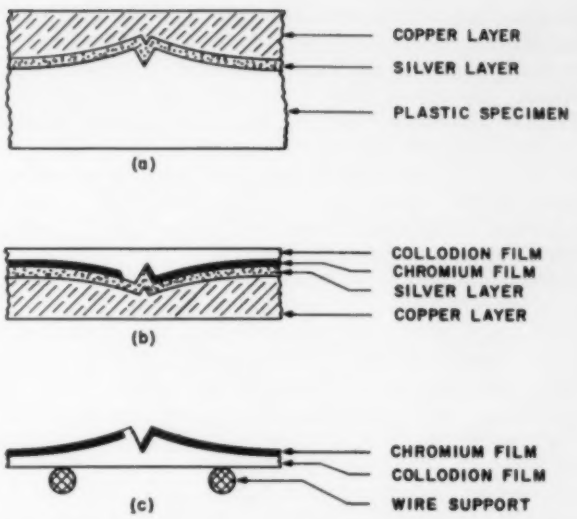

FIGURE 1. *Preparation of electron microscope specimens.*

(a) Silver is vacuum-deposited on the plastic sheet. A thicker layer of copper is electrodeposited on the silver. (b) The silver and copper layer is stripped from the plastic and shadowed with chromium. Collodion is then flowed over the chromium, forming a film replica. (c) Silver and copper films are removed with acid and the chromium shadow is mounted on a supporting grid.

a. Multiple-Beam Interferometry

(1) *Theory.* Observations with multiple-beam interferometry augmented the details revealed by transmission microscopy. The interference fringes formed in the thin film of air between a reference surface (optical flat) and the surface of a plastic sheet are governed by the well-known expression $n\lambda=2t\cos\theta\mu$, where n is the order of interference with a film of thickness t, λ the wave length of the light used, μ the refractive index of the air layer, and θ the angle of light incidence. When fringes are formed between unsilvered surfaces, only two light beams interfere. The lines of maximum intensity in such fringes are often difficult to determine and precise topographical detail cannot be measured. Multiple beams are produced by coating the surfaces producing interference with a highly reflecting, thin film of silver. The absorption of the film is held to the minimum possible at reflecting coefficients of 0.7 to 0.9. The successive reflecting of the beams between the silvered surfaces is sufficient to influence the resulting interference. This leads to a great increase in precision through sharpening of the fringes when all the beams are collected at the focus of a lens. The theory of interference by multiple beams is discussed in detail by Ditchburn [14] and Tolansky [9].

The equivalent positions of the fringes in the interferograms mark the loci of points separated by changes in the thickness of the interferometer air wedge equal to $\lambda/2$. Throughout this investigation $\lambda=546$ mμ. The interferogram, then, is a series of lines or fringes that reflect the surface contours of the specimen surface. When the fringes are straight parallel lines, the specimen surface approximates the flatness of the reference surface with which it is compared. Changes in the distance

between these lines are due not only to changes in microscopic magnification but are also dependent on the wedge angle between specimen and reference surface. Because the reference surface may be considered perfectly plane over the limited areas in a single field, all deviations in parallelism or direction of the fringes are a measure of the change in height of the specimen surface along the length of the fringe. Because of the fringe sharpness and the known geometric relations between fringe and surface contour, the specimen surface contour can often be determined with a high degree of accuracy.

For example, if we consider the interferogram in figure 7 and indicate the significant features by letters, the method of analysis will be obvious. The craze crack, which in this case is not a straight line, is indicated by XY. Because the linear distance from fringe I to fringe II also represents a change in the air wedge height of $\lambda/2$ or 273 mμ, then the surface containing point B has risen, or fallen, approximately this amount in the distance AB. Similarly, the surface containing D has risen (or fallen) approximately four-fifths of 273 mμ in the distance CD, and point F about one-third of 273 mμ in the distance EF. The fringes, then, yield a contour map of the surface topography wherever the fringes are propagated. In figure 7 it is obvious that the changes in surface height occur close to the craze crack itself and appear to decrease at the end of the crack length. Readjustment of the reference surface and the wedge angle will displace or change the fringe pattern, permitting the acquisition of more detailed information or of measurements at other points on the surface. The fringe separation will affect both sensitivity and precision of the measurements.

From the interferogram alone it is impossible to determine whether a discontinuity in the surface is a height or a depth. This can be ascertained, however, by pressing lightly against the plates of the interferometer. The fringes in this interferometer move in the direction of the thicker part of the air wedge. The considerations involved are shown schematically in figure 2. Other methods are available and were used for checking the direction of surface discontinuities. For example, a step wedge consisting of a thin layer of plastic is applied to part of the surface. Where the fringes reach the edge of the film they are deflected in direction by the thickness of the plastic film, thus indicating the direction for a height. Brossel [15] has described an extended source method of determining fringe direction which is easily applied to the specimens.

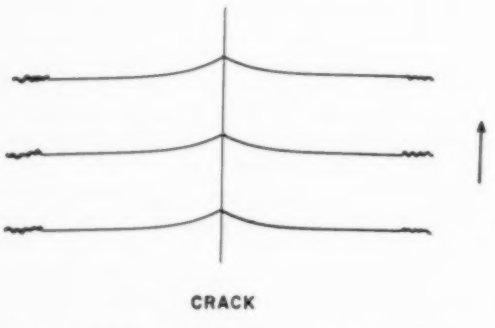

FIGURE 2. *Height or depth indication in interferograms when wedge angle is changed.*

If the wedge angle is decreased, the fringes move toward the wedge opening, indicating direction of decreasing distance between surfaces. This is the direction of the arrow. Thus the humps in the fringes are heights.

(2) *Transmission.* Specimens with semireflecting films of silver were used. An inverted universal microscope was modified to accept an AH–4 high-pressure mercury arc lamp in the transmission-source housing. The specimen was mounted in the microscope as shown in figure 3b. The parallel beam from the mercury lamp passes through a filter combination (Wratten 55 and Corning didymium) and enters the interference system, consisting of a semireflecting specimen and a semireflecting reference surface. The metal films were face to face. The microscope was focused on the fringes formed between the silvered surfaces of the specimen and the reference plate.

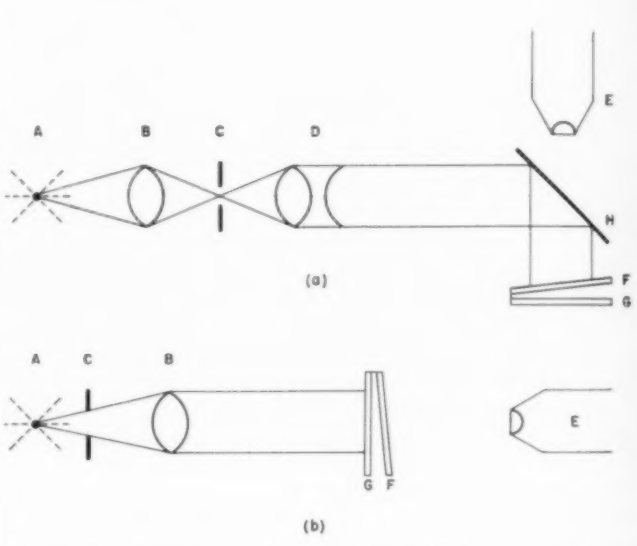

FIGURE 3. *Optical arrangement for multiple-beam interference.*

(a), Reflection; (b), transmission. A, Light source; B, condenser; C, slit; D, collimator; E, objective; F, specimen; G, reference surface; H, beam splitter.

(3) *Reflection.* Specimens with totally reflecting silver films were used. The same universal microscope was used as with the transmission method described above. However, in this case the high-pressure mercury lamp was inserted in the reflection-source housing and the specimen viewed as shown in figure 3a. The parallel beam of the lamp was filtered, and fell on the interference system of the totally reflecting specimen and the partially reflecting reference plate from the semireflector. The microscope was focused on the fringe system between the specimen and the reference surface.

b. Electron Microscopy

The electron microscope used was a 50-kv, permanent-magnet table model.

4. Observations and Discussion

4.1 Dimensions of Craze Cracks

Many of the individual cracks in the crazed specimens were easily distinguished by bright-field microscopy. Cracks observed by this technique are shown in the work reported by Russell [5] and others [2,3,4]. This does not mean that all cracks, particularly those in "blushed" or finely crazed areas, can be well resolved by this method. Chromium-shadowed collodion replicas were prepared from the surfaces of specimens of cast polymethyl methacrylate that had been crazed in short-time tensile tests. Specimens were chosen that had exceptionally fine cracks in the crazed areas. Figure 4 is an electron micrograph of one of these replicas. Despite the number of steps involved in its production, these replicas provide good resolution, and the craze crack appears as a height with the evaporated metal piled up on the side nearest the filament (black line) and

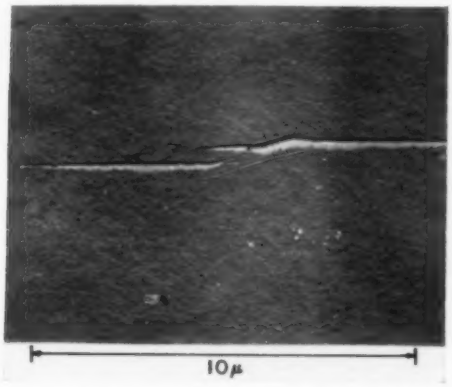

FIGURE 4. *Electron micrograph of a crack in a stress-crazed surface of polymethyl methacrylate.*

Collodion replica, chromium shadowed 4:1.

the light shadow appearing as a white or gray line. It is possible to make some accurate determinations of the dimensions from these replicas since the depth of the crack is given by the shadow, the maximum half-width by the black line of piled-up chromium, and the length directly from the impression. The craze cracks examined in the electron microscope varied in length from 2 to 10 μ.

Their widths ranged from 0.10 to 0.25 μ and their depths from 0.05 to 0.15 μ. In no case did the cracks appear to approach dimensions unresolvable by the electron microscope. The smallest cracks were also much larger than the structure observed in the replica substrate. This implies a minimum craze-crack length. One possible interpretation is that a certain minimum amount of energy is required to cause separation of the chain segments leading to crazing, and this energy threshold results in a minimum crack size. Alternately, there could exist a grain structure analogous to that of metals, which determines the threshold crack size. Further studies will be made to determine exactly the minimum crack size under various conditions.

4.2. Surface Dislocations Associated With Cracks

Uncrazed plastic surfaces yielded interferograms of the type shown in figure 5. Commercial samples of polymethyl methacrylate showed some fine detail along the fringes but no gross details other than those attributable to contamination or body deformation.

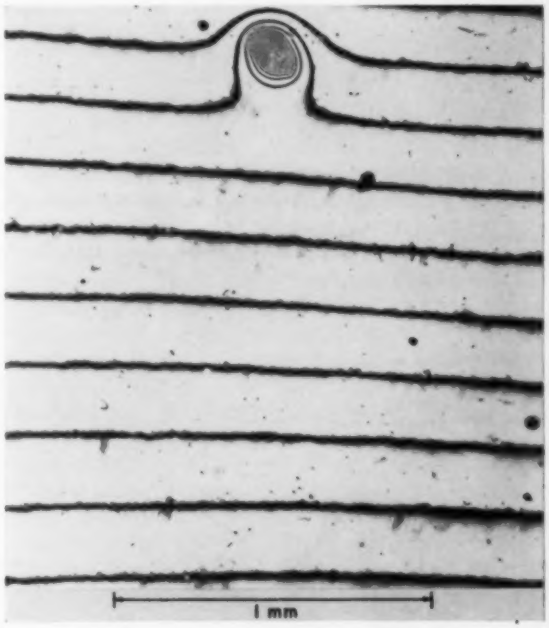

FIGURE 5. *Multiple-beam interferogram of an uncrazed surface of commercial cast polymethyl methacrylate.*

Some fine detail is observable along the fringes, and body deformations also exert a measurable effect on the over-all fringe pattern. The rounded detail is typical and apparently due to a mount of adhesive from the masking paper. Source is the 546-mμ line of a mercury lamp.

Interferograms of crazed surfaces, whether stress-crazed, solvent-crazed, or stress-solvent-crazed, exhibited fundamentally the same surface topography in the region of the craze cracks (figs. 6, 7, 8). The individual cracks could be seen to occupy an area that is displaced from the rest of the surface. This displacement appeared to increase with the size of the crack. It followed the crack very closely, as can be seen in the interferogram of the unoriented solvent-produced cracks (fig. 7).

The surface dislocations caused by the craze cracks varied considerably in magnitude, not only from crack to crack but along the length of the crack as well. Because the fringes can be best resolved by very

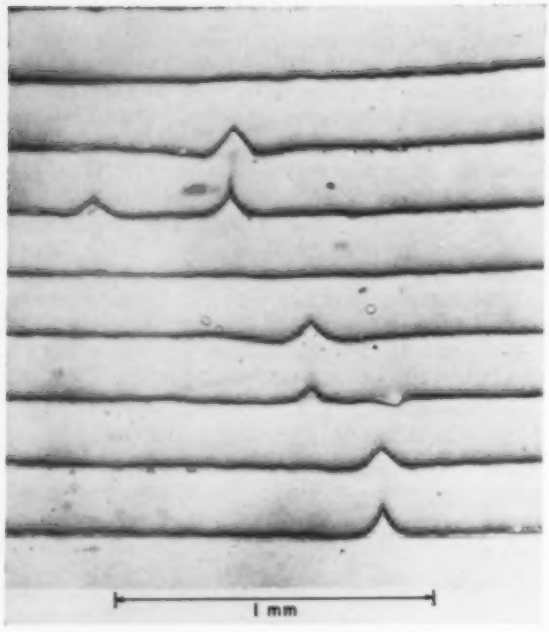

FIGURE 6. *Multiple-beam interferogram of the surface of a sheet of polymethyl methacrylate crazed in flexure.*

The discontinuities in the parellel fringes show the loci of the cracks which themselves are practically invisible. Source is the 546-mμ line of a mercury lamp.

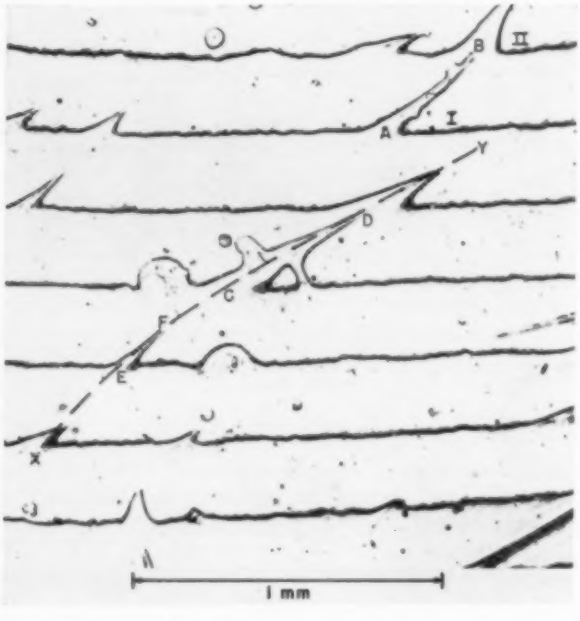

FIGURE 7. *Multiple-beam interferogram of the surface of a sheet of polymethyl methacrylate crazed by exposure to solvent.*

The numerous sharp discontinuities in the fringes mark the loci of the craze cracks which themselves are practically invisible. Source is the 546-mμ line of a mercury lamp.

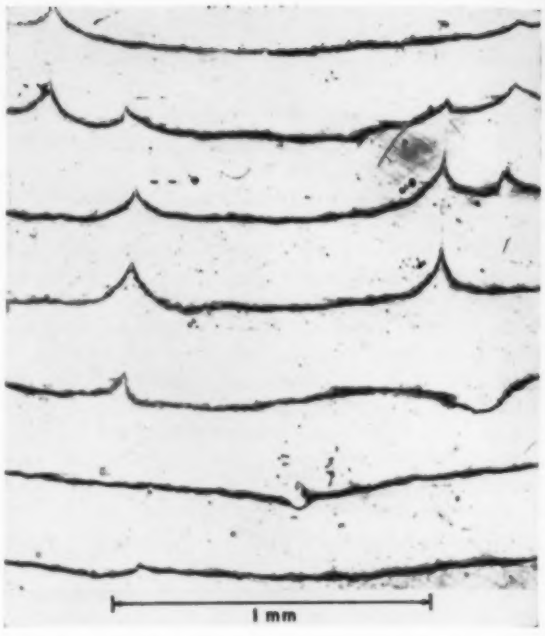

FIGURE 8. *Multiple-beam interferogram of the surface of a sheet of polymethyl methacrylate crazed by application of stress and solvent.*

The sharp discontinuities in the fringes mark the loci of the craze cracks. Because the specimen was stressed to failure, the long period fringe contours are the result of body deformation. Source is the 546-mμ line of a mercury lamp.

low-powered objectives in the simple technique previously described, the very fine cracks are somewhat difficult to study quantitatively, but the longer, coarser cracks are easily measured. For this reason, the stress-solvent-crazed material provides better demonstrations of the observations than the stress-crazed specimens.

Dimensions of the details of one of the cracks shown in the interferogram in figure 8 are shown schematically in figure 9. Although, as indicated previously, there is considerable variation, the maximum change in height for areas around stress-solvent-produced cracks was found to be about ½ λ or approximately 270 mμ. For stress-produced craze cracks the elevation is much less, apparently only a few hundred angstroms.

By using the techniques previously described, it was shown that the area around each crack was elevated and not depressed. The phase-contrast microscope was also used for this purpose. With a dark-contrast diffraction plate in the objective, the part of the specimen having the greater optical path will be darker than the surrounding parts having shorter paths. Thus, the crack itself appears bright, and the thickening adjacent to it is darker than the surround.

The behavior of the plastic sheet in forming these surface discontinuities around each crack can be simulated in the following experiment with a sheet

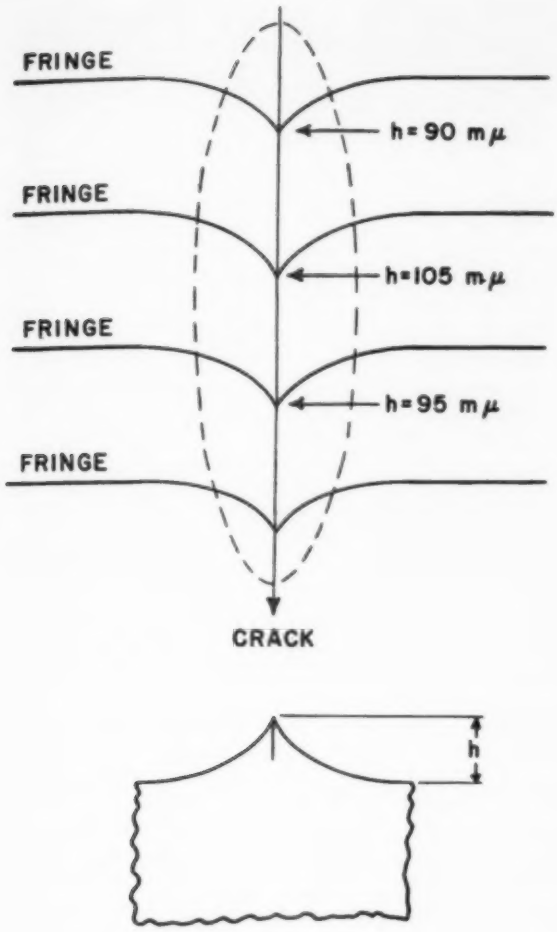

FIGURE 9. *Schematic representation of a craze crack from figure 8 (slightly idealized).*

The encircled portion shows the surface area affected ×100.

of rubber. A 1/16-in.-thick strip of rubber was superficially notched on one face with a sharp razor blade, the notch not extending to the edges, and with its long axis normal to the major axis of the specimen strip. When a tensile load, sufficient to cause considerable elongation, was applied parallel to the specimen's major axis, a raised area appeared around the notch. On releasing the tension the raised area subsided. When the specimen was observed on the unnotched side just opposite the notch while the tension was applied, it could be seen that a concavity formed at this point. The material of the rubber strip was apparently pulled up around the lips of the cracks at the expense of material from the opposite side. The rubber, being above the glass transition at room temperature, recovered on removal of the load, there being no delayed elasticity or flow. Recovery in the plastic sheets, which were below the glass transition, was much slower and incomplete because of these viscoelastic properties.

A complete explanation of this phenomenon of surface dislocation would require a lengthy and highly detailed stress analysis. Qualitatively, it can be said that the center axis through the cross section of the specimen is displaced locally by the formation of a craze crack due to the decrease in thickness at the point of the crack. The center axis moves to realine with the load line, and material on either side of the crack is displaced away from the center axis. In the case of the rubber sheet, this realinement also produces a concavity in the surface opposite the notch. However, the concavity observed on the reverse side of the rubber specimen could not be detected in the crazed plastic. Crazing is a phenomenon that for practical considerations is restricted to a thin surface membrane. Both the high modulus of elasticity and the thickness of the plastic specimen hinder the formation of the concavity observed in the rubber strip.

4.3. Surface Dislocations Under Load

The typical fringe contour showing a rise in the surface in the vicinity of craze cracks can be shown to be present while the crazed specimen is still under load. A series of observations was made on one stress-crazed and one stress-solvent-crazed specimen while still under load. Each specimen was clamped in a specially designed jig, which could be placed on the microscope stage and which would permit the application of a load to the specimen by means of a bolt at one end. An unmeasured load was applied for several months to the stress-crazed specimen. The stress-solvent-crazed specimen was under load for several weeks prior to the application of solvent to the surface. With the specimen still under load, the silver film was applied in vacuum and the specimen examined in the interferometer. Under load, the contour fringes indicated much the same type of displacement as in the other crazed specimens. For the stress-solvent-crazed specimen (fig. 10), the fringes were somewhat exaggerated when compared to specimens solvent-crazed in short-time loading. It is doubtful that the increased deformation was due to the fact that the specimen was still under stress, because on the removal of the load there was little, if any, recovery. Increasing the duration of the loading increased the size of the surface discontinuities. It can be seen from figure 10 that there are portions of the craze cracks that rise more steeply than the remainder, as if the lips of the cracks had yielded locally.

4.4. Recovery in Crazed Surfaces

Some recovery of crazing undoubtedly does occur in crazed specimens over long periods of time after the stress is removed. Crazed specimens of polymethyl methacrylate that were stored at room temperature for several months were found to have lost all or much of the visual evidence of crazing. On microscopic examination some residual evidence of

FIGURE 10. *Multiple-beam interferogram of the surface of a sheet of polymethyl methacrylate crazed by application of stress and solvent.*

The stress has not been removed. Horizontal lines intersecting the fringes were caused by abrasion resulting from wiping the surface with lens tissue. Source is the 546-mμ line of a mercury lamp.

crazing could be detected. A number of tensile specimens that had been stress-crazed some months earlier were silvered and examined in the multiple-beam interferometer. Although these specimens appeared uncrazed to the unaided eye and even in the bright-field microscope, the sites of the craze cracks were easily distinguished by multiple-beam interferometry. This residual crazing was evidently too slight to affect the optical properties of the sheet sufficiently to reveal the crazed condition without the aid of optical tools.

Some further observations on a number of crazed plastic specimens that had been heated, indicated the general aspects of this optical recovery. Tensile specimens of various types of commercial polymethyl methacrylate sheet were stress-crazed in short-time tensile tests. One of the halves of each specimen was heated for various periods of time up to 15 hours at 150° C in an air-circulating oven. When examined with the bright-field microscope, the half of the specimen that was not heated showed the typical cracks oriented with their long axis, normal to the principal stress (fig. 11). However, the half that had been heated appeared clear and uncrazed. Multiple-beam interferometry of the heated portion also revealed no indication of the surface dislocations associated with crazing.

Somewhat different results were obtained with specimens that were crazed by exposure to solvent while under stress. After crazing, loading was continued until failure occurred. Half of each broken specimen was given the same heat treatment as described for the stress-crazed plastic. The heated

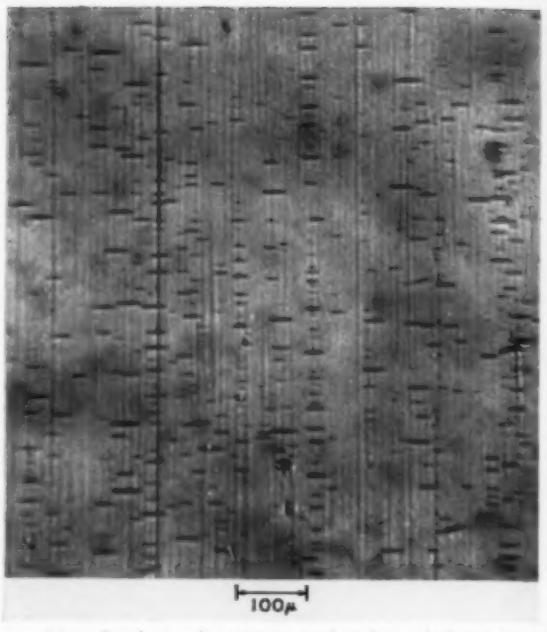

FIGURE 11. *Surface of stress-crazed polymethyl methacrylate.*

The stress was applied normal to the long axis of the cracks. Vertical lines are the result of wiping the surface with lens tissues.

specimens again showed no evidence of crazing when viewed with the bright-field microscope. Multiple-beam interferometry of the heated portion, however, revealed surface dislocations similar to those observed on unheated stress-solvent-crazed specimens. These dislocations were more rounded and gradual in contour and lacked, for the most part, the abrupt discontinuity at the crack (fig. 12). In addition, there

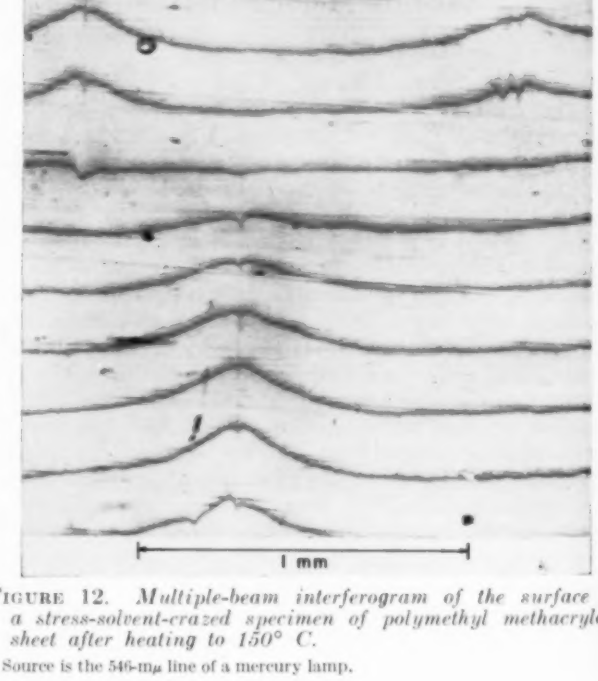

FIGURE 12. *Multiple-beam interferogram of the surface of a stress-solvent-crazed specimen of polymethyl methacrylate sheet after heating to 150° C.*

Source is the 546-mμ line of a mercury lamp.

appeared to be a widening of the crack itself, forming a trough along the crest of the dislocation (cf. fig. 8).

These experiments indicate that when the crazed surface is heated above the glass transition temperature, the surface tends to flow. Because the crack is largely responsible for the changes in optical path of the transmitted light, any change eliminating these physical discontinuities would improve the optical properties of the sheet. The slight and gradual thickenings of the sheet caused by the dislocations around the crack would be expected to impair the optical properties of the crack in less obvious fashion. In the stress-crazed surfaces the flow at 150° C is sufficient to erase all evidences of crazing in a relatively short period of time. At room temperature, the recovery is much slower. Stress-solvent craze cracks also tend to "recover", but the recovery is incomplete. The discontinuity of the crack is largely obliterated and the sharp edges are rounded. Some relaxation of the edges of the crack also occurs, forming the trough in the crest. Flow is less effective in eradicating the comparatively broad surface dislocations surrounding the crack.

The difference in behavior for the two types of crazing is probably due to the nature of the deformations associated with each type. In the case of stress-crazing in short-time tensile tests, a "frozen-in" elastic deformation is apparently involved, which would be completely recoverable. In stress-solvent crazing, however, considerable flow, at or near the surface, probably occurs, due to the plasticizing action of the solvent. This deformation is permanent and complete recovery is not observed as a result of heating.

In view of the great sensitivity of the multiple-beam technique in revealing evidence of crazing, experiments were conducted to determine if crazing could be detected by this method prior to its observation by the unaided eye. In the standard tensile tests described previously, specimens of cast polymethyl methacrylate crazed at strains of slightly more than 3 percent. Tensile specimens were strained, therefore, to only 1, 2, and 3 percent, and the load removed. These specimens, which appeared uncrazed to the eye, exhibited no craze cracks when observed by multiple-beam interferometry and phase or bright-field microscopy. Similarly, unstressed polymethyl methacrylate sheet showed no crazing when examined by these sensitive techniques. These results indicate that the observation of the onset of crazing by the eye is an adequately sensitive technique.

4.5. Loci of Craze Cracks

Distribution of the cracks across the section of the specimens differed with the polymer involved. All of the craze cracks observed in polymethyl methacrylate involved the surface, that is, the surface plane intersected the cracks. While some surface crazing was observed in polystyrene and in polymethyl alpha-chloroacrylate, there was also considerable internal crazing, i. e., cracks that did not open on the surface. However, the surface craze cracks of the polystyrene and the polymethyl alpha-chloroacrylate were similar in shape to those of polymethyl methacrylate.

Internal cracks in the polystyrene specimens were distributed fairly homogeneously throughout the section. Cracks would occur in groups of two or more, and in most instances the group was associated with a visible particle of foreign matter (fig. 13). It

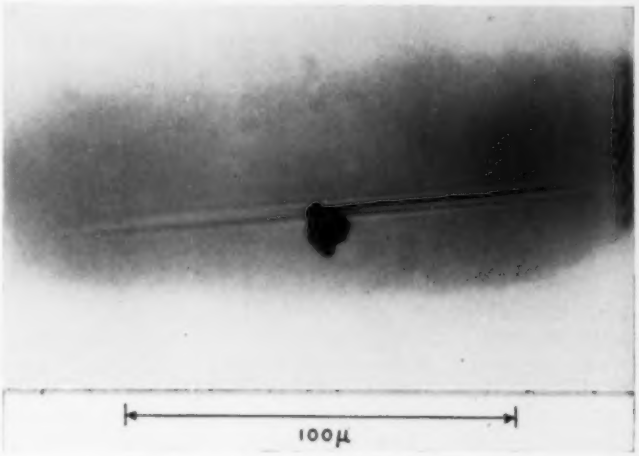

FIGURE 13. *Crazing in polystyrene.*
A single craze crack associated with a visible inhomogeneity.

would appear that internal crazing appeared in the polystyrene specimens at physical discontinuities, such as fragments of impurities, which were visible, or minute areas of inhomogeneities, which were not visible.

Crazing in the polymethyl alpha-chloroacrylate was mainly restricted to the center of the specimen section. Just under each cast surface was a clear section containing few, if any, cracks as shown in figure 14. When viewed with a microscope equipped with a double diaphragm [16], the cracks could be

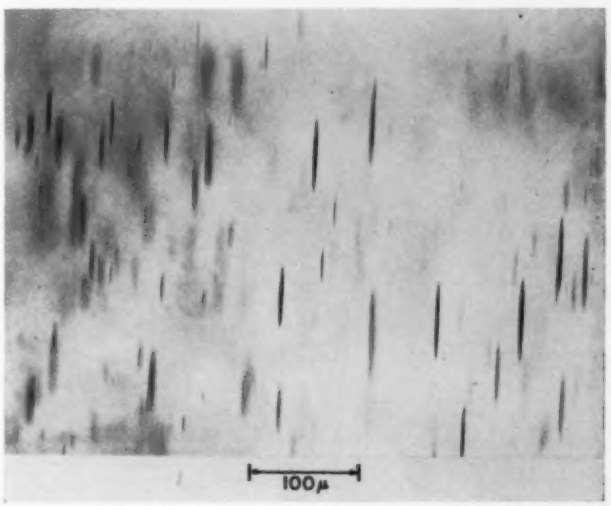

FIGURE 14. *Crazing in polymethyl alpha-chloroacrylate.*
The cast surface of the specimen is at the top of the photograph; the interior of the specimen is viewed through a machined and polished edge of the specimen. Note the clear area immediately adjacent to the edge.

seen to be areas of much lower index than the surrounding matrix. This would indicate that the cracks may be voids in the resin.

It is interesting to observe that the crazed specimens of polymethyl alpha-chloroacrylate, with a clear area near each surface, bear a striking resemblance to specimens of polymethyl methacrylate that had been subjected to atomic radiation in a pile and heated [17]. In the latter case, bubbles were formed in the interior of the specimens with a clear section extending inwards approximately 1 mm from all external surfaces. The authors explained that the bubbles in the interior of the material are due to gases that are evolved in the degradation of polymethyl methacrylate by irradiation. Bubbles do not occur near the surface because the gases produced there can escape.

4.6. Flow Associated With Cracks

During the studies of crazed surfaces with the optical microscope, a network of diagonal lines which appeared to emanate from the ends of craze cracks was observed in some stress-crazed tensile specimens of polymethyl methacrylate. The lines are more easily seen and photographed if the microscope is focused below the surface of the specimen (fig. 15). The lines were not observed on all crazed specimens of polymethyl methacrylate, even though the conditions of crazing were duplicated in replicate specimens. The angle between the trace of these flow lines on the surface and the craze cracks was somewhat variable. Values from about 35° to 45° were obtained on different specimens (fig. 15). Flow lines were also noted in one of the crazed specimens which had apparently "recovered" when examined without optical aids.

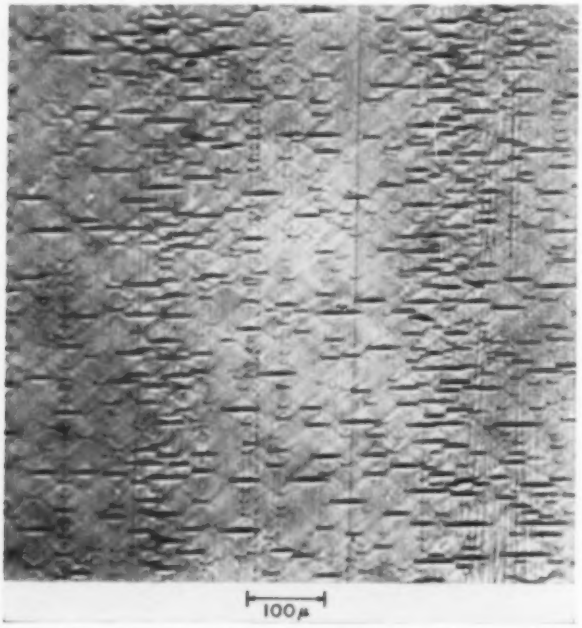

FIGURE 15. *Surface of a stress-crazed tensile specimen of polymethyl methacrylate.*

The image has been slightly defocused to emphasize the flow lines at the ends the cracks.

An optical microscope with approximately 100× magnification was set up in a horizontal position on a hydraulic testing machine to permit the observation of tensile specimens during the application of load. The relation between the appearance of craze cracks and flow lines could thus be observed. Of a number of specimens observed in this manner, only three exhibited flow lines. Two of these three specimens broke at strains of approximately 20 percent, which is higher than the usual average strain for this material. The other specimen broke at the usual average value, which is about 9 percent. The specimens crazed at strains of approximately 3 percent as observed in previous tests. The flow lines were first observed at strains of 8 to 10 percent. The lines clearly originated at the ends of craze cracks, forming an X-figure at each end. It was observed that many of the flow lines passed through the ends of several cracks. The growth of craze cracks was not observed after the appearance of the flow markings. This would seem to indicate that crazing may be the mechanism of stress relaxation in these particular cases up to a point, beyond which surface flow becomes the relaxation mechanism.

The network of flow lines noted in the bright-field microscope and shown in figure 15 can also be studied to advantage with multiple-beam interferometry. When the reference surface and the specimen surface are made as parallel as possible and the filters removed, high dispersion fringes result. For parallel plates, Fizeau fringes yield a uniform tint of given intensity. Local changes in plate separation produce changes in intensity. In the specimen in figure 16 there were residual angles due to surface

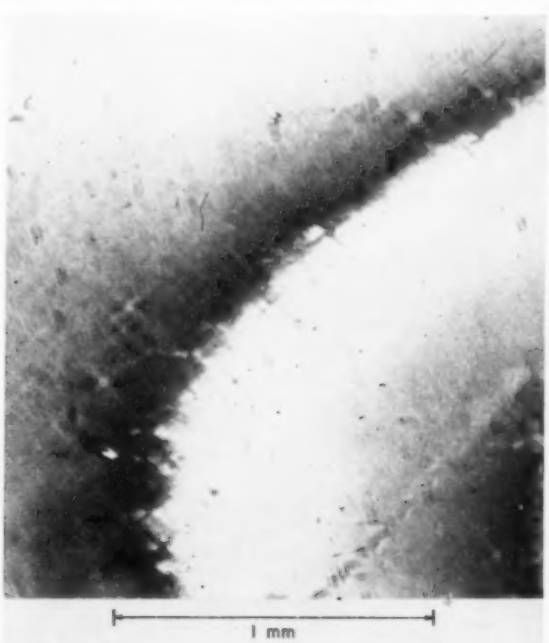

FIGURE 16. *Interferogram of a surface of polymethyl methacrylate showing flow at crack nuclei as indicated by changes in intensity.*

The reference plate and specimen are nearly parallel. The flow lines are visible as crosses. The broad fringe is a result of body deformation of the specimen. Source is the 546-mμ line of a mercury lamp.

features, but over much of the area shown in the photomicrograph, the flow lines are clearly visible as changes in intensity. Tolansky [9] has shown that for a given phase lag and reflectivity a 10-percent change in intensity is equal to 3 A. Although quantitative interpretation of this order would require precise densitometric determinations, which were not attempted in this study, it is obvious that this technique provides a powerful tool for the study of plastic surfaces and of surface structures. However, even a superficial examination revealed that these flow lines involved the surface and permitted a rough approximation of their height above the surface of the order of 25 to 50 mμ.

Similar flow lines were observed on the surfaces of biaxially stretched acrylic plastic sheet that had been stressed to failure without crazing. In this case, the nuclei consisted of bits of adhesive from the masking paper (fig. 17). Surfaces that craze are also sensitive to the presence of contaminants, such as adhesive, because the most severe crazing and opening up of the cracks is often associated with aggregations of adhesive (fig. 18).

Nadai [18] has shown that flow lines (Luder's lines) are produced by notches or holes. At a sharp reentrant edge the stresses are theoretically infinite, and local yielding in the neighborhood of such discontinuities may result. The resemblance of the flow lines in metal and paraffin specimens illustrated by Nadai bear a marked resemblance to the lines noted in the crazed polymethyl methacrylate tensile specimens. In the case of the uncrazed stretched material shown in figure 17, if the drop of adhesive on the surface is considered as forming a small round area

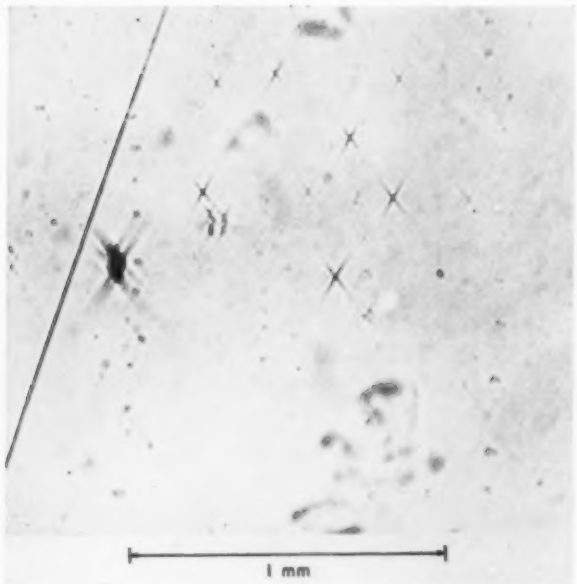

FIGURE 17. *Photomicrograph of the surface of a specimen of biaxially stretched polymethyl alpha-chloroacrylate that has been loaded to failure.*

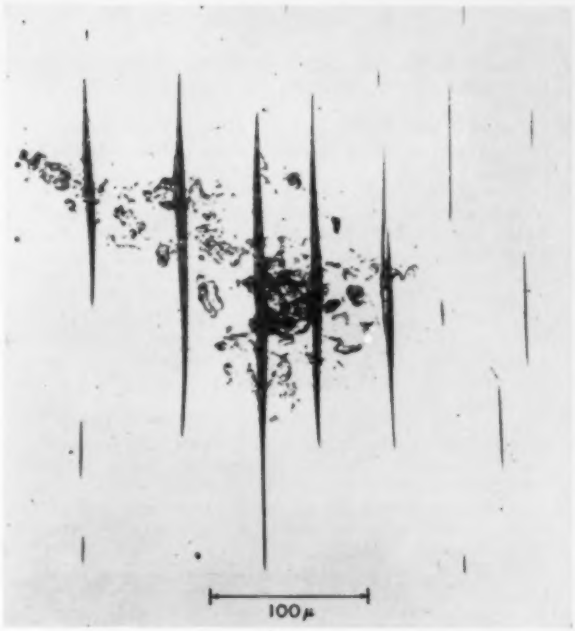

FIGURE 18. *Stress-crazed surface of a sheet of polymethyl methacrylate showing severity of crazing associated with surface contamination by adhesive.*

or a small circular hole in the surface film of the sheet, it is also possible to assume a mechanism for the development of the flow lines in these specimens.

For a small hole in a wide plate the tensile stress distribution is well known [19]. Further, the effect of stress concentration is not uniformly distributed around the hole but starts at two points on the boundary of the hole and progresses along a cross-shaped area. From Nadai's exposition it is shown that these two points are the location of peaks of the maximum shear stress on the hole boundary at $\theta=\pi/2$ and $3\pi/2$ and located in a plane perpendicular to the direction of the applied tension. Because this primary yielding is very much localized, it is rarely seen, but as the tensile stress is increased, yielding spreads and soon progresses along two lines symmetrically oriented to the direction of the tensile stress and at an angle of about 45° with it. The contour lines of the maximum shearing stresses can be checked by photoelastic techniques. Angles of lines observed in the crazed specimens are in fair agreement with those indicated.

In the case of a notch (such as the crazing crack in the surface plane) subjected to tension, much the same result is obtained [18]. F. van Iterson [20] has analyzed the stress situation in a hairline crack across a small part of the section by means of the plastic sector. The solution is also in agreement with the observed angles of the crazing cracks.

The authors acknowledge the assistance of Samuel Levy and Charles Proffer Saylor in the course of this work.

5. References

[1] J. A. Sauer, J. Marin, and C. C. Hsiao, Creep and damping properties of polystyrene, J. Appl. Phys. **20,** 507–517 (1949).

[2] B. Maxwell and L. F. Rahm, Rheological properties of polystyrene below 80 C, Ind. Eng. Chem. **41,** 1988–1993 (1949).

[3] B. Maxwell and L. F. Rahm, Factors affecting the crazing of polystyrene, J. Soc. Plastics Eng. **6,** 7–12 (1950); Tech. Rep. 14B (Plastics Laboratory, Princeton Univ., May 1949).

[4] C. C. Hsiao and J. A. Sauer, On crazing of linear high polymers, J. Appl. Phys. **21,** 1071–1083 (1950).

[5] E. W. Russell, Crazing of cast polymethyl methacrylate, Nature **165,** 91–96 (1950); Studies on polymethyl methacrylate, III: Crazing effects, Rep. Chem. 447 (Royal Aircraft Establishment, Farnborough Hants, England, 1948).

[6] B. M. Axilrod and M. A. Sherman, Effect of stress-solvent crazing on tensile strength of polymethyl methacrylate, Natl. Advisory Comm. Aeronaut., Tech. Note 2444 (1951); Modern Plastics **30,** 130–138 (June 1953).

[7] M. A. Sherman and B. M. Axilrod, Stress and strain at onset of crazing of polymethyl methacrylate at various temperatures, Natl. Advisory Comm. Aeronaut., Tech. Note 2778 (1952); Am. Soc. Testing Materials Bul. 191, 65–70 (1953).

[8] J. B. Saunders, Precise topography of optical surfaces, J. Research NBS **47,** 148–155 (1951) RP2239.

[9] S. Tolansky, Multiple beam interferometry of surfaces and films (Clarendon Press, Oxford, England, 1948).

[10] A. Verma, Crystal growth and dislocations (Academic Press, New York, N. Y., and Butterworth Press, London, 1953).

[11] Federal standard stock catalog IV (part 5), Federal specifications for plastics, organic: General specifications, test methods L–P–406b (1952).

[12] S. Dushman, Scientific foundations of vacuum technique (John Wiley & Sons, Inc., New York, N. Y., 1949).

[13] V. K. Zworykin and E. G. Ramberg, Surface studies with the electron microscope, J. Appl. Phys. **12,** 692–695 (1941).

[14] R. W. Ditchburn, Light (Blackie and Son, Ltd., London, 1952).

[15] J. Brossel, Asymmetrical broadening with multiple beam interference fringes, Nature **157,** 623 (1946).

[16] C. P. Saylor, Accuracy of microscopical methods for determining refractive index by immersion, J. Research NBS **15,** 277–294 (1935) RP829.

[17] M. Ross and A. Charlesby, The effect of pile radiation on polymethyl methacrylate (Perspex), I. Atomics **4,** 189–194 (1953).

[18] A. Nadai, Theory of flow and fracture of solids (McGraw-Hill Book Co., Inc., New York, N. Y., 1950).

[19] G. Kirsch, Die Theorie der Elastizität und die Bedürfnisse der Festigkeitslehre, Z. Vereines deut. Ingenieure **42,** 797 (1898).

[20] F. K. van Iterson, Plasticity in engineering (Hafner Publishing Co., New York, N. Y., 1947).

Washington, December 11, 1956.

INDEX TO VOLUME 58

January to June 1957—Research Papers 2727 to 2767

A

Page

ABO_3-type compounds, classification of, RP2736 ... 75
Accuracy of the Cutler-Hammer recording gas calorimeter when used with gases of high heating value, RP2754 ... 213
Actinium, emission spectra, RP2763 ... 297
Air, intermolecular forces in, RP2738 ... 93
Allen, H. C., Jr., E. K. Plyler, E. D. Tidwell, Infrared spectra of polychlorobenzenes, RP2758 ... 255
Alloys in the iron-chromium-molybdenum-nickel system, phase-diagram study, RP2728 ... 7
Alloys, nickel, thermal expansion, RP2737 ... 89
Aluminum, corrosion rate in acids and alkalies, influence of crystallographic orientation, RP2748 ... 157
Amplitude and phase of the low-frequency ground wave near a coastline, RP2756 ... 237
Antenna, slotted-cylinder, with a dielectric coating, RP2762 ... 287
Apatites deficient in divalent cations, RP2761 ... 279
Apatites, lead and calcium, RP2761 ... 279
Aqueous solutions, spectral absorbance of, in the range 10° to 40° C, RP2731 ... 33
Asphalts, chromatographically fractionated, infrared spectra, RP2759 ... 265
Azilrod, B. M., J. D. Hoffman, Theory of dielectric relaxation for the three-dimensional polar rotator: lattice models leading to bimodal loss curves RP2735 ... 61

B

Bechtoldt, C. J., H. C. Vacher, Phase-diagram study of alloys in the iron-chromium-molybdenum-nickel system, RP2728 ... 7
Bimodal dielectric loss curves, RP2735 ... 61
Birmingham, B. W., E. H. Brown, C. R. Class, A. F. Schmidt, Vessels for the storage and transport of liquid hydrogen, RP2757 ... 243
Blaine, L. R., E. K. Plyler, M. Nowak, Reference wavelengths for calibrating prism spectrometers, RP2752 ... 195
Boron-treated steels, temper brittleness of, RP2750 ... 175
Bozman, W. R., R. E. Trees, Matrices of spin-orbit interaction of the electron configuration $d^4 s$, RP2739 ... 95
Brass and Teflon tubes, resistance of flow in, RP2734 ... 51
Brockman, M. R., Resistance of flow in Teflon and brass tubes, RP2734 ... 51
Brown, E. H., B. W. Birmingham, C. R. Class, A. F. Schmidt, Vessels for the storage and transport of liquid hydrogen, RP2757 ... 243
Byers, F. C., E. E. Sager, Spectral absorbance of some aqueous solutions in the range 10° to 40° C, RP2731 ... 33

C

Calcified tissue, structure of, RP2761 ... 279
Calorimeter, gas, Cutler-Hammer, accuracy of, RP2754 ... 213
Class, C. R., B. W. Birmingham, E. H. Brown, A. F. Schmidt, Vessels for the storage and transport of liquid hydrogen, RP2757 ... 243
Classification of perovskite and other ABO_3-type compounds, RP2736 ... 75
Comparisons of national radium standards, RP2749 ... 169
Computer, high-speed, for predicting radioactive fallout, RP2740 ... 101
Conductivity, thermal of nitrogen, RP2760 ... 271
Copper, nickel, and copper-nickel alloys, tensile properties at high temperatures, RP2753 ... 201
Cordero, F., H. Matheson, D. P. Johnson, A nonlinear instrument diaphragm, RP2766 ... 333
Corrosion rate of aluminum in acids and alkalies, influence of crystallographic orientation, RP2748 ... 157
Corrosion rate of iron by polarization technique, measurement of, RP2746 ... 145
Crystallographic orientation, influence on corrosion rate of aluminum in acids and alkalies, RP2748 ... 157
Cutler-Hammer recording gas calorimeter, accuracy when used with gases of high heating value, RP2754 ... 213

D

Davis, P., Numerical computation of the transfinite diameter of two collinear line segments, RP2747 ... 155
Decimeter bars, stainless-steel, relative dimensional stabilities of, RP2742 ... 119
Defect structures, apatites, RP2761 ... 279
Dewar vessels for the storage and transport of liquid hydrogen and helium: RP2757 ... 243
RP2764 ... 317
Dielectric loss, theory of, RP2735 ... 61
Digges, T. G., W. D. Jenkins, C. R. Johnson, Tensile properties of copper, nickel, and 70-percent-copper-30-percent-nickel and 30-percent-copper-70-percent-nickel alloys at high temperatures, RP2753 ... 201
Dimensional stabilities of stainless steel length standards, RP2742 ... 119
Double-image prism, construction of, RP2729 ... 21
Double-image prism, Kösters, RP2730 ... 27

E

Eiseman, J. H., E. A. Potter, Accuracy of the Cutler-Hammer recording gas calorimeter when used with gases of high heating value, RP2754 ... 213
Electron configuration $d^4 s$, matrices of spin-orbit interaction of, RP2739 ... 95
Emission spectra of actinium, RP2763 ... 297

F

Page

Fallout, radioactive, high-speed computer for predicting, RP2740 ... 101
Fluorescent solutions, alpha- and gamma-excited, thermal quenching, RP2743 ... 125
Fred, M., W. F. Meggers, F. S. Tomkins, Emission spectra of actinium, RP2763 ... 297
Frequency conversion with nonlinear reactance, RP2755 ... 227
Friedman, A. S., Intermolecular forces in air, RP2738 ... 93
Further studies on the pyrolysis of polytetrafluoroethylene in the presence of various gases, RP2765 ... 327

G

Gas calorimeter, accuracy when used with gases of high heating value, RP2754 ... 213
Ginnings, D. C., R. L. Nuttall, Thermal conductivity of nitrogen from 50° to 500° C and 1 to 100 atmospheres, RP2760 ... 271
Glass, optical and volumetric relaxation effects in, following removal of high hydrostatic pressures, RP2751 ... 189
Glassy state transitions of poly-(chlorotrifluoroethylene), poly-(vinylidene fluoride and their copolymers, RP2745 ... 137
Gloss methods, two-parameter, RP2744 ... 127
Goodman, S., Radiant-heat transfer between nongray parallel plates, RP2732 ... 37
Ground wave, low-frequency, amplitude and phase of, RP2756 ... 237
Ground wave, low-frequency, influence of a ridge on, RP2727 ... 1

H

Heat transfer, radiant, between nongray parallel plates, RP2732 ... 37
Helium and liquid hydrogen, thermal design of large storage vessels:
RP2757 ... 243
RP2764 ... 317
Hidnert, P., Thermal expansion of some nickel alloys, RP2737 ... 89
Hoffman, J. D., B. M. Azilrod, Theory of dielectric relaxation for the three-dimensional polar rotator: lattice models leading to bimodal loss curves, RP2735 ... 61
Hydrogen, liquid, and helium vessels for the storage and transport of:
RP2757 ... 243
RP2764 ... 317
Hydrostatic pressure, high, effect on optical and volumetric relaxation in glass, RP2751 ... 189

I

Influence of a ridge on the low-frequency ground wave, RP2727 ... 1
Infrared spectra of chromatographically fractionated asphalts, RP2759 ... 265
Infrared spectra of polychlorobenzenes, RP2758 ... 255
Interferometer, double-image prism:
RP2729 ... 21
RP2730 ... 27
Interferometer, multiple-beam, plastics, RP2767 ... 339
Intermolecular forces in air, RP2738 ... 93
Ionization-chamber, standard, requirements for 250- to 500-kilovolt X-rays, RP2741 ... 111
Iron-chromium-molybdenum-nickel system, phase-diagram study of alloys in, RP2728 ... 7
Iron, corrosion rate, measurement by polarization techniques, RP2746 ... 145
Iron-halide lamps, wavelengths from, RP2733 ... 41

J

Jenkins, W. D., T. G. Digges, C. R. Johnson, Tensile properties of copper, nickel, and 70-percent-copper-30-percent-nickel and 30-percent-copper-70-percent-nickel alloys at high temperatures, RP2753 ... 201
Johnson, C. R., W. D. Jenkins, T. G. Digges, Tensile properties of copper, nickel, and 70-percent-copper-30-percent-nickel and 30-percent-copper-70-percent-nickel alloys at high temperatures, RP2753 ... 201
Johnson, D. P., F. Cordero, H. Matheson, A nonlinear instrument diaphragm, RP2766 ... 333

K

Kirn, F. S., H. O. Wyckoff, Standard ionization-chamber requirements for 250- to 500-kilovolt X-rays, RP2741 ... 111
Kösters double-image prism, RP2730 ... 27
Kösters double-image prism, construction of, RP2729 ... 21
Kösters interferometer, RP2730 ... 27

L

Lamps, iron-halide, wavelengths from, RP2733 ... 41
Lattice models leading to bimodal dielectric loss curves, theory of, RP2735 ... 61
Low-frequency wave near a coastline, amplitude and phase, RP2756 ... 237
Length standards, relative dimensional stabilities of, RP2742 ... 119
Loftus, T. P., W. B. Mann, L. F. Paolella, L. L. Stockmann, W. J. Youden, Comparisons of national radium standards, RP2749 ... 169
Low-frequency ground wave, influence of a ridge on, RP2727 ... 1

M

Page

Malitson, I., C. Weir, S. Spinner, W. Rodney, Optical and volumetric relaxation effects in glass following removal of high hydrostatic pressures, RP 2751 189
Mandelkern, L., G. M. Martin, F. A. Quinn, Jr., Glassy state transitions of poly-(chlorotrifluoroethylene), poly-(vinylidene fluoride), and their copolymers, RP2745 137
Mann, W. B., T. P. Loftus, L. F. Paolella, L. L. Stockmann, W. J. Youden, Comparisons of national radium standards, RP2749 169
Martin, G. M., F. A. Quinn, Jr., L. Mandelkern, Glassy state transitions of poly-(chlorotrifluoroethylene), poly-(vinylidene fluoride), and their copolymers, RP2745 137
Matheson, H., F. Cordero, D. P. Johnson, A nonlinear instrument diaphragm, RP2766 333
Matrices of spin-orbit interaction of the electron configuration d^4s, RP2739 95
Measurement of the corrosion rate of iron by polarization techniques, RP 2746 145
Meggers, W. F., M. Fred, F. S. Tomkins, Emission spectra of actinium, RP2763 297
—, *R. W. Stanley*, Wavelengths from iron-halide lamps, RP2733 41
Michaelsen, J. D., L. A. Wall, Further studies on the pyroplysis of polytetrafluoroethylene in the presence of various gases, RP2765 327
Mientka, W., J. R. Wait, Slotted-cylinder antenna with a dielectric coating, RP2762 287
Murphy, A., J. R. Wait, Influence of a ridge on the low-frequency ground wave, RP2727 1

N

National radium standards, comparisons of, RP2749 169
Newman, S. B., I. Wolock, Optical studies of crazed plastic surfaces, RP2767 339
Nickel alloys, thermal expansion of, RP2737 89
Nickel, copper, and copper-nickel alloys, tensile properties at high temperatures, RP2753 201
Nimeroff, I., Two-parameter gloss methods, RP2744 127
Nitrogen from 50° to 500° C and 1 to 100 atmospheres, thermal conductivity of, RP2760 271
Nonlinear instrument diaphragm, RP2766 333
Nowak, M., E. K. Plyer, L. R. Blaine, Reference wavelengths for calibrating prism spectrometers, RP2752 195
Numerical analysis, computation of the transfinite diameter of two collinear line segments, RP2747 155
Nuttall, R. L., D. C. Ginnings, Thermal conductivity of nitrogen from 50° to 500° C and 1 to 100 atmospheres, RP2760 271

O

Optical and volumetric relaxation effects in glass following removal of high hydrostatic pressures, RP2751 189
Optical studies of crazed plastic surfaces, RP2767 339
Orem, T. H., Influence of crystallographic orientation on the corrosion rate of aluminum in acids and alkalies, RP2748 157
Orthonormal polynomials, collinear line segments, computation of, RP2747 155
Oxygen, quenching by, in fluorescent solutions, RP2743 125

P

Page, B. L., Relative dimensional stabilities of a selected series of stainless-steel decimeter bars, RP2742 119
Page, C. H., Frequency conversion with nonlinear reactance, RP2755 227
Paolella, L. F., T. P. Loftus, W. B. Mann, L. L. Stockmann, W. J. Youden, Comparisons of national radium standards, RP2749 169
Perloff, A., A. S. Posner, Apatites deficient in divalent cations, RP2761 279
Perovskite and other ABO_3-type compounds, classification of, RP2736 75
Phase-diagram study of alloys in the iron-chromium-molybdenum-nickel system, RP2728 7
Plastic surfaces, microscopy of, RP2767 339
Plyler, E. K., H. C. Allen, Jr., E. D. Tidwell, Infrared spectra of polychlorobenzenes, RP2758 255
—, *L. R. Blaine, M. Nowak*, Reference wavelengths for calibrating prism spectrometers, RP2752 195
Polar rotator, three-dimensional, theory of dielectric relaxation for, RP2735 61
Polarization techniques, measurement of corrosion rate of iron by, RP2746 145
Polychlorobenzenes, infrared spectra, RP2758 255
Poly-(chlorotrifluoroethylene), glassy state transitions of, RP2745 137
Polytetrafluoroethylene, pyrolysis of, in the presence of various gases, RP2765 327
Poly-(vinylidene fluoride), glassy state transitions of, RP2745 137
Posner, A. S., A. Perloff, Apatites deficient in divalent cations, RP2761 279
Potter, E. A., J. H. Eiseman, Accuracy of the Cutler-Hammer recording gas calorimeter when used with gases of high heating value, RP2754 213
Prism, double-image, RP2730 27
Prism, double-image, construction of, RP2729 21
Prism spectrometers, reference wavelengths for calibrating, RP2752 195
Pyrolysis of polytetrafluoroethylene in the presence of various gases, RP2765 327

Q

Quenching, thermal, in alpha- and gamma-excited fluorescent solutions, RP2743 125
Quinn, F. A., Jr., L. Mandelkern, G. M. Martin, Glassy state transitions of poly-(chlorotrifluoroethylene), poly-(vinylidene fluoride), and their copolymers, RP2745 137

R

Page

Radiant-heat transfer between nongray parallel plates, RP2732 37
Radio propagation, amplitude and phase of the low-frequency ground wave near a coastline, RP2756 237
Radio propagation, influence of a ridge on the low-frequency ground wave, RP2727 1
Radio propagation, slotted-cylinder antenna with a dielectric coating, RP2762 287
Radioactive fallout, high-speed computer for predicting, RP2740 101
Radium standards, national, comparisons of, RP2749 169
Reference wavelengths for calibrating prism spectrometers, RP2752 195
Relative dimensional stabilities of a selected series of stainless-steel decimeter bars, RP2742 119
Resistance of flow in Teflon and brass tubes, RP2734 51
Rodney, W., C. Weir, S. Spinner, I. Malitson, Optical and volumetric relaxation effects in glass following removal of high hydrostatic pressures, RP2751 189
Rosenberg, S. J., Temper brittleness of boron-treated steels, RP2750 175
Roth, R. S., Classification of perovskite and other ABO_3-type compounds, RP2736 73

S

Sager, E. E., F. C. Byers, Spectral absorbance of some aqueous solutions in the range 10° to 40° C, RP2731 33
Saunders, J. B., Construction of a Kösters double-image prism, RP2729 21
—, The Kösters interferometer, RP2730 27
Schmidt, A. F., B. W. Birmingham, E. H. Brown, C. R. Class, Vessels for the storage and transport of liquid hydrogen, RP2757 243
Schwerdtfeger, W. J., Measurement of the corrosion rate of iron by polarization techniques, RP2746 145
Scott, R. B., Thermal design of large storage vessels for liquid hydrogen and helium, RP2764 317
Seliger, H. H., C. A. Ziegler, Thermal quenching in alpha- and gamma-excited fluorescent solutions, RP2743 125
Skramstad, H. K., J. H. Wright, L. Taback, A high-speed computer for predicting radioactive fallout, RP2740 101
Slotted-cylinder antenna with a dielectric coating, RP2762 287
Spectra, emission, of actinium, RP2763 297
Spectra, infrared, of chromatographically fractionated asphalts, RP2759 265
Spectra, infrared, of polychlorobenzene, RP2758 255
Spectral absorbance of some aqueous solutions in the range 10° to 40° C, RP2731 33
Spectrometers, prism, reference wavelengths for calibrating, RP2752 195
Spinner, S., C. Weir, I. Malitson, W. Rodney, Optical and volumetric relaxation effects in glass following removal of high hydrostatic pressures, RP2751 189
Spin-orbit interaction of the electron configuration d^4s, matrices of, RP2739 95
Stainless steel, phase-diagram study of alloys in the iron-chromium-molybdenum-nickel system, RP2728 7
Standard ionization-chamber requirements for 250- to 500-kilovolt X-rays, RP2741 111
Standards, national radium, comparisons of, RP2749 169
Standards, wavelengths from iron-halide lamps, RP2733 41
Stanley, R. W., W. F. Meggers, Wavelengths from iron-halide lamps, RP2733 41
Steels, boron-treated, temper brittleness of, RP2750 175
Stewart, J. E., Infrared spectra of chromatographically fractionated asphalts, RP2759 265
Stockmann, L. L., T. P. Loftus, W. B. Mann, L. F. Paolella, W. J. Youden, Comparisons of national radium standards, RP2749 169
Storage and transport of liquid hydrogen and helium, vessels for:
RP2757 243
RP2764 317

T

Taback, L., J. H. Wright, H. K. Skramstad, A high-speed computer for predicting radioactive fallout, RP2740 101
Teflon and brass tubes, resistance of flow in, RP2734 51
Temper brittleness of boron-treated steels, RP2750 175
Tensile properties of copper, nickel, and 70-percent-copper–30-percent-nickel and 30-percent-copper–70-percent-nickel alloys at high temperatures, RP2753 201
Theory of dielectric relaxation for the three-dimensional polar rotator: lattice models leading to bimodal loss curves, RP2735 61
Thermal conductivity of nitrogen from 50° to 500° C and 1 to 100 atmospheres, RP2760 271
Thermal design of large storage vessels for liquid hydrogen and helium:
RP2757 243
RP2764 317
Thermal expansion of some nickel alloys, RP2737 89
Thermal quenching in alpha- and gamma-excited fluorescent solutions, RP2743 125
Tidwell, E. D., E. K. Plyler, H. C. Allen, Jr., Infrared spectra of polychlorobenzenes, RP2758 255
Tomkins, F. S., W. F. Meggers, M. Fred, Emission spectra of actinium, RP2763 297
Transfinite diameter of two collinear line segments, numerical computation, RP2747 155
Trees, R. E., W. R. Bozman, Matrices of spin-orbit interaction of the electron configuration d^4s, RP2739 95
Two-parameter gloss methods, RP2744 127

V

Vacher, H. C., C. J. Rechtoldt, Phase-diagram study of alloys in the iron-chromium-molybdenum-nickel system, RP2728 7
Vessels for the storage and transport of liquid hydrogen and helium:
RP2757 243
RP2764 317

W

Page

Wait, J. R., Amplitude and phase of the low-frequency ground wave near a coastline, RP2756 237

—, *A. Murphy*, Influence of a ridge on the low-frequency ground wave, RP2727 1

—, *W. Mientka*, Slotted-cylinder antenna with a dielectric coating, RP2762 1

Wall, L. A., J. D. Michaelsen, Further studies on the pyrolysis of polytetrafluoroethylene in the presence of various gases, RP2765 327

Water-flow, resistance of, in Teflon and brass tubes, RP2734 51

Wavelengths from iron-halide lamps, RP2733 41

Wavelengths, reference, for calibrating prism spectrometers, RP2752 195

Weir, C., S. Spinner, I. Malitson, W. Rodney, Optical and volumetric relaxation effects in glass following removal of high hydrostatic pressures, RP2751 189

Wolock, I., S. B. Newman, Optical studies of crazed plastic surfaces, RP2767 339

Wright, J. H., L. Taback, H. K. Skramstad, A high-speed computer for predicting radioactive fallout, RP2740 101

Wyckoff, H. O., F. S. Kirn, Standard ionization-chamber requirements for 250- to 500-kilovolt X-rays, RP2741 111

X

Page

X-rays, 250- to 500-kilovolt, standard ionization-chamber requirements for, RP2741 111

Y

Youden, W. J., T. P. Loftus, W. B. Mann, L. F. Paolella, L. L. Stockmann, Comparisons of national radium standards, RP2749 169

Z

Ziegler, C. A., H. H. Seliger, Thermal quenching in alpha- and gamma-excited fluorescent solutions, RP2743 125

U. S. GOVERNMENT PRINTING OFFICE: 1957

THE NATIONAL BUREAU OF STANDARDS

The scope of activities of the National Bureau of Standards at its headquarters in Washington, D. C., and its major field laboratories in Boulder, Colorado, is suggested in the following listing of the divisions and sections engaged in technical work. In general, each section carries out specialized research, development, and engineering in the field indicated by its title. A brief description of the activities, and of the resultant publications, appears on the inside of the front cover.

WASHINGTON, D. C.

Electricity and Electronics. Resistance and Reactance. Electron Devices. Electrical Instruments. Magnetic Measurements. Dielectrics. Engineering Electronics. Electronic Instrumentation. Electrochemistry.

Optics and Metrology. Photometry and Colorimetry. Optical Instruments. Photographic Technology. Length. Engineering Metrology.

Heat and Power. Temperature Physics. Thermodynamics. Cryogenic Physics. Rheology. Engine Fuels. Free Radicals Research.

Atomic and Radiation Physics. Spectroscopy. Radiometry. Mass Spectrometry. Solid State Physics. Electron Physics. Atomic Physics. Neutron Physics Nuclear Physics. Radioactivity. X-rays. Betatron. Nucleonic Instrumentation. Radiological Equipment. AEC Radiation Instruments.

Chemistry. Organic Coatings. Surface Chemistry. Organic Chemistry. Analytical Chemistry. Inorganic Chemistry. Electrodeposition. Gas Chemistry. Physical Chemistry. Thermochemistry. Spectrochemistry. Pure Substances.

Mechanics. Sound. Mechanical Instruments. Fluid Mechanics. Engineering Mechanics. Mass and Scale. Capacity, Density, and Fluid Meters. Combustion Controls.

Organic and Fibrous Materials. Rubber. Textiles. Paper. Leather. Testing and Specifications. Polymer Structure. Plastics. Dental Research.

Metallurgy. Thermal Metallurgy. Chemical Metallurgy. Mechanical Metallurgy. Corrosion. Metal Physics.

Mineral Products. Engineering Ceramics. Glass. Refractories. Enameled Metals. Concreting Materials. Constitution and Microstructure.

Building Technology. Structural Engineering. Fire Protection. Air Conditioning, Heating, and Refrigeration. Floor, Roof, and Wall Coverings. Codes and Specifications. Heat Transfer.

Applied Mathematics. Numerical Analysis. Computation. Statistical Engineering. Mathematical Physics.

Data Processing Systems. SEAC Engineering Group. Components and Techniques. Digital Circuitry. Digital Systems. Analog Systems. Application Engineering.

Office of Basic Instrumentation.

• Office of Weights and Measures.

BOULDER, COLORADO

Cryogenic Engineering. Cryogenic Equipment. Cryogenic Processes. Properties of Materials. Gas Liquefaction.

Radio Propagation Physics. Upper Atmosphere Research. Ionospheric Research. Regular Propagation Services. Sun-Earth Relationships.

Radio Propagation Engineering. Data Reduction Instrumentation. Modulation Systems. Navigation Systems. Radio Noise. Tropospheric Measurements. Tropospheric Analysis. Radio Systems Application Engineering.

Radio Standards. High Frequency Electrical Standards. Radio Broadcast Service. High Frequency Impedance Standards. Calibration Center. Microwave Physics. Microwave Circuit Standards.

Recent Publications of the National Bureau of Standards

Journal of Research of the National Bureau of Standards, Volume 58, No. 4, April 1957 (RP2749 to RP2754, incl.), 60 cents. Annual subscription, $4.00.

Technical News Bulletin, Volume 41, No. 4, April 1957. 10 cents. Annual subscription $1.00.

Basic Radio Propagation Predictions for July 1957. Three months in advance. CRPL–D 152. Issued April 1957. 10 cents. Annual subscription $1.00.

Miscellaneous Publications

M220. Annual Report 1956, National Bureau of Standards. 60 cents.

UNITED STATES
GOVERNMENT PRIN
DIVISION OF PUBLIC
WASHINGTON :

OFFICIAL BU

PENALTY FOR PRIVATE USE TO AVOID
PAYMENT OF POSTAGE, $300
(GPO)

UNIVERSITY OF MICHIGAN
GENERAL LIBRARY
DOCUMENTS DIVISION
1276 ANN ARBOR MICH

Contents

		Page
Slotted-cylinder antenna with a dielectric coating. James R. Wait and Walter Mientka.	RP2762	287
Emission spectra of actinium. William F. Meggers, Mark Fred, and Frank S. Tomkins.	RP2763	297
Thermal design of large storage vessels for liquid hydrogen and helium. Russell B. Scott.	RP2764	317
Further studies on the pyrolysis of polytetrafluoroethylene in the presence of various gases. J. D. Michaelsen and L. A. Wall.	RP2765	327
A nonlinear instrument diaphragm. Fidel Cordero, Harry Matheson, and Daniel P. Johnson.	RP2766	333
Optical studies of crazed plastic surfaces. Sanford B. Newman and Irvin Wolock.	RP2767	339
Index to volume 58 (January to June 1957, Research Papers RP2727 to RP2767).		351

[A list of recent NBS publications is given on page 3 of the cover.]

For sale by the Superintendent of Documents, U. S. Government Printing Office, Washington 25, D. C. Price 60 cents (single copy). Subscription price: $4.00 a year; $1.25 additional for foreign mailing.

UNITED STATES GOVERNMENT PRINTING OFFICE, WASHINGTON : 1957